Characterization of Nanoparticle Based Exogenous Soft Tissue Contrast and Prospectively Gated Image Analysis for Live In Vivo Micro-Computed Tomography Imaging of Avian Morphogenesis

A Dissertation

Presented to the Faculty of the Graduate School

Of Cornell University

In Partial Fulfillment of the Requirements for the Degree of

Doctor of Philosophy

by

Chelsea Lynn Gregg

August 2016

©2016 Chelsea Lynn Gregg

Characterization of Nanoparticle Based Exogenous Soft Tissue Contrast and Prospectively Gated Image Analysis for Live In Vivo Micro-Computed Tomography Imaging of Avian Morphogenesis

Chelsea Lynn Gregg

Cornell University 2016

Congenital defects account for 3% of all live births with 1% of those having a congenital heart defect. Currently, visualization of live embryonic development is largely limited to the earliest stages of development where traditional optical imaging techniques are widely used. Nearly any malformation arising during the early stages of development would be embryo lethal but clinically relevant malformations manifest during the mid-late stages of development where live embryonic imaging analysis has rarely been accomplished. The prevalence and variety of congenital malformations suggest that single genetic origins are not the culprit but instead defects arise from the large, genome wide mis-expression due to mechanical and/or chemical perturbations. Quantitative longitudinal analysis of live embryonic morphogenesis during the mid-late stages is critical for revealing normal and abnormal tissue assembly, enabling the identification of key contributing factors and parsing out mechanistic underpinnings of these processes.

The focus of this dissertation was to develop new and adaptation of current three dimensional imaging technologies for the long term visualization and characterization of live embryonic morphogenesis during the mid-late stages of development. Toxicity,

biodistribution, and persistence of metallic nanoparticles were quantified in avian embryos for use as a live contrast media (Chapter 2). We also identified that the particles can be used to calculate transport phenomena within the tissue through the deduction of relative perfusion rates into the dorsal mesenchyme from the aorta (Chapter 2). Extension of this technology into longitudinal analysis revealed that the biodistribution and persistence of the same 110nm alkaline earth metal particle was both spatially and temporally heterogeneous and unique at each embryonic age invested between days 4-11 of development (Chapter 3). Anatomy and identification of tissue boundaries comparable to that of standard histological sections and in some instances outperformed the information from thin sections, particularly in non tissue boundary regions of the embryos. Through the modeling of perfusion rates into the tissue we found that perfusion was spatially specific into the left and right myocardium even with homogenous distribution of particles in the ventricular lumens immediately post injection; elucidating the side specific differences in the myocardium, particularly the myocardial compaction and orientation differences which may contribute to disparities in the perfusion (Chapter 3). Furthermore, dynamic analysis of the embryonic heart reveals landmark metrics of cardiac function imperative to understanding the functional consequences of normal and abnormal cardiogenesis. This was accomplished through building and validating a prospective image gating system that used direct visualization of the heart rate for tracking and triggering the image acquisition. Specifically, images were taken at peak systole and peak diastole to reveal the extremes of the heart conformation, revealing the extent of tissue dynamics that are occurring during the cardiac cycle (Chapter 4).

Overall this body of work contributes significantly the understanding live embryonic development through the ability to visualize mid-late stage morphogenetic processes in vivo though high resolution microCT imaging. The imaging platform not only enables three dimensional visualization of morphogenesis but reveals relative material changes through bulk particle transport that is both spatially and temporally heterogeneous with unique components at each embryonic age. The studies presented here allow for direct live quantification of embryogenesis in real time and provide a means for parsing out gross morphological changes involved in normal tissue assembly and has the ability to be extended to diseased embryonic models for elucidating the phenotypical changes and suggesting the mechanistic underpinnings that may be responsible for diseased patterning and mitigation.

BIOGRAPHICAL SKETCH

Chelsea graduated summa cum laude in May 2010 from Arizona State University (ASU) with a Bachelors of Science degree in bioengineering and dual emphasis in molecular/cellular engineering and medical imaging. While at ASU, she was accepted into a joint BS/MS program in biomedical engineering and completed her first MS degree in December 2010 just one semester after her BS degree. During her time at ASU, Chelsea was a member of Tau Beta Pi Engineering Honor Society and Alpha Eta Mu Beta Biomedical Engineering Honor Society based on academic achievement. Additionally, Chelsea was a member of Engineers Without Borders (EWB) where she was the project manager for the Tsuraku, Ecuador Water Project. Chelsea traveled to Ecuador in the summers of 2008 and 2009 to build a new water system for a rural village in Ecuador implementing the engineering designs, serving as the leading member during the school year. Furthermore, Chelsea was selected for an undergraduate research fellowship that funded her honors thesis project where she graduated from Barrett the Honors College in 2010 concurrently with her BS. For her undergraduate thesis, Chelsea produced and purified the bone sialoprotein in a bacterial model for incorporation into polymer based scaffolds with the end goal of localized bone regeneration. In parallel with her involvement in EWB and scientific research, she has held an industrial internship at Capstone Therapeutics, served as an undergraduate teaching assistant for the computer science and engineering department, and volunteered her time as a private student tutor. For her MS thesis, Chelsea diversified her research portfolio transferring from molecular engineering to

anatomical modeling based of medical image datasets. For her MS thesis, Chelsea generated anatomically accurate flow phantom model of cerebral aneurysms based on patient data for experimental flow analysis.

Chelsea chose to pursue a PhD from Cornell University beginning in Fall 2011. She became a PhD candidate in August 2014 and was awarded her second MS degree in biomedical engineering. During her tenure at Cornell, Chelsea was awarded a Swanson fellowship through the biomedical engineering department, a National Science Foundation Diversity fellowship, National Science Foundation GK-12 fellowship, and a Cornell University Center for Vertebrae Genomics fellowship. Chelsea has mentored 12 different students both individually and in groups for a variety of research projects. She has published four first author peer reviewed journal articles, is currently writing an additional two manuscripts, and has eight conference publications. In parallel to her graduate research, Chelsea is a fellow in the Broadening Experiences in Scientific Training (BEST) program with specific involvement in science policy. She began a student led science policy organization called Advancing Science and Policy (ASAP) where she organizes annual trips to Washington DC and facilitates students in pursuing their own policy interests with a focus on science for policy and policy for science initiatives. This includes guiding op-ed writing, outreach efforts locally, DC lobbying efforts, and monthly roundtable discussions on current science policy topics. Chelsea's doctoral research focuses on the development of new and adaptation of current 3D live in vivo imaging technologies for use in embryonic imaging of mid-late stages of development for capturing morphogenetic tissue assembly.

For my parents, Michael Gregg and Janet Gregg

ACKNOWLEDGEMENTS

First and foremost I would like to thank my parents for their encouragement, unwavering support, and believing in me even when I struggled with believing in myself. They have supported and encouraged me to push to edge of my comfort zone because I will always regret what I do not try. Their love and devotion has certainly molded me into the person that I have become today and I hope that they know how much I love them. While she will never be able to read this, I want to thank and acknowledge my cat Annabel whose companionship has comforted me through the most difficult times during my graduate career.

I would like to thank my advisor Dr. Jonathan Butcher for his support and guidance during my tenure at Cornell. He has helped me find my own tenacity in the face of adversity during my graduate career. I would also like to express my gratitude to my committee members Dr. Natasza Kurpios and Dr. Warren Zipfel for their guidance and expertise. In particular, I would like to thank Dr. Julian Palacios Goerger from the Zipfel lab for all of his help and collaboration with the gating portion of my thesis; it would not have been possible without him. Furthermore, I would like to thank Dr. Chris Schaffer, the Director of Graduate Studies for biomedical engineering and my science policy mentor. Through Chris' mentorship in science policy, I have found a drive in policy and advocacy that I never knew I had. I cannot thank him enough for giving me the opportunities to learn about molding my career with science policy as a part of it. I would also like to thank my entire lab family both past and present. Specifically Jen Richards, Stephanie Lindsey, Emily Farrar, Leah Pagnozzi, Dan Cheung, David

Bassen, and Terence Gee. Their support and friendship has made coming into lab fun every day.

I would like to acknowledge the Broadening Experiences in Scientific Training program at Cornell for giving me a community of students and faculty who encourage and embrace many different career paths for a PhD educated scientist to engage in. The opportunities and support that they give students is irreplaceable and I am so grateful for how they have encouraged my professional development.

I would like to acknowledge the National Institutes of Health and the National Science Foundation for supporting all of my work throughout my 5 year tenure at Cornell. Their financial support in the pursuit of scientific knowledge is invaluable to the training of young scientists.

Lastly, I would like to thank my entire family for their love and support of me through this difficult but rewarding time during my career. They have always encouraged me to go after my dreams and to never put limitations on what I am capable of.

TABLE OF CONTENTS

BIOGRAPHICAL SKETCH iii
ACKNOWLEDGEMENTS vi
TABLE OF CONTENTS viii
LIST OF FIGURES xi
LIST OF ABBREVIATIONS xiii
CHAPTER 1 - INTRODUCTION 1
1.1 Fundamental Analysis of Vertebrate Embryonic Development 1
1.2 Cardiogenesis and Congenital Cardiac Pathology 2
1.3 Avian Animal Model 6
1.4 Embryonic Imaging Techniques 8
1.4.1 Optical Imaging 9
1.4.2 Ultrasound Imaging 11
1.4.3 Magnetic Resonance Imaging 12
1.4.4 Micro-Computed Tomography 13
1.5 Nanoparticle Exogenous Contrast Media 16
1.6 Image Processing: Acquisition, Restoration, and Analysis 18
1.7 Research Objectives 20
1.7.1 - Aim 1 (Chapter 2): Characterization of commercially available metallic nanoparticles for use as a non-toxic exogenous soft tissue contrast media for live in vivo microCT imaging of avian embryonic development 22
1.7.2 - Aim 2 (Chapter 3): Longitudinal Quantitative Three Dimensional Assessment of Live Embryonic Morphogenesis during Mid-Late Stages of Development via In Vivo MicroCT Imaging 23
1.7.3 - Aim 3 (Chapter 4): Prospective gated image analysis of functional, dynamic heart changes during mid-late stage cardiogenesis 24
1.7.4 Summary 25
References 27
CHAPTER 2 – COMPARATIVE ANALYSIS OF METALLIC NANOPARTICLES AS EXOGENOUS SOFT TISSUE CONTRAST FOR LIVE IN VIVO MICRO-COMPUTED TOMOGRAPHY IMAGING OF AVIAN EMBRYONIC MORPHOGENESIS 32
2.1 Abstract 32
2.2 Introduction 33
2.3 Materials and Methods 37

2.4 Results 41
References 59
CHAPTER 3 - LONGITUDINAL, QUANTITATIVE IN VIVO THREE DIMENSIONAL ANALYSIS OF LIVE AVIAN MORPHOGENESIS WITH HIGH RESOLUTION MICRO-COMPUTED TOMOGRAPHY IMAGING DURING MID-LATE STAGES OF DEVELOPMENT 67
3.1 Abstract 67
3.2 Introduction 68
3.3 Experimental Procedures 72
3.4 Results 75
3.5 Discussion 92
References 100
CHAPTER 4 - THREE DIMENSIONAL, LIVE IN VIVO DYNAMIC MICRO-COMPUTED TOMOGRAPHY IMAGING OF AVIAN CARDIOGENESIS THROUGH PROSPECTIVE GATING ACQUISITION 106
4.1 Abstract 106
4.2 Introduction 107
4.3Experimental Procedures 110
4.4 Results 115
References 132
CHAPTER 5 144
CONCLUSIONS AND FUTURE DIRECTIONS 144
5.1 Conclusions 144
5.2 Future Directions 152
References 164
CHAPTER 6 - EFFECTIVE ENGAGEMENT OF INQUIRY BASED LEARNING IN THE K-12 SCIENCE CLASSROOM: AN EX OVO CHICK CULTURE FOR THE STUDY OF ETHANOL ON EMBRYONIC DEVELOPMENT 168
6.1 Abstract 168
6.2 Introduction 169
6.3 Experimental and Pedagogical Methods 169
6.4 Results 172
6.5 Discussion 174
APPENDIX A – GK-12 PRE AND POST TEST FOR EVALUATING STUDENT LEARNING 175
APPENDIX B – RELEVANT PROTOCOLS 176

APPENDIX C – MATLAB SCRIPTS.....194

LIST OF FIGURES

Chapter 1

Figure 1.1 - Embryonic Heart Development Schematic..... 3
Figure 1.2 - CHDs result in severe and often times multiple defects. 5
Figure 1.3 - Comparison of common imaging modalities 9
Figure 1.4 - Flow diagram of mechanical, chemical, and genetic inputs for morphogenesis..... 20
Figure 1.5 - Illustration of dissertation specific aims with corresponding hypotheses.... 26

Chapter 2

Figure 2.1 - Microinjection set up and identification of select organ analysis for nanoparticle contrast enhancement 41
Figure 2.2 - Metallic nanoparticle comparison with varying scan voltages. 42
Figure 2.3 - Nanoparticle Toxicity Analysis and Contrast Enhancement Calibration. (A) Acute heart rate analysis of day 3 chicks following treatment with metallic nanoparticle contrast media injected at 10% blood volume with EBSS serving as a negative control. (B) Body anatomical measurements of nanoparticle treated chicks as compared to controls. (C) Contrast enhancement vs. amount of metal dilution curve 44
Figure 2.4 - Immediately post injection peak contrast 46
Figure 2.5 - 3D Comparison of Metallic Nanoparticles 48
Figure 2.6 - Temporal contrast enhancement comparison 49
Figure 2.7 - Direct metallic nanoparticle comparison as compared to Visipaque 51
Figure 2.8 - Perfusion analysis of particles from the dorsal aorta into the flank mesenchyme. 53

Chapter 3

Figure 3.1 - Tb skeletal muscle paralysis efficacy and toxicity 76
Figure 3.2 - Virtual histological sections of live embryos compared to standard histology 79
Figure 3.3 - Tissue boundary identification via grayscale mapping of line scans 81
Figure 3.4 - Longitudinal biodistribution of nanoparticle contrast over multiple organ systems 82
Figure 3.5 - Long term live in vivo modeled growth metrics 86
Figure 3.6 - Longitudinal myocardial analysis of spatial and temporal contrast dynamics 90
Figure 3.7 - Longitudinal transport analysis into the left and right myocardium 94

Chapter 4

Figure 4.1 - Functional flow diagram of surface and contour plots 114
Figure 4.2 - Functional flow diagram of prospectively gated image acquisition 116
Figure 4.3 - Gating hardware schematic and imagesl 117
Figure 4.4 - Visualization of embryo heart beat tracking 118
Figure 4.5 – Tracking algorithm for identification of the maximum or minimum 119
Figure 4.6 - Dynamic volumetric analysis of day 9 and day 11 embryonic chick hearts. Systolic, diastolic, and control 3D volumetric reconstructions for day 9 (top) and day 11 (bottom) embryos with corresponding measured lumen volume changes in the right and left ventricles. 120
Figure 4.7 - Day 9 contour and surface mapping of the right and left ventricles 124
Figure 4.8 - Day 11 contour and surface mapping of the right and left ventricles 125
Figure 4.9 - Realtive bulk trabecular density based on volumetric blood changes 126

Chapter 5

Figure 5.1 - Pictorial representation of key future directions. 153
Figure 5.2 – Diagram of 1D and 2D perfusion finite element modeling of spatial and temporal nanoparticle movements 159
Figure 5.3 – NanoCT images of left atrial ligations and rescues 159
Figure 5.4 - Immunohistochemistry stains of Quek 1 antibody 159
Figure 5.5 - Liposome nanoparticles containing FITC 160

Chapter 6

Figure 6.1 - Ex ovo culturing method 171
Figure 6.2 - Heart rate and anatomical analysis of long term ethanol exposure to developing chick embryos 173

LIST OF ABBREVIATIONS

2D	Two dimensional
3D	Three dimensional
microCT	Micro-computed tomography
nanoCT	Nano-computed tomography
RVC	Right ventricular chamber
LVC	Left ventricular chamber
VS	Ventricular septum
RVM	Right ventricular myocardium
LVM	Left ventricular myocardium
CRL	Crown-rump length
DVL	Dorso-ventral length
ED	Eye diameter
FL	Foot length
WL	Wing length
Quek1	Quail endothelial kinase one
MIP	Maximum intensity projection
Vol. Rend.	Volumetric rendering
EXTN	Exitron nano 12000
VP	Visipaque
AuNP	Gold nanoparticles
H	Heart

He	Head
DA	Dorsal aorta
A	Allantois
OP	Omnipaque
miRNA	MicroRNA

CHAPTER 1

INTRODUCTION

1.1 Fundamental Analysis of Vertebrate Embryonic Development

Proper embryogenesis requires the successful completion of three fundamental processes: growth, differentiation, and organization(Dehaan and Ebert 1964). These three elements occur across multiple length and time scales involving numerous cell types and secreted factors. Dissecting the functional contributions of each component and their molecular mechanisms is critical for understanding the genetic and environmental cues that influence tissue behavior. Understanding has progressed slowly but deliberately over the last century through the use of vertebrate animal models, aided through complex surgical manipulations and/or well controlled genetic perturbations. Imaging technology has been essential to identify morphological changes in embryos over time and as a result of these perturbations. Early research studied large-scale changes in organ shape and/or growth that ultimately cause gross malformations that in many cases are not survivable. From this foundation, more focused and localized changes in tissue morphogenesis have been pursued, including conditional (time and space) genetic mutations, localized microsurgical ablation, and environmental changes. Discoveries that many organs and tissues are organized and matured through heterogeneous patterning by several different cell lineages, each with the potential of multiple fate decisions has unveiled the complexity and intricacy of

morphogenesis. The dysregulation of these processes can result in a congenital malformation with the most common being congenital heart defects (CHD).

1.2 Cardiogenesis and Congenital Cardiac Pathology

Extra-embryonic vasculature begins with the appearance of blood islands quickly becoming patent blood vessels forming the vitelline vascular network. In the embryo proper, the most apparent beginnings of the vasculature (dorsal aorta and posterior cardinal veins) arise out of the mesenchyme *in situ* (Coffin & Poole, 1988). The early stages of embryonic development (i.e. neuralation and the onset of organogenesis) result in rapid vascular and blood formation. Many minor vessels are formed through sprouting (Coffin & Poole, 1988). The degree of vessel remodeling and angiogenesis occurs in conjunction with organ development with no surprise that the dorsal aorta and heart tube are concomitants (Coffin & Poole, 1988).

Heart formation begins first with chamber development and is followed by septation (Lamers, 2002). The onset of cardiogenesis begins with the formation of the heart tube from splanchnic mesoderm brought to the midline due to body folding at Hamburger-Hamilton stages 8-9 (Manner, 2000). The heart tube elongates along the cranio-caudal axis (Manner, 2000). After elongation of the heart tube, it bends towards the right side of the body going through the first phase of looping, c looping (Manner, 2000). The developing heart goes from the c looping to the s looping phase. By the end of the s looping, the heart has positioned itself with spatial specificity of the definitive heart anatomy with primitive atria, ventricular bend, and primitive OFT (Manner, 2000). Post

s looping of the heart results in morphological changes of the truncus arteriosus and shifting of the future OFT ventral with respect to the right atrium (Manner, 2000).

Septation is the process by which the heart is separated into a dual channel pump containing one way valves with pulmonary and systemic halves (Lamers, 2002). Endocardial cushions are responsible for the separation of the common AV canal into right and left AV canals (Lamers, 2002). OFT septation begins with two pairs of endocardial cushions oriented at 90˚ angles to each other. The cushions first fuse with their counterpart and proximo-distally with each other. The right angle difference between the two sets of cushions causes a clockwise rotation generating a spiral septum, separating the OFTs into pulmonary and systemic trunks. Additionally, intra-atrial and intra-ventricular septa form from tissue outgrowth within the heart. In the

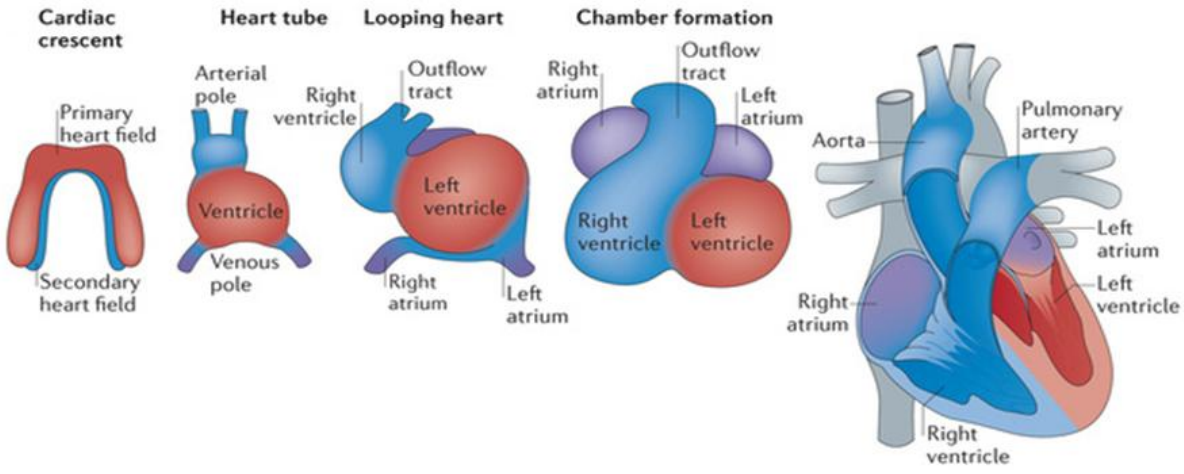

Figure 1.1 - Embryonic Heart Development Schematic. Diagram representing the entirety of cardiogenesis from progenitor heart field recruitment to a fully patterned heart (Xin et al., 2013)

avian embryo, heart looping and septation are complete by day 7 of development (Gregg & Butcher, 2013). Beginning at day 4 of avian development, septation becomes

apparent through the appearance of endocardial cushions and the intra-atrial septum prium (Gregg & Butcher, 2013). A graphical summary of heart development can be found in Figure 1.1 (Xin, Olson, & Bassel-duby, 2013). Congenital heart defects (CHD) are the most common congenital disease (Yang, Khoury et al. 1997) with estimated incidence rates as high as 10 in 1000 live births (Hoffman and Kaplan 2002). Furthermore, 45% of deaths resulting from a congenital defect are due to a cardiac malformation (Yang, Khoury et al. 1997). CHD comprise a highly variable group of malformations affecting the heart, great vessels, and outflow tract ranging in severity and often times altering the hemodynamics in the heart with two of many CHD examples given in Figure 1.2 (Lucille Packard Children's Hospital at Stanford; National Heart, Lung, and Blood Institute). The ability to treat CHD and the survivability is varied. In many instances, minor septal defects do not require surgery (Roest and de Roos 2012) but complex malformations such as hypoplastic left heart syndrome require immediate postnatal surgical intervention and the survival rate after the first week of life for these patients can be as low as 39% (Samanek 1992). Within the past three decades, improvements in fetal cardiovascular imaging has been instrumental in evaluating the heart and diagnosing CHD prenatally (Kleinman, Hobbins et al. 1980) contributing to the postnatal survival of patients born with complex CHD (Bonnet, Coltri et al. 1999; Tworetzky, McElhinney et al. 2001). Furthermore, when a CHD is present, evaluating the spatial progression of the defect over gestation allows for important developmental information to be learned (Hornberger, Sanders et al. 1995; Hornberger, Sanders et al. 1995). With the advancements in imaging technologies, surgical planning and intervention is improving but not all defects are detected prior to birth.

Beyond the heart, patients who suffer from a CHD have a higher susceptibility for further long term health concerns. Conditions such as hyponatremia, anemia, and renal dysfunction are frequently encountered along with a higher susceptibility for developing dementia in patients who have a CHD (Dimopoulos, Diller et al. 2008; Dimopoulos, Diller et al. 2009; Dimopoulos, Diller et al. 2010; Gorelick, Scuteri et al. 2011). Many of these long term complications are due to blood flow changes from the malformation, causing a cascade of events resulting in lifelong health problems. Prenatal assessment of CHD has the ability to improve perioperative management and surgical outcomes that can ideally return the hemodynamic environment of the heart close to its native state, reducing the downstream affects caused by systemic blood flow changes.

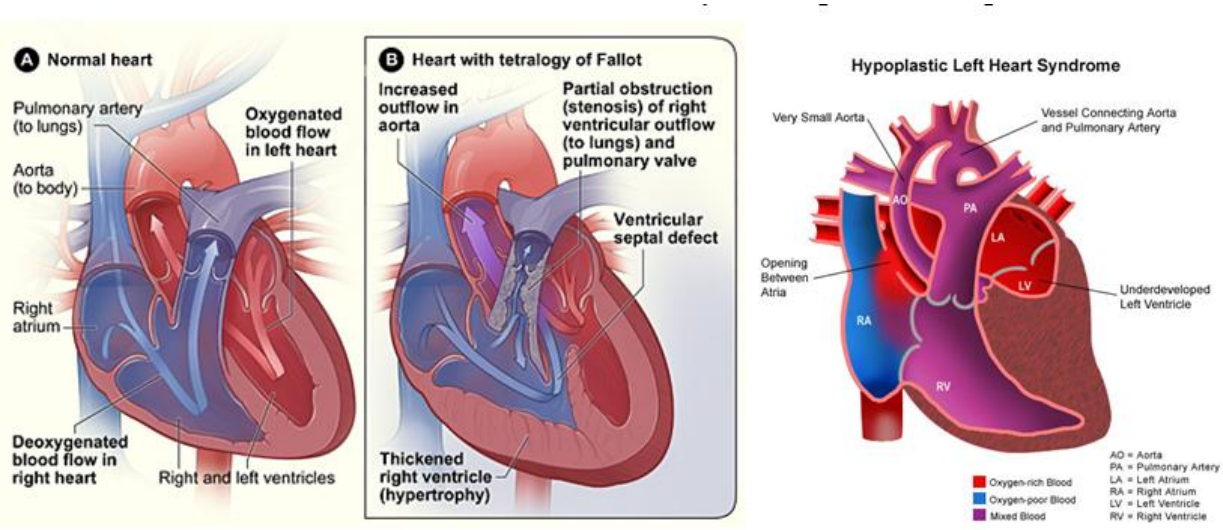

Figure 1.2 - CHDs result in severe and often times multiple defects. CHDs result in abnormal anatomy in the lumen, outflow track, and/or myocardium (Lucile Packard Children's Hospital at Stanford; National Heart, Lung, and Blood Institute)

The genetic contribution to the development of a CHD varies with the malformation but less than 10% of many common defects can be traced to a genetic origin (Pierpont, Basson et al. 2007), suggesting that there are several other mechanisms at the root of

CHD development paving the way for scientific research. This leaves a considerable amount of scientific real estate to be explored but the technology has to be available for the types of inquiries required for understanding defect mechanisms. A reliable animal model and high resolution deep tissue imaging are critical for breaching this knowledge gap.

1.3 Avian Animal Model

Chick and quail embryos have been a vital tool for the study of development for the past 100 years (Darnell & Schoenwolf, 2000; Le Douarin, 2008; Patten, Akd, & Barry, n.d.; Wilson, Roth, & Warkany, 1953). Avian models (chick and quail) are inexpensive and the embryo is easily accessed by either an ex ovo culture or through windowing the egg shell in an in ovo egg culture. Avian models have been particularly useful for establishing cell movements and tissue fates. Birds have a four chambered heart, developed in the same manner as the mammalian heart, capable of developing relevant CHDs through surgical manipulation or genetic perturbation (Hogers, DeRuiter, Gittenberger-de Groot, & Poelmann, 1999). Chick and quail embryos do not require maternal contributions for growth post oogenesis and the ease of use makes it an ideal candidate for studying morphodynamics.

Avian models however have limited molecular targets for tissue specific studies and have not been widely manipulated genetically (Chapman, Lawson et al. 2005; Bower, Sato et al. 2011; Seidl, Sanchez et al. 2013) with treatments required for every egg. Surgical perturbations of avian embryos, achieved via a metallic clip or ligation, enable

quantitative understanding of the role of hemodynamic forces on heart development (Broekhuizen, Hogers et al. 1999; Ursem, Struijk et al. 2001; Ursem, de Vos et al. 2002; Stekelenburg-de Vos, Ursem et al. 2003; Stekelenburg-De Vos, Steendijk et al. 2005; Stekelenburg-de Vos, Steendijk et al. 2007; Oosterbaan, Ursem et al. 2009). Coupling OCT imaging with computational analysis to examine the hemodyamic environments within the developing aortic arches of early stage chick embryos informs the affects of fluid-structure mechanics but is limited to the first few days of development (Kowalski, Dur et al. 2013). Chick embryos have been imaged with microCT in fixed and live studies. With the high spatial resolution of microCT, Kim and colleagues generated mathematical relationships for volumetric growth of major organ system including the heart (Kim, Min et al. 2011). Using a navigated retrospective gating protocol, Holmes et al determined the cardiac cycle of chick embryos (Holmes, McCabe et al. 2008). The method established by Holmes has to potential for multi-slice imaging, serial imaging of the chick heart longitudinally through cardiogenesis (Holmes, McCabe et al. 2008). Hogers and colleagues have imaged live quail embryos with induced cardiac malformations from clipping the right lateral vitelline vein (Hogers, van der Weerd et al. 2009). Hogers et al obtained high quality MRI images of quails ranging from days 3-11 of development with a spatial resolution of 78-90μm with image slices ranging from 300-500μm (Figure 6) (Hogers, van der Weerd et al. 2009). With each experimental advancement in the use of vertebrate animal models, parallel developments in imaging technologies are required to identify the phenomena and if possible quantify the resulting changes.

1.4 Embryonic Imaging Techniques

Classical imaging of embryonic development was and still is performed either through direct microscopic visualization, which is limited to whatever could be seen on the surface, or through thin section preparations of fixed tissues. While acceptable for largely static tissues, fixation of dynamic tissues can result in atypical morphology that can be mistaken for malformations. Some fixation processes can result in non-negligible and unpredictable changes in organ size. In addition, in-plane imaging of thin sections is always with greater resolution than along the transverse axis, which creates difficulty in resolving highly tortuous anatomy. Even with time consuming three-dimensional (3D) reconstructions, only one data point in time for one embryo is obtained, necessitating multiple embryos with multiple experimental treatments to obtain statistical significance. As each surgery, injection, and/or genetic recombination event is not strictly identical, there is an increased risk of variability. This risk is elevated for rapid and/or dynamic processes that are very sensitive to small changes in local cell phenotypes or environmental factors (growth factors, extracellular matrix, biochemical, etc.) (Hogers, DeRuiter et al. 1999; Munoz-Sanjuan, Simandl et al. 1999; Maciaczyk, Singec et al. 2009). Subtle malformations early in embryonic development can generate detrimental consequences later in development, but without an ability to connect the effect to the cause the critically important origins of these malformations would be missed. Continuous live imaging of embryonic morphogenesis would ensure that all data is obtained and available for analysis, but no imaging system to date can obtain the spatial resolution needed over the depth of field desired at a frame rate fast enough. Currently there are four main imaging modalities for quantitative in vivo

embryonic imaging: 1) optical 2) ultrasound, 3) magnetic resonance imaging (MRI), and 4) micro-computed tomography (microCT). Each of these imaging methods has differences in resolution capabilities, depth of field, acquisition time, and cost (Figure 1.3).

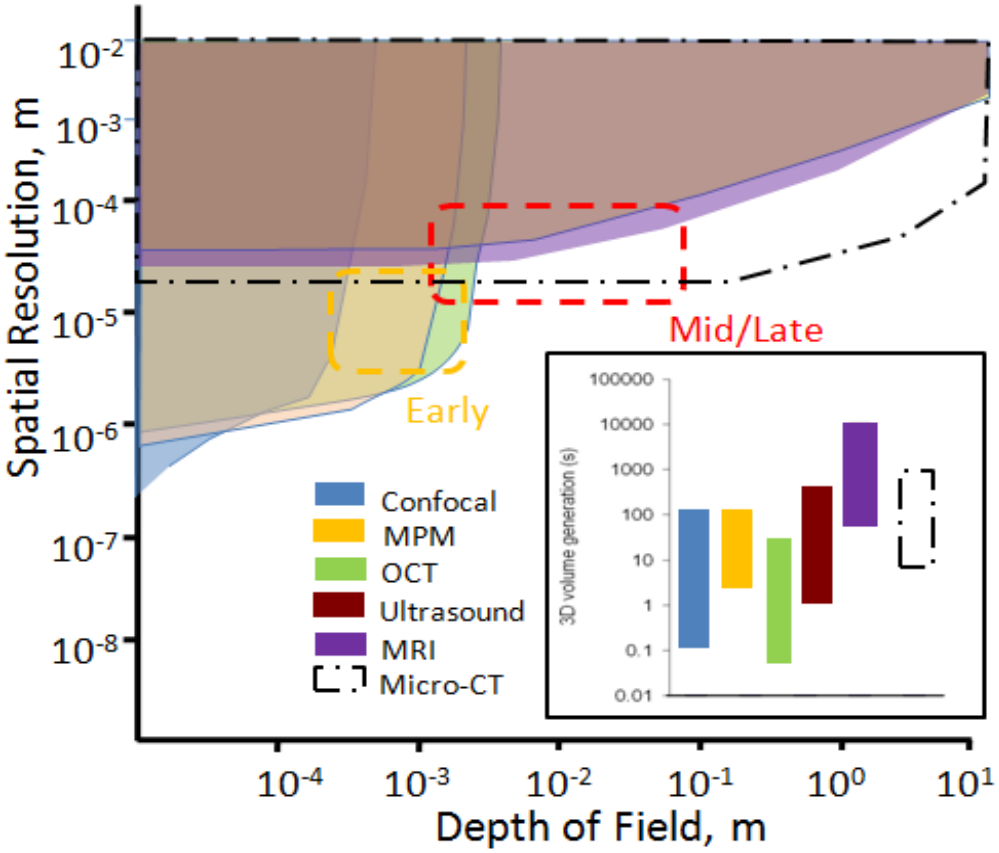

Figure 1.3 - Comparison of common imaging modalities. Spatial resolution vs. depth of field comparison of common optical, ultrasound, MRI, and microCT imaging techniques (Gregg & Butcher, 2012)

1.4.1 Optical Imaging

The compound and stereomicroscope are longstanding essential workhorses to assist in conducting experiments and qualitative observation. The amount and usefulness of

quantitative information is limited to tissue surfaces or very thin slices (<10μm) because of the inability of visible light wavelengths to penetrate into dense media without scattering and difficulties in partitioning light to different transverse-plane depths when creating two dimensional projections of the actual three dimensional tissue; therefore, while these approaches have achieved widespread use in live embryo imaging, they are primarily limited to virtually flat surfaces and or qualitative observations of gross tissue movements.

Confocal fluorescence microscopy has been the most widely used optical imaging technique for quantifying live morphogenesis (Pawley 2006). In general, confocal microscopy is fast and yields a high signal-to-noise ratio, but its depth of view is limited by the light scattering properties of the sample, which for embryonic specimens is a maximum of about 200 μm.

Multi-photon microscopy (MPM) takes advantage of the nonlinear wavelength dependency of light scattering and absorption magnitude. Infrared light (>800 nm) has dramatically reduced scattering through biological tissue, allowing deeper penetration (up to 2 mm) into live specimen samples with reduced toxicity (Denk, Strickler et al. 1990; Squirrell, Wokosin et al. 1999; Dickinson, Simbuerger et al. 2003; Diaspro, Chirico et al. 2005; Helmchen and Denk 2005; McMahon, Supatto et al. 2008; Supatto, McMahon et al. 2009). Like confocal microscopy, spatial resolution remains diffraction limited with the effective resolution dependent on many factors with resulting in comparable resolution capabilities between confocal and multi-photon microscopy (Zipfel, Williams, & Webb, 2003).

Optical coherence tomography (OCT) is an alternative non-invasive imaging modality that takes advantage of optical scattering in a specimen. Typically employing infrared wavelengths, OCT has a greater penetration depth into tissues than focused laser microscopy (up to 3mm) and is more flexible for producing dynamic 3D and 4D datasets across many different embryonic animal models (Kim, Min et al. 2011) (Yang, Gordon et al. 2003; Liu, Wang et al. 2009; Choma, Suter et al. 2010). Though it has high spatial resolution (~10 μm), OCT can suffer from multiple sources of reflectance in a specimen and therefore low signal to noise ratio. .

Optical imaging will continue to be the principle imaging tool for developmental biology inquiry, but with effectiveness limited primarily to early embryonic events. In vivo imaging of later stage morphogenetic and tissue maturation events will necessitate the implementation of alternative imaging techniques with deeper tissue penetration.

1.4.2 Ultrasound Imaging

Ultrasound imaging applies short pulses of high frequency sound waves that scatter when transmitted and/or reflected through tissue. The deeper tissue penetration of sound waves enables ultrasound the unique ability to visualize morphology in later embryonic stages. Furthermore, Doppler blood flow ultrasound imaging is a widely used experimental tool for analyzing the hemodynamic profiles of both normal and diseased states of embryonic development. Ultrasound is therefore very useful to screen embryos for aberrant morphology and hemodynamics phenotypes, whether from targeted genetic mutations or via random mutagenesis experiments (Wessels and

Sedmera 2003; Yu, Shen et al. 2004; Shen, Leatherbury et al. 2005). Doppler ultrasound data coupled with three dimensional image reconstructions via MRI or microCT facilitates in computational fluid dynamics inquiry on hemodynamic profiles in the developing embryo(Yalcin, Shekhar, McQuinn, & Butcher, 2011).

1.4.3 Magnetic Resonance Imaging

Magnetic resonance imaging (MRI) uses the inherent magnetic properties of atomic nuclei to generate an image. MR contrast in soft tissues can be generated without the need of external contrasts through manipulation of spin relaxation events that occur after the radio frequency pulse but with the several undifferentiated and immature cells during early development, achieving high contrast presents a challenge for embryonic imaging (Turnbull and Mori 2007). Long scan times are required (6-24 hours) to generate the high resolution needed for embryonic imaging (Turnbull and Mori 2007); therefore, multiple embryo imaging increases the throughput of phenotyping (Turnbull and Mori 2007). Technical limitations hinder the ability of MRI to be used for live embryonic development studies. The resolution of the image is the limiting factor based on the signal-to-noise ratio (SNR) and scan time. Theoretically, the physical spatial resolution limit is 10μm but in practicality this limit is much larger to have adequate SNR with reasonable scan times. There are current radio frequency coil configurations which are sufficient for murine and avian embryos, but to follow live embryonic development, advances in hardware would be needed such as multi-element phased array coils with optimized fast image sequences to capture from early to late stages of development (Turnbull and Mori 2007).

1.4.4 Micro-Computed Tomography

Micro-computed tomography (microCT) has been used for the past 15 years to quantify complex spatial geometries at small resolutions in embryological research (Butcher, Sedmera et al. 2007). The sample is scanned with high-powered X-ray energy from a single gamma emitter, whose attenuation is registered by a gamma camera opposite the emitter. Attenuation is quantified in Hounsfield units (HU). The image is constructed through back projection based off of 360º discrete rotation angle increments which are a fully registered into a three dimensional near continuous series of planar slices with no registration defects using commercial software (Butcher, Sedmera et al. 2007). The contents of the entire cylindrical bore are imaged, but often a fast scout is performed to limit 3D reconstruction to a small region of interest. The spatial resolution from microCT is usually limited by the pixel density and acquisition dynamics of the gamma camera. Greater image density also requires rapid transmission and storage of very large files. In vivo microCT has the ability to produce voxel sizes less than 10µm (Guldberg, Ballock et al. 2003) but X-ray exposure time is only a few minutes for a full-volume scan for resolutions of 25-50µm resolution (Kim, Min et al. 2011). MicroCT systems have relatively inexpensive upfront costs and little overhead maintenance associated with them with a decrease in scan time as compared to other imaging modalities (Kim, Min et al. 2011).

While microCT has theoretically the highest possible imaging resolution, soft tissue attenuates X-rays poorly. The vast majority of microCT imaging in embryonic development has been performed on fixed tissue specimens soaked with high atomic weight molecules that enhance X-ray attenuation (Metscher 2009; Degenhardt, Wright et al. 2010; Kim, Min et al. 2011). A summary of the most widely used contrast media is given in Table 1.1 (Gregg, Recknagel, & Butcher, 2015). Osmium tetroxide provides the best soft tissue contrast and clear tissue boundaries, but chemical diffusion is

Table 1.1 - Comparison of Common CT Exogenous Tissue Contrast

Contrast Media	Lugol's Solution	Phospho-tungstic Acid	Osmium Tetroxide	Gallocyanin Chromalum	Microfil™	Omnipque™	Visipaque™
Advantages	Rapid, deep penetration, cheap	High levels of contrast, sharp tissue boundaries	Combines with ECM, high levels of contrast	Cell densities and individual cellular resolution	Imaging of negative spaces	Allows for short term imaging	Allows for long term imaging
Limitations	Over stain mineralized tissues	Slow tissue penetration	Toxic with expensive disposal	Overall low level of contrast	Complicated staining protocol	Embryotoxic within 24 hours	Low residence time
Toxic	Yes	Yes	Yes	Yes	Yes	Yes	No

impaired by epithelial layers at later stages of development (Johnson, Hansen et al. 2006; Litzlbauer, Neuhaeuser et al. 2006; Bentley, Jorgensen et al. 2007; Zhu, Bentley et al. 2007; Faraj, Cuijpers et al. 2009; Metscher 2009; Kim, Min et al. 2011). Additional exogenous contrast used for embryonic soft tissues include Lugol's solution, iodine potassium iodide, gallocyanin-chromalum and phosphotungstic acid stains (Bentley, Jorgensen et al. 2007; Metscher 2009; Degenhardt, Wright et al. 2010; Kim, Min et al.

2011). With these methods, microCT have been used to create mathematical relationships for the volumetric growth of the heart, limb, eye, and brain in the chick embryo (Kim, Min et al. 2011). Alternatively, perfusion of a self-casting X-ray dense polymer (Microfil, Flow Tech, Inc.) into the luminal spaces of the embryo generates 3D lumen geometries for volumetric reconstruction and subsequent computational modeling (Butcher, Sedmera et al. 2007; Wang, Dur et al. 2009; Yalcin, Shekhar et al. 2011). None of these agents however, are suitable for live embryonic imaging.

For extension of microCT imaging into live embryonic samples, some technical challenges need to be overcome including 1) the risk of toxic or teratogenic affects of x-rays on live developing embryos and 2) development and characterization of non-toxic, high attenuation exogenous soft tissue contrast. A previous study determined that x-ray radiation of 798mGy, equivalent to the dosage from exposure to daily 50um scans was non-toxic for avian embryos ranging from day 4-10 of development (Henning, Jiang, Yalcin, & Butcher, 2011). Additionally, radiation from a single bolus exposure at 7X the typical scan was also shown to be safe (Henning et al., 2011) ; therefore, radiation exposure from microCT scans is non-toxic and non-teratogenic for live in vivo imaging in avian embryos for 50um 80kV scans. Identification of non-toxic exogenous soft tissue contrast with high attenuation properties is critical for extension of microCT imaging technology into live in vivo samples. Two different iodine based contrast agents, Omnipaque™(iohexol-OP) and Visipaque™ (iodixanol-VP), have been as an in vivo CT contrast agent. In adult animal studies, OP was used to visualize rabbit and rat placentas (Wise, Xue et al. 2010) and VP has been used in humans to image the coronary arteries and in mice to quantify kidney volumes (Almajdub, Magnier et al.

2008; van Soest, Goderie et al. 2010). In avian embryos, OP was toxic within 24 hours post microinjection into samples due to hyper-osmotic conditions of the media whereas VP was safe for embryonic use for days4-10 of development (Henning et al., 2011). VP and the like transiently affect basic blood properties (hematocrit, viscosity, volume) without causes lasting deleterious effects (Scheller et al., 1999). The iso-osmotic property of VP is critical for embryo survivability whereas this is less critical within adult systems (Nebuloni, Kuhn, & Müller, 2013; Scheller et al., 1999). With the continuous remodeling and immature tissue properties during embryogenesis, free molecule contrast media do not persist in embryos for more than 1 day. Additionally, free molecules are limited to only visualizing the entire sample without delineation in the underlying biological mechanisms that are occurring. Development and characterization of high radiopaque exogenous soft tissue contrast agents is fundamental for the use and efficacy of live in vivo microCT imaging of mid-late stage embryonic morphogenesis.

1.5 Nanoparticle Exogenous Contrast Media

One of the largest limiting factors of microCT is the lack of available exogenous soft tissue contrast agents for extension of this technology into live samples. Iodine based molecules have been the standard contrast media for x-ray and CT imaging. Development and characterization of persistent, highly attenuating exogenous contrast media is critical for longitudinal term spatial and temporal quantitative analysis of live embryonic morphogenesis. Nanoparticles have demonstrated long residence times and

high levels of x-ray attenuation becoming a promising option for embryonic imaging contrast (Ashton et al., 2014; Boll et al., 2011; Lee et al., 2014; Nebuloni et al., 2013). Nanoparticles can be fabricated out of multiple materials (gold, earth metals, tungsten, liposomes encapsulating VP) and have been a prominent part of cancer research as an imaging and delivery tool (Melancon et al., 2014; Zarschler et al., 2014). The use of nanoparticle based soft tissue contrast presents the questions of particle toxicity and stipulations for the use in live embryonic systems. Previous studies and literature reviews outline the known toxicity of gold nanoparticles with several metrics including MTT assays for metabolic disruption, apoptosis, and oxidative stress (Aillon, Xie, El-Gendy, Berkland, & Forrest, 2009; Jia et al., 2009; Pan et al., 2009). Some of the most influential attributes of nanoparticles that result in toxic effects to cell populations include particle size, dose, and surface charge. Pan and colleagues found that smaller particles (<2nm) exhibit mitochondrial damage, necrosis, and oxidative stress whereas 15nm gold particles did not (Pan et al., 2009) and particles less than a couple of nanometers in diameter have shown to have chemical reactivity that is not observed with larger sized particles (Turner et al., 2008). Furthermore, studies have indicated that cationic particles display toxic effects suspected of malignant interactions with the negatively charged cellular membrane whereas the anionic counterpart to these particles were non-toxic (Goodman, McCusker, Yilmaz, & Rotello, 2004). Additionally, nanoparticles have a surface for biomolecule conjugation with known surface chemistry resulting in molecular targeting experiments for different tissue types (Melancon et al., 2014; Wen et al., 2001).

1.6 Image Processing: Acquisition, Restoration, and Analysis

Pre- and post-processing techniques extend the power of the individual imaging modality. These can be broken into three categories: 1) image acquisition 2) image restoration, and 3) image analysis (Khairy and Keller 2011). For a dynamic system, specifying the timing of image acquisition – called gating – is essential to limit motion artifacts. Gating can be designed and performed during imaging (prospective), or established after the image dataset has been acquired (retrospective). Prospective gating synchronizes image acquisition to specific instances within a periodic (repetitive) signal emitted by the specimen. Because an electrocardiogram is not available in an embryo, usually the physical motion of the heart or large vessel is tracked. This has been achieved optically (Chan, Lin et al. 2009; Taylor, Saunter et al. 2011) or through simultaneous blood velocity tracking (Deng, Birkett et al. 2001; Herberg, Goldberg et al. 2005; Jenkins, Chughtai et al. 2007). Retrospective gating is achieved by acquiring all possible images in a dataset, and then sorting them based on periodic spatial or temporal signals. This approach has been employed for embryonic heart development imaging by taking advantage of unique non-symmetric myocardial cross-sections for each imaging plane and phase of cardiac cycle (Liebling, Forouhar et al. 2005). Alternatively, a separate signal can be taken at the same time as the imaging, or extracted separately after imaging, and then used to separate each image. Retrospective imaging requires tremendous amounts of data to be rapidly acquired and stored, while prospective gating is data efficient but difficult to implement in an embryo.

Image restoration improves boundary detection and local contrast in an image dataset. Two key approaches are deconvolution and registration. Deconvolution of blurred

objects is achieved through estimation of the spread of the data points and restoring them to their “true” locations (Lucy 1974; Markham and Conchello 1999). Point spread functions can either be assumed directly or derived directly from the datasets, the latter being the most computationally intense (Racine, Sachse et al. 2007). For image registration, spatially mis-aligned images are translated and/or transformed based on deviation from a defined reference frame (Khairy and Keller 2011). This reference can be a an externally applied marker (e.g. hole or region of high scatter/contrast), or ascribed relatively through neighboring images(Brown 1992; Zitova and Flusser 2003). Both deconvolution and registration can and has been employed with gating processes to improve image quality.

Image analysis translates the intensity of each image voxel into digital information that can be quantified and compared. For example, image segmentation delineates anatomic structures and tissue geometries, while thresholding bins the intensity of a voxel to assign values relevant to the study. Numerous algorithms have been developed and implemented for these purposes and are found in common imaging applications such as ImageJ through the National Institutes of Health (Khairy and Keller 2011). Once obtained, these datasets can also be used in computational modeling, simulating biological conditions to estimate local and global functional parameters that cannot be measured directly.

1.7 Research Objectives

The overall motivation for the work contained in this dissertation and for the future scientific questions to come is to have quantitative analysis of embryonic morphogenesis during the clinically relevant mid-late stages for the evaluation of structure-function relationships imperative for understanding normal and abnormal tissue assembly. A multi-scale synergistic understanding is critical for parsing out biomechanical and biochemical influences on tissue behavior with experimental and computational tools required for all scales of analysis. The overall flow of the many input and output factors during development are given in Figure 1.4. The work presented in this dissertation focuses on the morphological consequences of normal embryonic development concurrent with the development of new engineering strategies

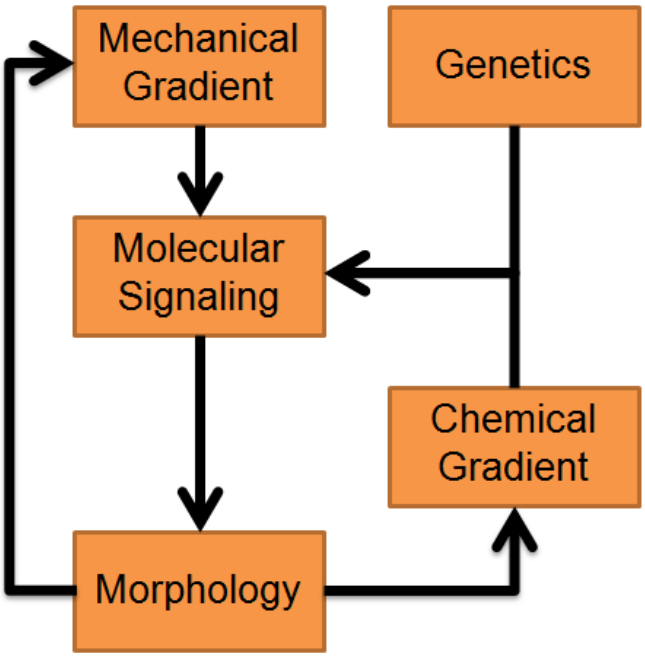

Figure 1.4 - Flow diagram of mechanical, chemical, and genetic inputs for morphogenesis. The factors influencing molecular signaling resulting in changes in morphology

for 3D live analysis. More specifically, the objective of the work presented here is to develop new and adapt current technologies for live in vivo microCT imaging of avian morphogenesis during the mid-late stages of development through the implementation of nanoparticle based contrast media and prospectively gated image analysis. To accomplish this I screened and characterized the use of commercially purchased metallic nanoparticles for use as exogenous soft tissue contrast determining their toxicity, persistence, and spatial/temporal biodistribution over 24 hours within the developing embryo. Using the most effective metallic nanoparticles for use in embryos, I analyzed longitudinal use of these particles ranging from days 4-11 of development. Specifically I quantified the biodistribution through modeling the bulk particle movements by analysis of the temporal and spatial contrast enhancement changes over 24 hour periods of time with measurements taken in the heart, dorsal aorta, head, and limb. Characterization and quantification of anatomical changes was completed based on live in vivo image datasets resulting in methods to noninvasively and nondestructively analyze longitudinal changes in morphogenesis. Furthermore, I developed a method for quantifying bulk particle transport from large vascular structures into the surrounding tissue indicative of basic transport relationships changing during morphogenesis. For dynamic analysis of cardiovascular changes during morphogenesis, I developed a means for gating image acquisition during the embryonic cardiac cycle with specified acquisition points with the goal of assessing function at peak systole and peak diastole. This technology development was addressed through three different aims:

1.7.1 - Aim 1 (Chapter 2): Characterization of commercially available metallic nanoparticles for use as a non-toxic exogenous soft tissue contrast media for live in vivo microCT imaging of avian embryonic development

We established the dose dependent toxicity, persistence, and biodistribution of three different metallic nanoparticles believing that the spatio-temporal dynamics of the contrast, biodistribution, and persistence are size dependent. We chose to examine 1.9nm gold nanoparticles (1.9nm AuNP), 15nm gold nanoparticles (15nm AuNP), and 110nm alkaline earth metal particles (110nm EXTN) based on their previous use and efficacy found in the literature in adult animal model systems. For extension of into embryonic systems, we established that the nanoparticle dosage cannot exceed 20% blood volume. We found that 1.9nm AuNPs are toxic by 8 hours post injection; therefore, are only a viable imaging option for imaging soon post injection. The 15nm AuNPs and 110nm EXTN particles were non-toxic and persisted 8 hours and 24 hours respectively in the embryo where contrast enhancement was discernible from the background albumen attenuation. Longitudinal biodistribution was modeled in the heart, dorsal aorta, head, limb, and allantois where it was found that cardiovascular structures have significantly higher contrast enhancement immediately post injection. Relative perfusion quantification was established from bulk particle movement out of the dorsal aorta into the flank mesenchyme over 8 hours post injection. We conclude that particle size and material composition is critical for embryo survivability and contrast enhancement, facts supported in the literature, but we found that larger particles are essential for longitudinal studies of embryonic development with increased tissue persistence. Furthermore, with known injection volumes and particle solution concentrations transport phenomena can be readily quantified spatially and temporally.

We found that the spatio-temporal dynamics are heavily influenced by particle size as hypothesized. The results from this study demonstrate the importance of nanoparticle contrast media selection and how particle size is imperative for determining spatial and temporal information.

1.7.2 - Aim 2 (Chapter 3): Longitudinal Quantitative Three Dimensional Assessment of Live Embryonic Morphogenesis during Mid-Late Stages of Development via In Vivo MicroCT Imaging

Longitudinal analysis of live morphogenesis is essential for parsing out tissue-scale changes. Using the most optimal 110nm EXTN nanoparticle, we imaged chick embryos ranging from days 4-11 for a 24 hour period of time after injection believing that the spatio-temporal dynamics of the contrast, biodistribution, and persistence are age and organ specific reflecting increasing tissue heterogeneity longitudinally. Analysis extended to model development of persistence and biodistribution within embryos of varying ages with complementary virtual histology sections representative of 24 hour bulk particle movement and organ identification. Spatial quantification of bulk nanoparticle concentration and movement over 24 hours was found into the left and right myocardial walls determining inherent differences of the myocardium that is side and age specific. Additionally, we quantified real time organ growth metrics of the heart, lungs, and eyes determining consistent but organ specific growth. We conclude that complex tissue morphogenesis is readily visualized and quantified through non invasive, high resolution live in vivo microCT imaging during the mid-late stages of avian embryogenesis. Furthermore, we have quantitatively determined spatial tissue variation

within the myocardium through determination of bulk particle movement divergence. This study represents critical advancements in three dimensional high resolution live embryonic imaging and the tissue metric quantification capable through this technology, an imperative step towards quantifying normal and abnormal morphogenesis with clinically relevant consequences.

1.7.3 - Aim 3 (Chapter 4): Prospective gated image analysis of functional, dynamic heart changes during mid-late stage cardiogenesis

Live, dynamic heart imaging during the mid-late stages of development is critical for elucidating information that is impossible to gather from traditional fixed 3D specimens including but not limited ventricular shape and volume changes, spatio-temporal blood distribution changes, and dynamics of morphology and trabecular structure believing that these morphodynamics can be revealed with the use of prospective gated image acquisition coupled with 3D microCT imaging. We fabricated a prospectively gated image system compatible with the microCT capable of acquiring the cardiac cycle and processing the signal into user defined trigger points within the sinusoid. Furthermore, we established dynamic metrics of day 9 and day 11 embryonic hearts through evaluation of chamber volume changes between peak systole and peak diastole. We quantitatively defined ejection fraction both dynamically with the cyclic changes at a given embryonic age and functionally by following changes as a result from tissue maturation. Contour and surface plots reveal relative blood concentration, distribution, and morphology changes of the right and left ventricles during systole and diastole. Trabecular density analysis reveals trending differences within the cardiac cycle that

demonstrate relatively higher trabecular density during ventricular contraction. We conclude that the mid-late stage embryonic heart can be successfully prospectively gated with live in vivo microCT imaging. Additionally, we determined quantitative metrics of functional consequences during normal heart development not readily obtained in live three dimensional datasets prior to this technology and impossible to determine through fixed tissue specimens. This technology will enable functional, dynamic downstream physiological consequences to be realized in mid-late stage cardiogenesis for in abnormal and normal morphogenesis.

1.7.4 Summary

Three dimensional live in vivo imaging is a powerful and much needed tool in the field of embryological research. Mid-late stage embryogenesis is a critical and much evasive part of developmental biology that has not been readily visualized in live samples to date. Here we demonstrate the development of new and adaptation of current imaging technologies for live in vivo imaging of embryonic morphogenesis during mid-late stages of development through the implementation of nanoparticle based contrast media and prospectively gated image acquisition with graphical delineation of my aims and hypotheses given in Figure 1.5. Because live studies of embryogenesis during these stages has been largely elusive, it is my hope that this work will propel the field of embryological imaging and morphogenetic studies forward by providing quantitative information for specific structure function relationship studies.

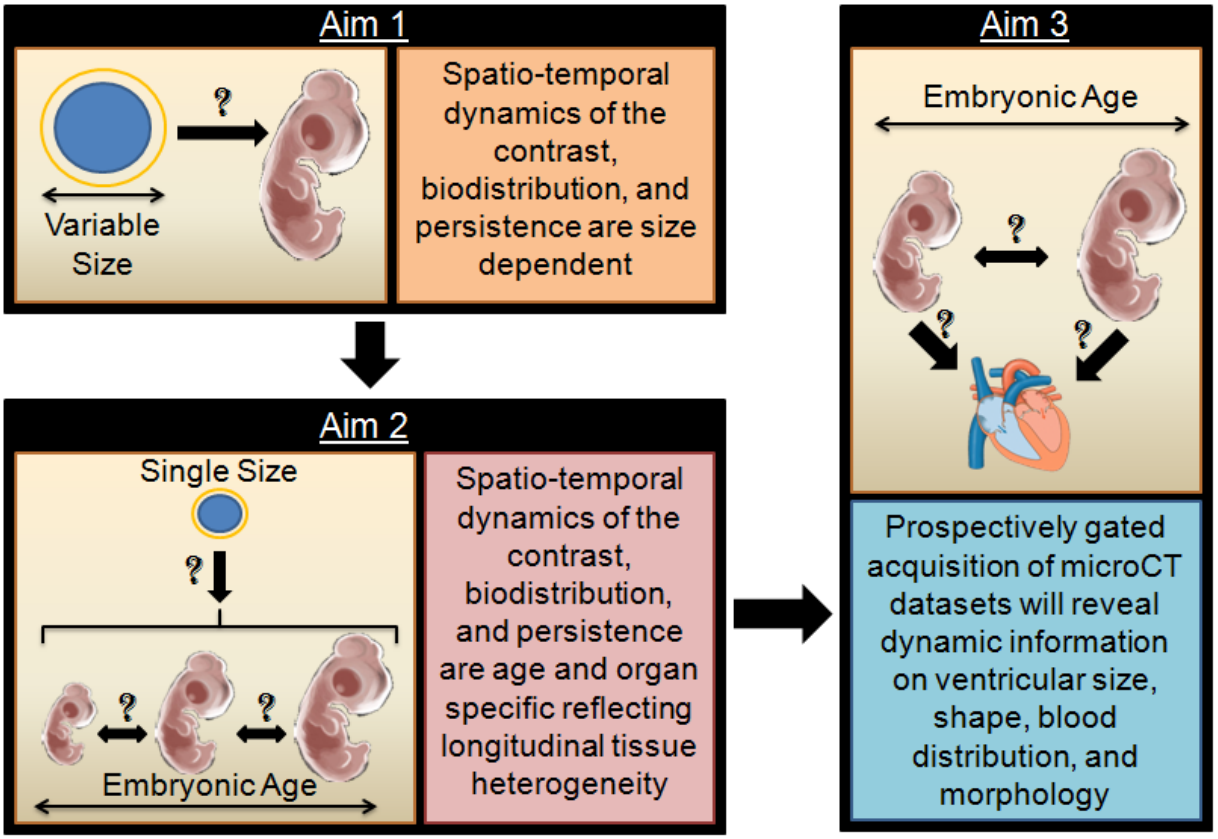

Figure 1.5 - Illustration of dissertation specific aims with corresponding hypotheses

References

Aillon, K. L., Xie, Y., El-Gendy, N., Berkland, C. J., & Forrest, M. L. (2009). Effects of nanomaterial physicochemical properties on in vivo toxicity. *Advanced Drug Delivery Reviews*, *61*(6), 457–466. http://doi.org/10.1016/j.addr.2009.03.010

Ashton, J. R., Clark, D. P., Moding, E. J., Ghaghada, K., Kirsch, D. G., West, J. L., & Badea, C. T. (2014). Dual-energy micro-CT functional imaging of primary lung cancer in mice using gold and iodine nanoparticle contrast agents: a validation study. *PloS One*, *9*(2), e88129. http://doi.org/10.1371/journal.pone.0088129

Boll, H., Nittka, S., Doyon, F., Neumaier, M., Marx, A., Kramer, M., … Brockmann, M. a. (2011). Micro-CT based experimental liver imaging using a nanoparticulate contrast agent: a longitudinal study in mice. *PloS One*, *6*(9), e25692. http://doi.org/10.1371/journal.pone.0025692

Coffin, J. D., & Poole, T. J. (1988). Embryonic vascular development: immunohistochemical identification of the origin and subsequent morphogenesis of the major vessel primordia in quail embryos. *Development (Cambridge, England)*, *102*(4), 735–48. Retrieved from http://www.ncbi.nlm.nih.gov/pubmed/3048971

Darnell, D. K., & Schoenwolf, G. C. (2000). The chick embryo as a model system for analyzing mechanisms of development. *Methods in Molecular Biology (Clifton, N.J.)*, *135*, 25–9. Retrieved from http://www.ncbi.nlm.nih.gov/pubmed/10791301

Goodman, C. M., McCusker, C. D., Yilmaz, T., & Rotello, V. M. (2004). Toxicity of gold nanoparticles functionalized with cationic and anionic side chains. *Bioconjugate*

Chemistry, *15*(4), 897–900. http://doi.org/10.1021/bc049951i

Gregg, C. L., & Butcher, J. T. (2012). Quantitative In Vivo Imaging of Embryonic Development: Opportunities and Challenges. *Differentiation*, *84*(1), 149–162. http://doi.org/10.1016/j.diff.2012.05.003.Quantitative

Gregg, C. L., & Butcher, J. T. (2013). Translational paradigms in scientific and clinical imaging of cardiac development. *Birth Defects Research. Part C, Embryo Today : Reviews*, *99*(2), 106–20. http://doi.org/10.1002/bdrc.21034

Gregg, C. L., Recknagel, A. K., & Butcher, J. T. (2015). Micro/Nano-Computed Tomography Technology for Quantitative Dynamic, Multi-scale Imaging of Morphogenesis. *Methods in Molecular Biology (Clifton, N.J.)*, *1189*, 47–61. http://doi.org/10.1007/978-1-4939-1164-6

Henning, A. L., Jiang, M. X., Yalcin, H. C., & Butcher, J. T. (2011). Quantitative three-dimensional imaging of live avian embryonic morphogenesis via micro-computed tomography. *Developmental Dynamics : An Official Publication of the American Association of Anatomists*, *240*(8), 1949–57. http://doi.org/10.1002/dvdy.22694

Hogers, B., DeRuiter, M. C., Gittenberger-de Groot, a C., & Poelmann, R. E. (1999). Extraembryonic venous obstructions lead to cardiovascular malformations and can be embryolethal. *Cardiovascular Research*, *41*(1), 87–99. Retrieved from http://www.ncbi.nlm.nih.gov/pubmed/10325956

Jia, H. Y., Liu, Y., Zhang, X. J., Han, L., Du, L. B., Tian, Q., & Xu, Y. C. (2009). Potential oxidative stress of gold nanoparticles by induced-NO releasing in serum. *Journal of*

the American Chemical Society, *131*(1), 40–41. http://doi.org/10.1021/ja808033w

Lamers, W. H. (2002). Cardiac Septation: A Late Contribution of the Embryonic Primary Myocardium to Heart Morphogenesis. *Circulation Research*, *91*(2), 93–103. http://doi.org/10.1161/01.RES.0000027135.63141.89

Le Douarin, N. M. (2008). Developmental patterning deciphered in avian chimeras. *Development, Growth & Differentiation*, *50 Suppl 1*(December 2007), S11–28. http://doi.org/10.1111/j.1440-169X.2008.00989.x

Lee, C.-L., Min, H., Befera, N., Clark, D., Qi, Y., Das, S., … Kirsch, D. G. (2014). Assessing Cardiac Injury in Mice wit hDual Energy-microCT, 4D-microCT and microSPECT Imaging Following Partial-Heart Irradiation. *Int. J Radiat Oncol Biol Phys*, *88*(3), 686–693. http://doi.org/10.1016/j.ijrobp.2013.11.238.Assessing

Manner, J. (2000). Cardiac Looping in the Chick Embryo : A Morphological Review With Special Reference to Terminological and Biomechanical, *262*(March), 248–262.

Melancon, M. P., Zhou, M., Zhang, R., Xiong, C., Allen, P., Wen, X., … Li, C. (2014). Selective uptake and imaging of aptamer- and antibody-conjugated hollow nanospheres targeted to epidermal growth factor receptors overexpressed in head and neck cancer. *ACS Nano*, *8*(5), 4530–8. http://doi.org/10.1021/nn406632u

Nebuloni, L., Kuhn, G. a, & Müller, R. (2013). A comparative analysis of water-soluble and blood-pool contrast agents for in vivo vascular imaging with micro-CT. *Academic Radiology*, *20*(10), 1247–55. http://doi.org/10.1016/j.acra.2013.06.003

Pan, Y., Leifert, A., Ruau, D., Neuss, S., Bornemann, J., Schmid, G., … Jahnen-

Dechent, W. (2009). Gold Nanoparticles of Diameter 1.4 nm Trigger Necrosis by Oxidative Stress and Mitochondrial Damage. *Small*, *5*(18), 2067–2076. http://doi.org/10.1002/smll.200900466

Patten, B. M., Akd, K., & Barry, A. (n.d.). VALVULAR ACTION IN T H E EMBRYONIC.

Scheller, B., Hennen, B., Thünenkötter, T., Mrowietz, C., Markwirth, T., Schieffer, H., & Jung, F. (1999). Effect of X-ray contrast media on blood flow properties after coronary angiography. *Thrombosis Research*, *96*(4), 253–60. Retrieved from http://www.ncbi.nlm.nih.gov/pubmed/10593427

Turner, M., Golovko, V. B., Vaughan, O. P. H., Abdulkin, P., Berenguer-Murcia, A., Tikhov, M. S., … Lambert, R. M. (2008). Selective oxidation with dioxygen by gold nanoparticle catalysts derived from 55-atom clusters. *Nature*, *454*(7207), 981–983. http://doi.org/10.1038/nature07194

Wen, X., Wu, Q. P., Lu, Y., Fan, Z., Charnsangavej, C., Wallace, S., … Li, C. (2001). Poly(ethylene glycol)-conjugated anti-EGF receptor antibody C225 with radiometal chelator attached to the termini of polymer chains. *Bioconjugate Chemistry*, *12*(4), 545–53. Retrieved from http://www.ncbi.nlm.nih.gov/pubmed/11459459

Wilson, J. G., Roth, C. B., & Warkany, J. (1953). An analysis of the syndrome of malformations induced by maternal vitamin A deficiency. Effects of restoration of vitamin A at various times during gestation. *The American Journal of Anatomy*, *92*(2), 189–217. http://doi.org/10.1002/aja.1000920202

Xin, M., Olson, E. N., & Bassel-duby, R. (2013). Mending broken hearts: cardiac

development as a basis for adult heart regeneration and repair. *Nature Reviews. Molecular Cell Biology*, *14*(8), 529–541. http://doi.org/10.1038/nrm3619.Mending

Yalcin, H. C., Shekhar, A., McQuinn, T. C., & Butcher, J. T. (2011). Hemodynamic patterning of the avian atrioventricular valve. *Developmental Dynamics : An Official Publication of the American Association of Anatomists*, *240*(1), 23–35. http://doi.org/10.1002/dvdy.22512

Zarschler, K., Prapainop, K., Mahon, E., Rocks, L., Bramini, M., Kelly, P. M., … Dawson, K. a. (2014). Diagnostic nanoparticle targeting of the EGF-receptor in complex biological conditions using single-domain antibodies. *Nanoscale*, *6*(11), 6046–56. http://doi.org/10.1039/c4nr00595c

Zipfel, W. R., Williams, R. M., & Webb, W. W. (2003). Nonlinear magic: multiphoton microscopy in the biosciences. *Nature Biotechnology*, *21*(11), 1369–1377. http://doi.org/10.1038/nbt899

CHAPTER 2

COMPARATIVE ANALYSIS OF METALLIC NANOPARTICLES AS EXOGENOUS SOFT TISSUE CONTRAST FOR LIVE IN VIVO MICRO-COMPUTED TOMOGRAPHY IMAGING OF AVIAN EMBRYONIC MORPHOGENESIS

Accepted for publication in Developmental Dynamics (2016)

2.1 Abstract

Clinically relevant congenital malformations arise during mid-late stages of development that are inaccessible in vivo with traditional optical imaging. MicroCT is an attractive technology to rapidly and inexpensively generate quantitative 3D datasets but requires exogenous soft tissue contrast. Here we establish dose dependent toxicity, persistence, and biodistribution of three different metallic nanoparticles in day 4 chick embryos. We determined that 110nm alkaline earth metal particles were non-toxic and persisted in the chick embryo for up to 24 hours post injection with contrast enhancement levels at high as 1600HU. 15nm gold nanoparticles persisted with contrast enhancement higher than that of background for up to 8 hours post injection, while 1.9nm particles resulted in lethality by 8 hours. We identified spatial and temporally heterogeneous contrast enhancement ranging from 250-1600HU in the heart, dorsal aorta, head, limb, and allantois. We further quantified an exponential increase in the tissue perfusion coefficient versus distance from the dorsal aorta into the flank over 8 hours with a peak perfusion rate of 0.7um^2/s measured at a distance of 0.3mm. These results

demonstrate the safety, efficacy, and opportunity of nanoparticle based contrast media in live embryos for quantitative analysis of embryogenesis.

2.2 Introduction

Embryonic development is a rapid and dynamic three-dimensional process characterized by the growth and differentiation of progenitor cell populations into a complex network of organs and supporting tissues. Though much has been learned about the gross anatomical changes that occur during morphogenesis, elucidating the mechanistic interplays between underlying biomechanical and biochemical cues is critical for integrating the genetic and environmental influences on tissue behavior. Outside of the earliest stages of development, our understanding of this highly dynamic process has been gleaned primarily from static reconstructions of animal models. This gap obscures our knowledge of relative growth rates, prioritization, and distinction between association and causality. Genetic mutations that alter early stage patterning are nearly always embryonic lethal, but clinically survivable malformations arise during the mid-late stages of development after initial fate specification and tissue patterning have begun (Roger et al., 2010). Propagation of even subtle abnormalities at these stages can lead to congenital defects with a range of severities, origins that are largely unknown, and potentially bleak prognoses (Gregg & Butcher, 2013).

High resolution, quantitative dynamic imaging technologies are therefore essential for capturing these emerging knowledge needs in embryonic development. Although high resolution 3D reconstructions from histological sections are commonplace, these are static representations of post-vital organisms. Optical resolution is unparalleled within

the sectioning plane but out of plane 3D interpolation between multiple sections is time consuming and suffers from inherent error in embedding and sectioning.

The vast majority of live embryonic inquiry has focused on the early events of development spanning gastrulation and heart tube formation with the onset of beating (Cui et al., 2013; Czirók, Rongish, & Little, 2004; Zamir, Czirók, Cui, Little, & Rongish, 2006). Confocal and multiphoton microscopy with excitable and infrared fluorophores is capable of imaging up to 2mm in live samples (Diaspro, Chirico, & Collini, 2005; Dickinson, Simbuerger, Zimmermann, Waters, & Fraser, 2003; Squirrell, Wokosin, White, & Bavister, 1999; Supatto et al., 2005; Supatto, Mcmahon, Fraser, & Stathopoulos, 2009) with limited capacity once the tissue becomes dense and light scattering beyond the earliest stages of development. Live embryonic studies conducted during mid-late stages of development are more limited, requiring a reliable animal model and high resolution, wide field, deep tissue imaging.

Live in vivo imaging with ultrasound and magnetic resonance imaging (MRI) often suffer from restrictions in field of view, signal-to-noise ratio, and differential tissue contrast (Metscher, 2009). Ultrasound is widely used for screening hemodynamic profiles in developing embryos and couples nicely with three dimensional reconstructions for further computation analysis of fluid-solid tissue interactions (Shen et al., 2005; Wessels & Sedmera, 2003; B. Yu et al., 2015; Q. Yu et al., 2004). Whole specimen MRI studies are emerging as rf coil design and post-processing techniques improve, but MRI remains an expensive and a lengthy scanning process (especially for very high resolutions) requiring additional considerations for environmental control to maintain

healthy, viable samples (Gregg & Butcher, 2012). Micro-computed tomography (microCT) is an attractive three dimensional whole specimen imaging technology for morphogenetic inquiry having the resolution and depth of field required to capture mid-late stages of embryonic development with high fidelity at a fraction of the cost of MRI (Gregg & Butcher, 2012).

MicroCT has been a valuable imaging tool for the past 15 years in the field of embryological research characterizing tortuous anatomy with high spatial and temporal resolution (Butcher, Sedmera, Guldberg, & Markwald, 2007). MicroCT imaging produces high resolution three dimensional datasets within minutes at a fraction of the cost of similar technologies (Kim, Min, Recknagel, Riccio, & Butcher, 2011). Advancements in CT dense contrast media and sophisticated protocols enable high tissue boundary identification with general and molecularly targeted exogenous soft tissue contrast (Butcher et al., 2007; Gregg, Recknagel, & Butcher, 2015; Metscher & Müller, 2011; Metscher, 2009; Yalcin, Shekhar, McQuinn, & Butcher, 2011). MicroCT imaging can readily identify multiple and broad three dimensional morphological consequences of transgenic modifications on fixed developing embryos (Degenhardt, Wright, Horng, Padmanabhan, & Epstein, 2010; Johnson et al., 2006). Furthermore, whole mount staining with antibody probes and metal immunodetection has yielded tissue patterning data in the developing chick embryo (Gregg et al., 2015; Metscher & Müller, 2011). Coupled three dimensional microCT anatomical data with Doppler ultrasound has shown to be a power tool for computational analysis of hemodynamic patterning in the developing chick heart (Yalcin et al., 2011).While microCT has served

a much needed purpose for high resolution, deep tissue imaging of embryos, the inability to gather longitudinal (time course) data from the same embryo necessitates the preparation of multiple samples for single time points, increasing experimental variability particularly if genetic perturbations or microsurgical manipulations are present. It is essential to extend microCT imaging to live samples to address these limitations. We previously established the possibility for non-toxic live microCT imaging using Visipaque™ (VP) in an avian embryo model (Henning, Jiang, Yalcin, & Butcher, 2011). We showed that radiation from scans up to 7X higher than typical scan dosage did not cause morphological defects for embryos up to day 10 of development. Iodine based molecules, such as VP, have been the standard contrast media for x-ray and CT images proving themselves safe and effective (Scheller et al., 1999). Such free molecule contrast media are < 1 nm, and therefore extravasate quickly with dramatic reduction in contrast after a few hours, too short for meaningful longitudinal analysis from a single injection. Injectable nanoparticle technology has achieved long residence times and high levels of x-ray attenuation, motivating their potential as embryonic imaging contrast (Ashton et al., 2014; Boll et al., 2011; Lee et al., 2014; Nebuloni, Kuhn, & Müller, 2013). Nanoparticles, which can be fabricated out of multiple materials (e.g. gold, earth metals, tungsten, liposomes encapsulating VP), have been used extensively in cancer research as an imaging and delivery tool (Melancon et al., 2014; Zarschler et al., 2014). Additionally, biomolecule conjugation to the nanoparticle surface enables targeting of different tissue types (Melancon et al., 2014; Wen et al., 2001). Nanoparticle based CT contrast media has not been extended to live embryonic imaging to date. In this study we address longitudinal use of nanoparticle based exogenous soft tissue

contrast for live microCT imaging of embryonic development in the avian embryo. Intravenous delivery and toxicity of three different metallic nanoparticles were assessed. Furthermore, we analyzed particle material and size contributions on spatial and temporal contrast enhancement of day 4-5 embryos. Lastly, we quantified relative perfusion characteristics via bulk particle movements in embryonic tissue.

We demonstrate that alkaline earth 110nm metallic nanoparticles are more radiopaque within the embryo than their 15nm and 1.9nm gold nanoparticle counterparts. Additionally, we found that the 110nm particles persist longest in the embryo and yields high tissue boundary delineation with time dependent and organ dependent contrast enhancement. The 15nm gold nanoparticles persisted for at least 8 hours post injection and the 1.9nm gold nanoparticles extravasated quickly out of the vasculature into the embryonic tissue and were toxic to the embryo by 8 hours post injection. Lastly, we quantified relative diffusion of the 110nm alkaline earth metal particles moving out of the dorsal aorta into the surrounding tissue based on transient contrast enhancement changes.

2.3 Materials and Methods

Preparation of embryonic samples and in vivo microinjections

White leghorn eggs (Cornell Poultry) were incubated for 3 days at 99.5˚F and 55% humidity. After three days, embryos were cultured in ovo from a method previously described in (Nakamura & Funahashi, 2001). Eggs were cleaned with 70% ethanol and a small opening was created at the narrow end of the egg with the point of sterile

dissection scissors. Approximately 6-7mL of albumin was removed using a 21 gauge needle and the opening was secured with a small piece of masking tape. Two large strips of masking tape were placed down the egg and a small window was made in the egg shell using curved dissection scissors allowing visualization of the embryo. The window was covered with sterilized plastic wrap. Following in ovo culture, the embryos were housed in sterilized Styrofoam incubators maintained at appropriate temperature and humidity for proper development for the duration of the experiment.

A gravity driven pressure gradient and micromanipulator was used to microinject chick embryos as previously described by Butcher and colleagues (Butcher et al., 2007) (Figure 2.1). Borosilicate capillary tubes (OD 1.00mm, ID 0.75mm) were drawn into microneedles and beveled at a 45˚ angle using a microforge forming needles 20µm in diameter. Soft tissues were visualized through a dissecting light microscope and contrast media was injected through extraembryonic vessels in the vitelline network (Figure 2.1).

Contrast media toxicity based on heart rate and morphology

Day 3 chick embryos were injected with approximately 10% blood volume, in line with previously described literature (Henning et al., 2011). Three different nanoparticles were tested: a 110nm alkaline earth metal particles (110nm EXTN, Miltenyi Biotec. Inc.) and two gold nanoparticles (1.9nm AuNP, 15nm AuNP, Nanoprobes Inc.). The heart rate was monitored immediately before and after injection, 1 hour, and 24 hour post-injection. Earl's balanced salt solution (EBSS) served as an injection sham control. At

day 10 of development, the embryos were sacrificed and fixed in 4% paraformaldehyde (PFA). Images of the embryos were taken on a stereo Zeiss microscope and anatomical measurements were analyzed in ImageJ. The wing length (WL), foot length (FL), eye diameter (ED), and crown-rump length (CRL) were measured in triplicate for each sample. The WL and FL were measured from the bend the limb to the furthest tip following the curvature of the limb. The eye diameter was measured across the middle of the eye with the head aligned flat with the microscope and the CRL was measured from the tip of the beak to the tail following the curvature from the ventral side of the face, following cranial to the top of the head and then caudally down the backside to the tail. All sample measurements were compared against EBSS injected controls.

In vivo microCT scanning

Nanoparticle injected embryos were taken from the portable Styrofoam incubator and placed in a custom built polycarbonate imaging chamber. All imaging was completed on a GE Healthcare eXplore CT 120 scanner. Embryos were scanned at 50µm for 5 minutes with a total of 800 projections with a voltage of 80kV. Post-processing was completed in MicroView (GE Healthcare) for quantification of contrast levels and OsiriX (Apple) for three dimensional reconstructions. Contrast intensity gray scale values were converted to Hounsfield units (HU), correlating to bone material density (Badea et al 2008) from calibration to a bone standard (SB3, GE).

Image analysis and quantification

Virtual 2D cross sections were analyzed in MicroView using the Line Tool, measuring the contrast intensity of the heart, dorsal aorta, limb, head, and allantois (Figure 2.1). Contrast enhancement and degradation were modeled over a 24 hour period of time. DICOM image stacks were imported into OsiriX and used to produce maximum intensity projections (MIP) and volumetric renderings (VR) of representative day 4 samples.

Particle perfusion quantification from the dorsal aorta immediately post injection and 8 hour post injection images were used for contrast enhancement measurements at known distance from the dorsal aorta. Measurements were taken parallel to the dorsal aorta at known variable distances in multiple (n = 3) embryos. Contrast enhancement inside the dorsal aorta at 0 hours was used as the initial concentration value based on the contrast enhancement. All measurements were normalized to the background contrast (albumin and yolk). We approximated the flank perfusion as a radially symmetric process (emanating from the vessel wall). Fick's First Law (Equation 1) was used to calculate the relative perfusion with respect to a perpendicular distance away from the dorsal aorta.

$$J = -P\frac{dC}{dX} \quad (Equation\ 1)$$

The flux (J) was determined through a 1mm^2 area where individual contrast measurements were taken. The change in concentration (dC) with respect to the change in distance (dX) was determined based on the differences between the 8 hour

post injection image versus the 0 hour image with the initial concentration and distance taken from the dorsal aorta.

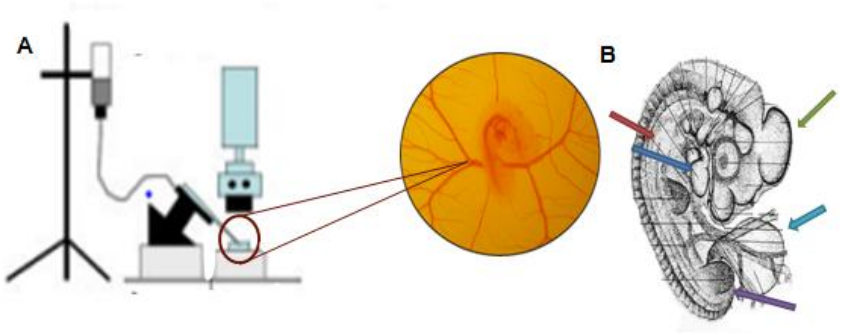

Figure 2.1 - Microinjection set up and identification of select organ analysis for nanoparticle contrast enhancement. (A) microinjection set up (Butcher et al., 2007) and (B) schematic of day 4 chick embryo and identification of organ contrast analysis with the following labels: blue = heart, red = dorsal aorta, green = head, purple = limb bud, teal = allantois

Statistics

One way and two way ANOVA and T-Test was used to compare contrast enhancement as described in the results. Heart rate and anatomical measurements were compared to EBSS controls via T-Test. Data are presented as a mean and standard deviation. $P<0.05$ denoted statistical significance.

2.4 Results

Differential attenuation with varying x-ray tube voltages and metallic nanoparticle contrast media

Material differences in nanoparticles can affect absorption of x-ray energy at different tube voltages, commonly understood in literature as the K-edge energy (Liu, Yu, Primak, & McCollough, 2009). Understanding x-ray attenuation of contrast media is crucial for not only establishing the most ideal scan protocols for 3D visualization of soft

tissues but is highly valuable for use in dual-energy CT based imaging technologies. Nanoparticle dilutions (20µL total volume) performed in triplicate for each particle type were scanned at three different x-ray tube voltages (80kV, 100kV, and 120kV) to assess the impact of voltage on the attenuation of metallic nanoparticles. Overall, the 110nm EXTN particles produced the highest levels of contrast enhancement with all three voltages assessed with no statistically significant differences in voltage (Figure 2.2). However, x-ray tube voltage was significant for some dilutions of the 1.9nm AuNP and 15nm AuNP particles (Figure 2.2). Specifically, higher concentrations became a

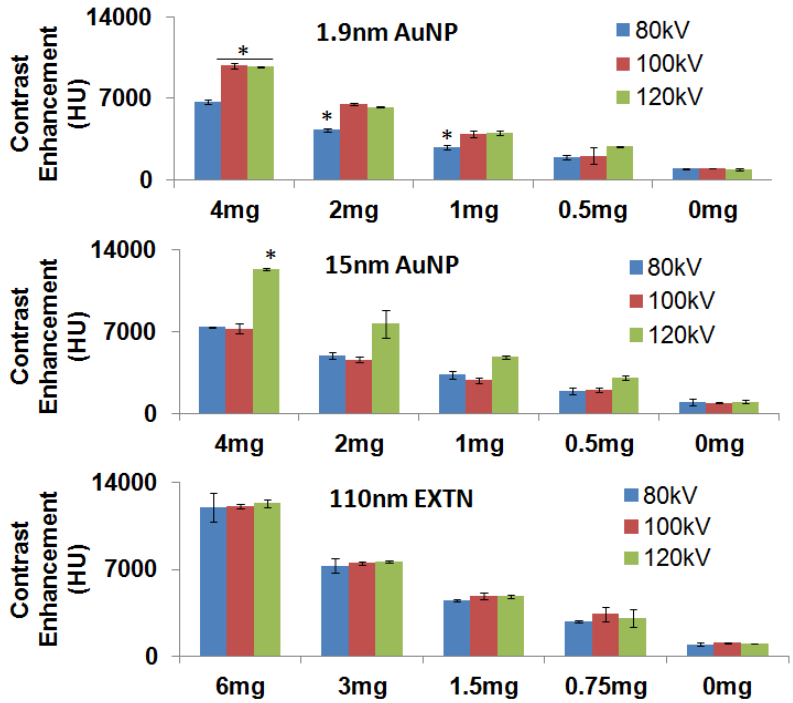

Figure 2.2 - Metallic nanoparticle comparison with varying scan voltages. 1.9nm AuNP (top), 15nm AuNP (middle), and 110nm EXTN (bottom) particle dilutions were analyzed scanned at different x-ray tube voltages while maintaining all other scan parameters as constants.

prominent factor for x-ray attenuation with significantly higher contrast enhancement with the 120kV and in some instances 100kV voltages as compared to 80kV (Figure 2.2). This effect diminished with dilutions less than 25%, a level higher than any microinjection volumes which would never exceed 20% total blood volume; therefore, it is doubtful that differences in x-ray tube voltage will drastically change the contrast enhancement outcome for soft tissue visualization in the context of live embryonic imaging presented here.

Temporal nanoparticle toxicity and x-ray attenuation during in vivo Micro-CT imaging

Acute and long-term toxicity from metallic nanoparticle exposure were assessed using heart rate and anatomical analysis, respectively. Embryonic heart rate was recorded immediately before (0-), immediately after (0+), 1 hour, and 24 hours post injection (Figure 2.3A). Exposure to the microinjection procedure caused a significant but transient drop in heart rate from baseline pre-injections levels in 15nm AuNPs from 143bpm to 104bpm, in 110nmEXTNs from 161bpm to 111bpm, and in EBSS from 147bpm to 109bpm in injected samples (Figure 2.3A). All heart rates recovered within 1 hour post injection with no significant difference between the 0- pre-injection levels for each respective injected media and between different types of media. This small transient dip is consistent with previous observations from nearly identical experimental procedures resulting in no long term, deleterious consequences to the samples (Henning et al 2011).

All samples injected with the 1.9nm AuNP particles died within 8 hours post injection. The concentration of metallic gold material in the 1.9nm AuNP is identical to the 15nm AuNP particles with the only difference being the size of particles themselves, indicating that toxicity is not only dose dependent but also size dependent of the particle (Pan et al., 2009). We next analyzed resulting embryonic morphology through anatomical measurements of day 10 embryos to see if particles induced malformations during development. No gross anatomical malformations were observed between samples

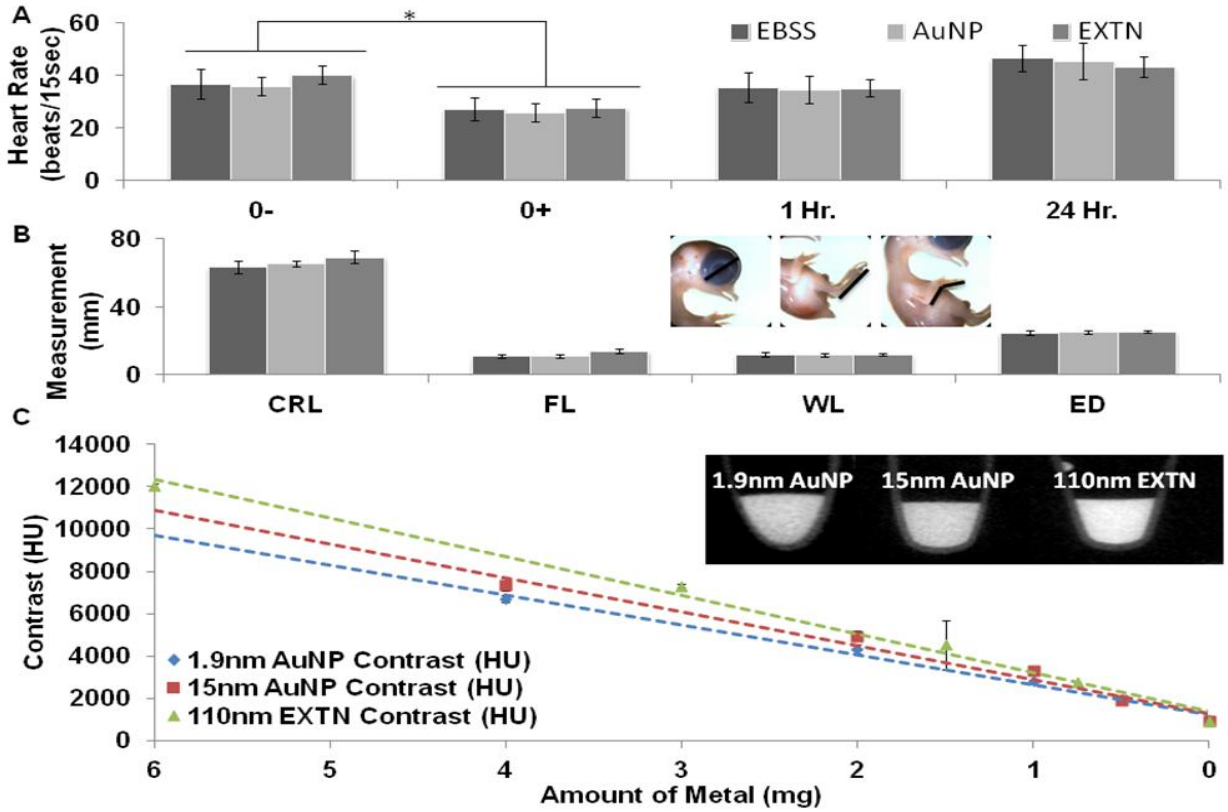

injected with particles as compared to EBSS control (Figure 2.1B). The WL, FL, ED,

Figure 2.3 - Nanoparticle Toxicity Analysis and Contrast Enhancement Calibration. (A) Acute heart rate analysis of day 3 chicks following treatment with metallic nanoparticle contrast media injected at 10% blood volume with EBSS serving as a negative control. (B) Body anatomical measurements of nanoparticle treated chicks as compared to controls. (C) Contrast enhancement vs. amount of metal dilution curve

and total CRL were consistent with no statistically significant differences between the samples injected with 15nm AuNPs or 110nm EXTNs as compared to measurements obtained from the EBSS controls suggesting that development proceeds normally in all nanoparticle exposed embryos. Subsequent scans on Day 10 embryos that were injected at Day 4 were inspected for gross internal organ malformations (e.g. heart, eye, brain, liver size/shape/positions), of which none were found. This was consistent with our previous contrast injection study (Henning et al., 2011).

As expected, we identified a linear reduction of x-ray attenuation with contrast dilution for all particle types considered (Figure 2.3C). The amount of metal was extrapolated from known metal concentrations in all particle stock solutions. The upper limit of contrast enhancement achieved for each particle type at a 10% injection volume is 1800HU, 1940HU, and 2500HU for the 1.9nm AuNP, 15nm AuNP, and 110nm EXTN respectively.

Comparison of local contrast enhancement between particle types

Comparison of spatial particle distribution demonstrates greater heterogeneity with the 110nm EXTN particles as compared to the smaller 1.9nm and 15nm AuNP particles. Structures associated with the vascular system, particularly the heart, dorsal aorta, and extra embryonic vasculature were visualized immediately post injection with representative images being taken within the first 30 minutes post injection (Figure 2.4B). Contrast enhancement was measured in the heart, dorsal aorta, head measured at the mesencephalon, limb, and allantoic sac immediately post injection (Figure 2.4A). The contrast enhancement produced by the 110nm EXTN particles was significantly

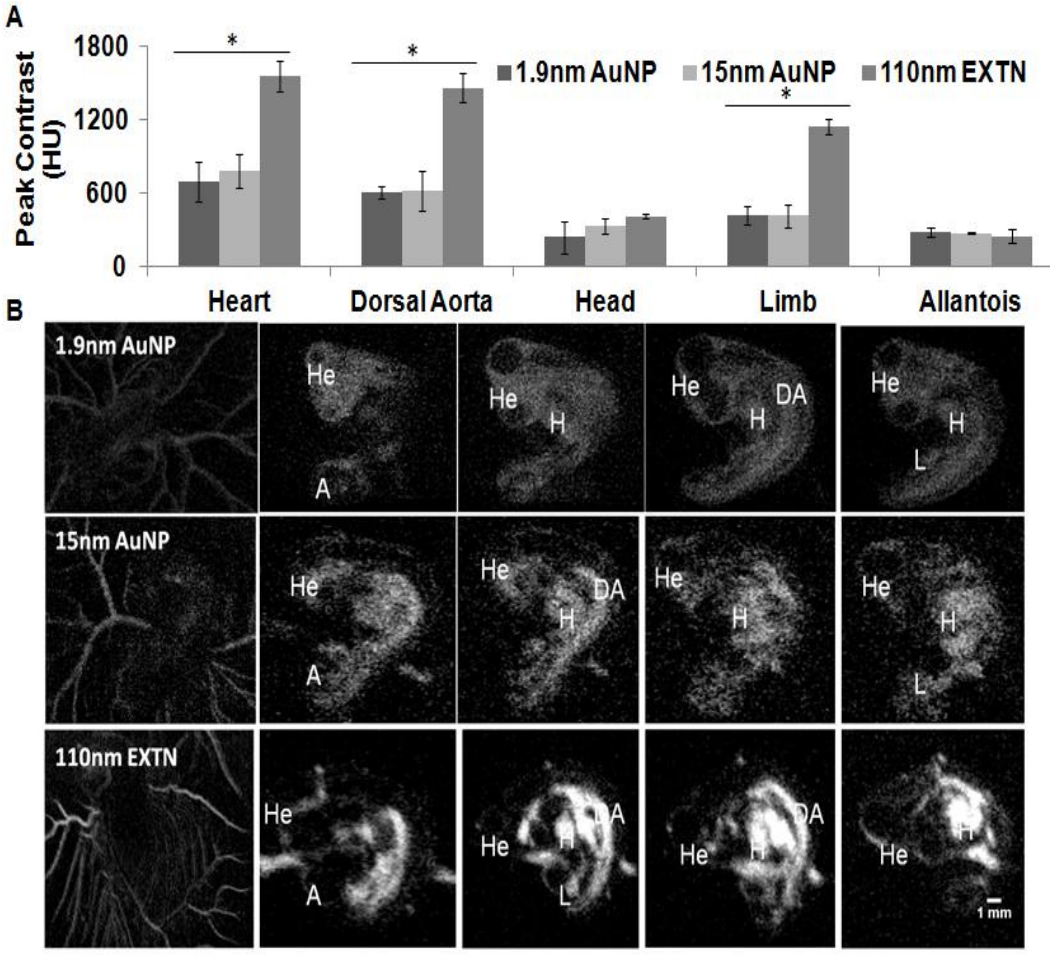

Figure 2.4 - Immediately post injection peak contrast. (A) Comparison of peak contrast enhancement between three different metallic nanoparticle contrast media microinjected into day 4 chick embryos at 10% blood volume. Contrast enhancement was measured within the heart, dorsal aorta, head, limb, and allantoic sac (n = 3). Contrast was significantly higher in embryos treated with 110nm EXTN particles ($P<0.05$) for the heart, dorsal aorta, and limb. (B) Representative 2D grayscale cross section images through the sagittal plane labeled with developing organ systems of day 4 chick embryos. 110nm EXTN particles demonstrate higher x-ray attenuation and soft tissue contrast enhancement as compared to the gold nanoparticles. Furthermore, a size dependent extravasation is suggested due to larger particles retained in the vasculature whereas the smallest 1.9nm AuNP particles have extravasated into the surrounding tissue. H = heart, He = head, DA = dorsal aorta, L = limb, and A = allantois

higher in the heart, dorsal aorta, and limb with levels as high as 1560HU immediately

post injection ($p<0.05$). Contrast enhancement was the same in the head and allantois between all particle types considered with no significant differences measured immediately post injection (Figure2. 4A). Visualization of sagittal image sections in representative embryos (Figure 2.4B) demonstrates qualitative spatial contrast enhancement differences within the same embryo and across particle types. The 1.9nm particles quickly extravasate from the vasculature and luminal spaces into the surrounding tissue, an observation not comparatively seen with the 110nm EXTN particles suggesting a size specific component to particle perfusion into the tissue.

Three dimensional renderings show maximum intensity and volumetric information of the embryo and surrounding extra embryonic vasculature (Figure 2.3). Maximum intensity projections (MIP) were generated and mapped to the same color intensity legend (Figure 2.5A) between all particle types allowing direct comparison of spatial contrast intensity revealing particle locations and their relative concentrations. The 1.9nm AuNP MIP rendering has homogenous particle distribution within the embryo with no clear concentrations throughout the volume suggesting fast extravasation and distribution of particles through the tissue (Figure 2.5A). 3D analysis of embryos injected with the 15nm AuNPs reveals minimal concentration of the particles within the heart and dorsal aorta that is most proximal to the heart indicated through the color map (Figure 2.3A). These results are also consistent with the measured contrast values (Figure 2.2A) with highest enhancement found in the cardiovascular system. The largest heterogeneity of spatial particle contrast enhancement is visualized with the 110nm EXTN particles (Figure 2.5A). High enhancement is observed in the heart,

dorsal aorta, and vitelliene vascular network denoted by the shift in the color map whereas the head and allantois have minimal particle concentration (Figure 3A, supplement video). Volumetric renderings reveal all density information of the embryo (Figure2. 3B). Subtleties of soft tissues around high vascularized tissues are revealed in more detail, particularly soft tissues surrounding the dorsal aorta and somites on the

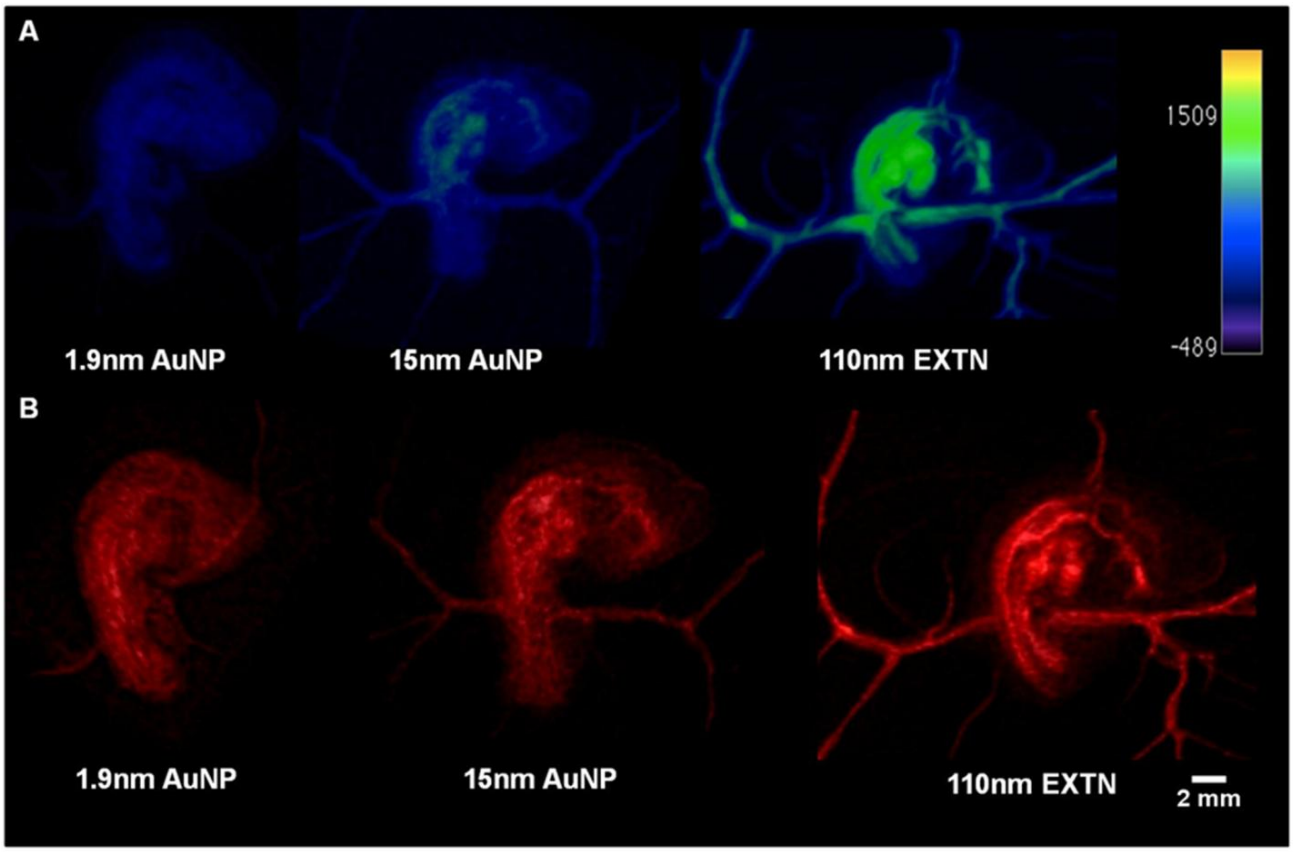

Figure 2.5 - 3D Comparison of Metallic Nanoparticles. Representative 3D renderings of day 4 chick embryos microinjected with different metallic nanoparticle contrast media and imaged at 50um resolution with 800 projection scans (A) Maximum intensity projections (MIP) of day 4 chicks calibrated to a single contrast enhancement color map given in the image denoting localized higher and lower contrast values measured in HU and (B) volumetric renderings of day 4 chicks injected with different contrast media.

dorsal side of the embryo (Figure 2.5B) best seen with the 110nm EXTN particles.

Temporally changing organ specific contrast enhancement

Contrast persistence and distribution was monitored for up to 24 hours post injection. The 1.9nm AuNP embryos did not survive to the 8-9 hour time point but the 15nm AuNP and 110nm EXTN embryos survived for 24 hours post injection for a total of three

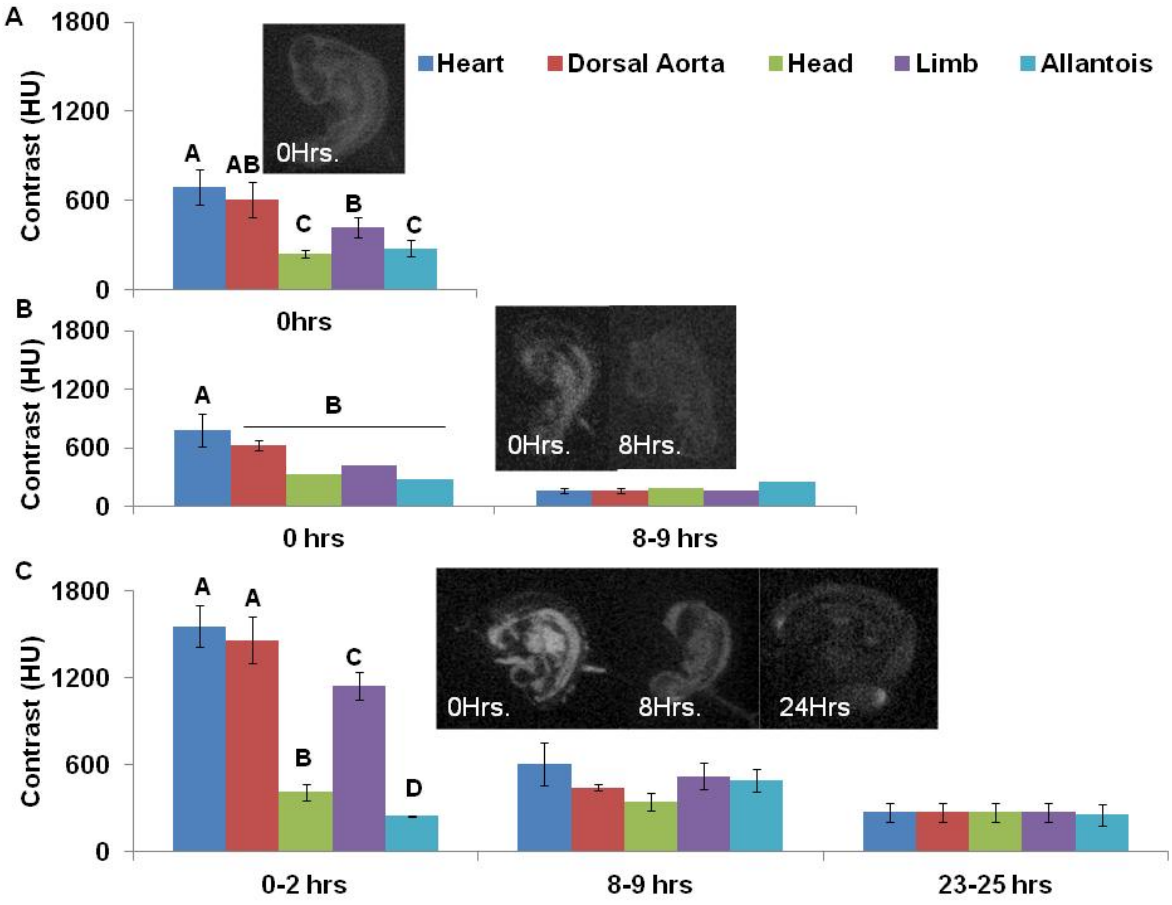

Figure 2.6 - Temporal contrast enhancement comparison (A) Contrast enhancement of the 1.9nm AuNP particles across multiple organ systems. Contrast extravasated quickly from the vasculature into the surround tissue and all samples died within 8 hours post injection. (B) Contrast enhancement of the 15nm AuNP particles over 8 hours post injection. Cardiovascular structures were visualized readily immediately post injection and by 8 hours contrast enhancement was the same across the embryo. Embryos survived for 24 hours post injection but contrast enhancement at 24 hours was not different from the background resulting in zero visualization of the embryo. (C) Contrast enhancement in day 4 embryos treated with 110nm EXTN particles produced the highest levels of contrast with strong attenuation in structures with high vascularity but enhancement across the embryo equalized by 8 hours post injection but tissue boundaries were still readily visualized. At

imaging time points. Heterogeneous spatial contrast enhancement was observed in all three particle types immediately post injection with the highest contrast enhancement associated with the cardiovascular system (Figure 2.6 A-C). Over a 24 hour period of time, contrast enhancement degraded in both 15nm AuNP and 110nm EXTN particles in the heart, dorsal aorta, limb, and head. At 8 hours post injection with the 15nm AuNPs, all organs considered were statistically the same with contrast levels ranging from 160HU – 250HU (Figure 2.6B). However, the 110nm EXTN particles at 8 hours post injection had statistically similar contrast enhancement in all organs but the overall contrast intensity was higher than that of the 15nm AuNPs with levels ranging from 350HU – 600HU (Figure 2.6C). At 24 hours post injection, contrast enhancement in the 15nm AuNP embryos was not distinguishable from background noise suggesting that the particles had extravasated out of the embryonic body into the extra embryonic space with homogenous distribution between the embryo and the albumin. At 24 hours post injection, contrast enhancement of 110nm EXTN embryos was nearly identical in all organs considered with an average value of 272 +/- 7 HU (Figure 2.4C). Specific tissue delineation in the 24 hour 110nm EXTN embryos was not readily visualized given the equal distribution of the particles within all tissues but the overall embryonic body was seen as compared to the background.

Comparison to previously published VP data (Henning et al., 2011) reveals that the 110nm EXTN particles outperform all other nanoparticle types and VP. The heart and dorsal aorta have significantly higher contrast enhancement in the 110nm EXTN embryos versus the VP embryos with values of 1557HU and 1462HU for 110nm EXTN

and 786HU and 945HU for VP in the heart and dorsal aorta respectively immediately post injection (Figure 2.7). Furthermore, analysis 24 hours later reveals persistence of the 110nm EXTN levels significantly higher than all organs considered except the allantois than the VP (Figure2. 7).

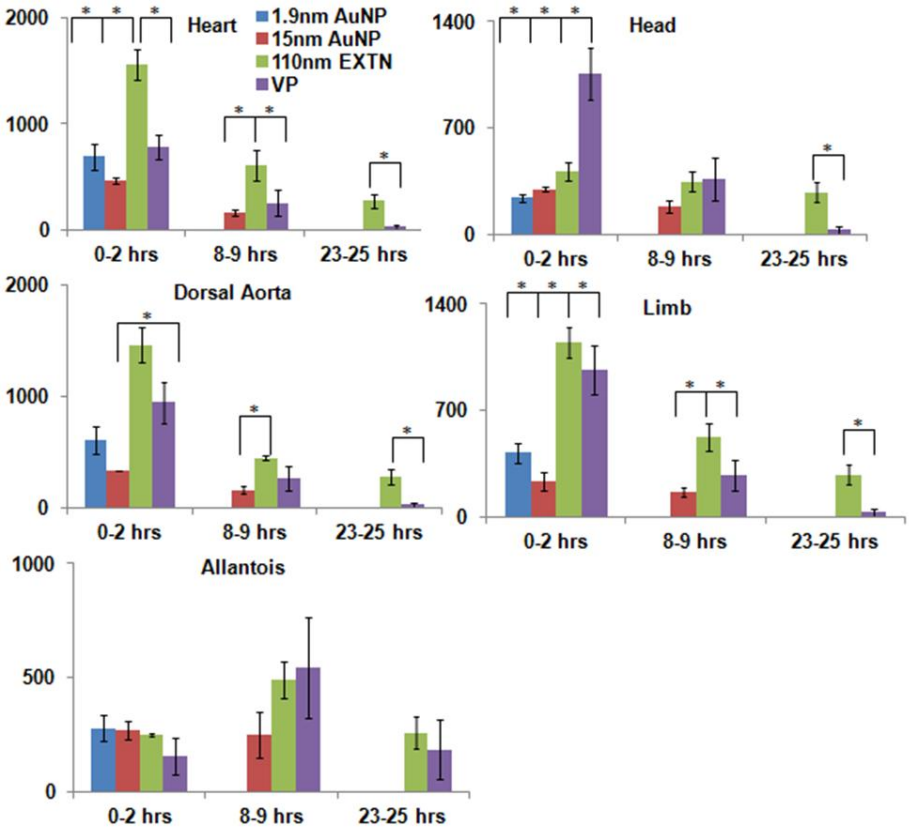

Figure 2.7 - Direct metallic nanoparticle comparison as compared to Visipaque. Contrast enhancement in each organ system considered for this study was compared across all three particles types presented against the previously published VP. The 110nm EXTN particles outperformed VP particularly in the cardiovascular structures, maintaining significantly high attenuation at 8 hours post injection in the hearts, dorsal aorta, and limb. At 24 hours post injection, the 110nm EXTN particles outperformed the VP demonstrating high levels of contrast enhancement in the embryonic body.

Modeled particle perfusion from the dorsal aorta into the surrounding tissue

Nanoparticles perfuse across the endothelium of the vasculature into the surrounding tissue of the embryonic body prior to perfusing into the remaining extra-embryonic space. Unique to the 110nm EXTN particles, perfusion of the particles from the vascular system into the surrounding tissue can be quantified within the first 8 hours post injection where tissue boundaries are still visualized, enabling quantification of particle movement rates out of major vascular structures. Contrast enhancement per amount of metal is known from the dilution data previously given (Figure 1C) and the stock solution of the EXTN particles is 300mg/mL of metal. We chose to quantify perfusion from the dorsal aorta into the flank mesenchyme. The perfusion coefficient versus distance (Figure 2.6A) increases exponentially with increasing distance from the dorsal aorta. A faster rate of perfusion farther from the dorsal aorta is correlative to lower contrast enhancement away from the dorsal aorta (Figure 2.8B). Measured perfusion rates ranged from 0.06um^2/s to 0.7um^2/s for distances ranging from 0.1mm – 0.3mm respectively. MIP 3D reconstructions reveal overall contrast enhancement based on a controlled color map (Figure 2.8B) at the two time points considered. Inset images, magnified to the same portion of the dorsal aorta, reveal changes in contrast enhancement over an 8 hour period. These images reveal a significant decrease in contrast enhancement within the dorsal aorta and decreasing contrast enhancement as distance increases away from the dorsal aorta indicating the increasing rate of perfusion with distance (Figure2. 8).

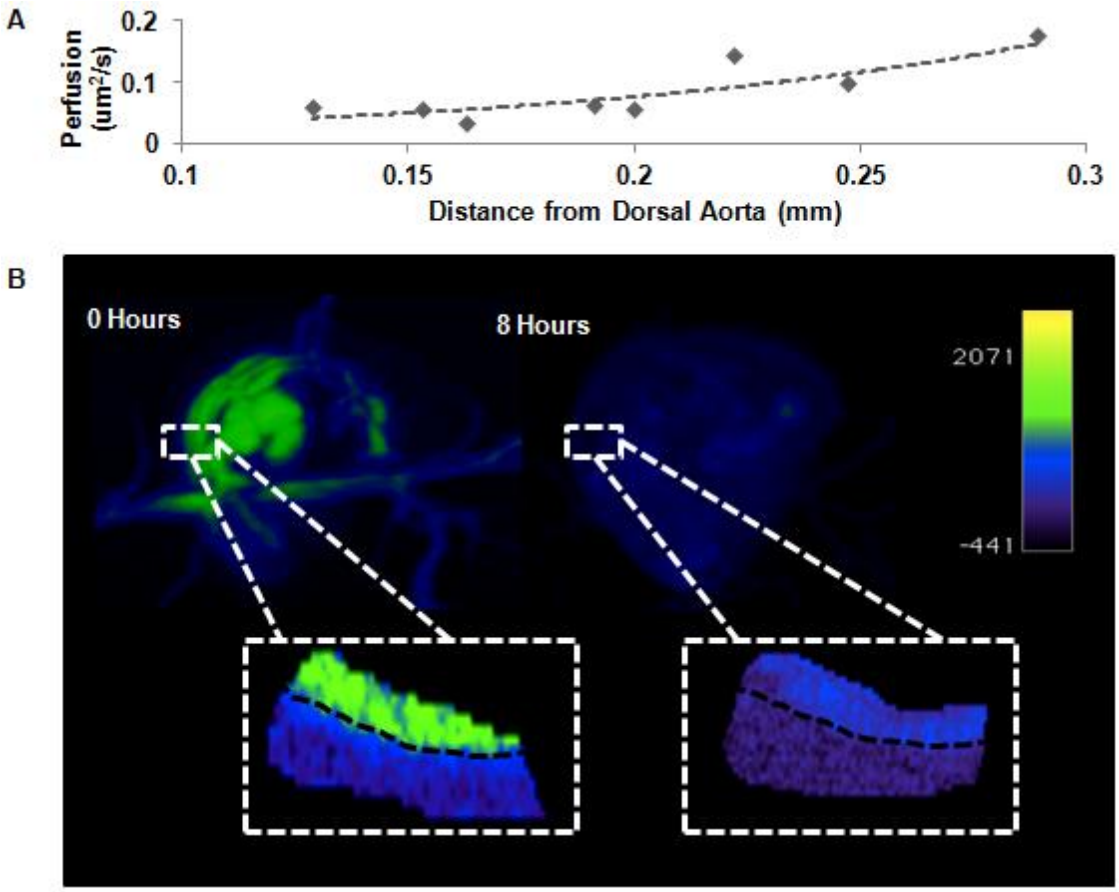

Figure 2.8 - Perfusion analysis of particles from the dorsal aorta into the flank mesenchyme. (A) Modeled particle diffusion over an 8 hour period of time from the dorsal aorta, sampled above the vitelliene vein. Contrast enhancement was measured at known distances away from the dorsal aorta at 8 hours post injection. Concentration and amount of metal values were derived from standard curves previously established (Figure 1). Fick's first law of diffusion was used to interpolate the diffusion coefficient as a function of distance from the dorsal aorta 8 hours post injection. (B) representative maximum intensity projections of immediately post injection (0 hours) and 8 hour post injection chick embryos with magnified insets of the dorsal aorta (black dashed line) and surrounding tissue. Color map based on contrast enhancement (HU) given in the legend.

2.5 Discussion

We demonstrate that nanoparticle based contrast enhancement is safe and effective for live in vivo microCT imaging of embryonic development. We show that the 110nm EXTN particles surpass the gold nanoparticles in contrast enhancement, residence time, and identifiable tissue boundaries. Furthermore, we show that contrast

enhancement of the embryo remains at high levels 24 hours post injection than the previously published VP. The best images of the cardiovascular structures was seen immediately post injection whereas the best analysis of the allantois is 8 hours post injection when contrast has reached its peak. Furthermore, our data suggests alternate clearance mechanisms than that observed with the VP studies, indicating extravasation of particles into the tissue where it further moves down a concentration gradient out of the embryonic body. Additionally, particles may also be transported into the cell via endocytosis, a mechanism that is out of the scope of this study but indicates future experimental opportunities. Given the increased time in reliable tissue boundary recognition, quantitative analysis into transport processes is possible. Here we present a method for characterizing relative perfusion coefficients from the dorsal aorta into the surrounding tissue demonstrating the ability for powerful insights into passive and active transport phenomena within live embryos.

MicroCT is a promising tool in 3D embryonic imaging for mid-late stage in vivo studies fulfilling the needed resolution and depth of field required for capturing these stages of development (Gregg & Butcher, 2012). Previous studies established the dose dependent toxicity of x-ray radiation on avian embryos (Henning et al., 2011) determining that a radiation dose of 798mGy would be required to induce morphological defects within the time period being considered, a level far above what is required for microCT imaging and what was presented in this study. The most pressing challenge associated with live imaging of embryos using microCT is the lack of available non-toxic, non-teratogenic contrast media. A number of exogenous soft tissue contrast

agents have been used in embryonic imaging (Butcher et al 2007) but nearly all contrast media has proven to be lethal. A detailed explanation of all contrast media, excluding the media used in this study, has been given in previous literature (Gregg et al., 2015). Prior to this study, the only non-toxic contrast media for live embryonic microCT imaging to our knowledge was VP (Henning et al., 2011) becoming the standard of comparison for live embryonic microCT imaging. In this study, the 110nm EXTN particles outperformed all other contrast media including VP. EXTN particles remained in the vasculature the longest with enhancement remaining up to 8 hours post injection. After 24 hours post injection, while vascular contrast was not distinguishable from the embryonic tissue, contrast enhancement remained within the embryonic body. Differences between nanoparticles in rates of extravasation and clearance from the embryo proper suggest a size dependent mechanism. For the metallic particles to extravasate into the surrounding embryonic tissue, they must cross the endothelium. The primitive vasculature is active and present throughout the time period of the presented study (days 4-5) but the blood vessels are immature in structure and function. Basic vascular architecture arises in the earliest stages of development prior to blood flow initiation (Sabin, 1917). Fusion and transformation of endothelial and angioblast progenitor cells into lamina produce the primitive vascular networks (vasculogenesis), from which sprouting and capillary formation occurs (angiogenesis). Primary blood vessels undergo much remodeling to eventually form the mature vascular system at the end of development (Risau & Flamme, 1995). A vast majority of vessels that arise throughout development regress, serving functions only for the development of a variety of different organ systems such as capillaries found in the prechondrogenic areas of the

embryo (Risau & Flamme, 1995). Continuous sprouting and regression of blood vessels results in an immature endothelium during much of development. Endothelial lamina and other structural component (organelles, junction components) are found in the chick embryo vessels by day 4 of development (Roy, Hirano, Kochen, & Zimmerman, 1974) but basement membrane structure is ill formed until day 18 of chick development and the tight junction complexes are “leaky” until the latest stages of development (Roy et al., 1974) indicating that extravasation of molecules, and in the case of this study, particles will readily occur across the endothelium.

Without a developed renal system, primitive filtering in embryos at the stages considered is in part attributed to the allantois. In early mid stage embryos (days 4-5), the allantois serves to store and excrete nitrogenous metabolites from the embryo (Bellairs & Osmond, 2014) with increasing ability of active transport across the allantoic epithelium (Graves, Dunn, & Brown, 1986). Henning et al found that VP was readily filtered into the allantoic sac. These observations are contrary to what was found in this study, suggesting a different mechanism for nanoparticle clearance from the embryonic body through either passive or active means. While contrast in the allantois was significantly less than other organ systems considered immediately post injection, the transient increase in enhancement can be due to many reasons namely slower transport and less permeable blood vessels into the allantois resulting in a time lag for contrast enhancement of the allantois. The glomeruli of the renal system are not perfused and integrated into systemic vasculature until much later in development, with the earliest stages of glomerular perfusion beginning on day 10 of development and

continuing until near hatching at day 18 (Bolin & Burggren, 2013). For this reason, rudimentary clearance mechanisms are largely mitigated through the allantois and the chorioallantoic membrane. As previously mentioned, the allantois has limited observable role with clearance of the nanoparticles. Qualitatively, nanoparticle clearance occurred through movement down concentration gradients passively and actively with transport through the embryo proper and then into the extra-embryonic membranes.

The use of nanoparticle based soft tissue contrast presents the questions of particle toxicity and stipulations for the use in live embryonic systems. Previous studies and literature reviews outline the known toxicity of gold nanoparticles with several metrics including MTT assays for metabolic disruption, apoptosis, and oxidative stress (Aillon, Xie, El-Gendy, Berkland, & Forrest, 2009; Jia et al., 2009; Pan et al., 2009). Some of the most influential attributes of nanoparticles that result in toxic effects to cell populations include particle size, dose, and surface charge. Pan et al found that smaller particles (<2nm) exhibit mitochondrial damage, necrosis, and oxidative stress whereas 15nm gold particles did not (Pan et al., 2009). Additionally, particles less than a couple of nanometers in diameter have shown to have chemical reactivity that is not observed with larger sized particles (Turner et al., 2008). Goodman and colleagues indicated that cationic particles display toxic effects suspected of malignant interactions with the negatively charged cellular membrane whereas the anionic counterpart to these particles were non-toxic (Goodman, McCusker, Yilmaz, & Rotello, 2004). We have found that approximately 10% blood volume bolus injections with material

concentrations as high as 300mg/mL to be non-toxic. Preliminarily, we have observed that volume injections approaching or exceeding 20% blood volume result in a non-recoverable decrease in heart rate

The data presented here captures static live imaging at a single stage of development, future studies and the development of new technology could address such questions as the biodistribution and residence time of particles in older stage embryos (days 4-10) with changing tissue architecture and material properties affecting the behavior of the particles. Extension of the 110nm EXTN particles into later stage embryos will elucidate changes in material properties and extracellular environments. Differential particle movements within the tissue and changes in clearance patterns – indicative of renal system development – will give critical insights into key morphogenetic events occurring simultaneously through the entire embryo. Furthermore, avian embryos develop in a similar manner as mammals capable of developing relevant congenital malformations through surgical manipulation or genetic perturbation (Hogers, DeRuiter, Gittenberger-de Groot, & Poelmann, 1999). Parsing out tissue contributions and changes in morphogenesis within live, diseased embryos with clinically relevant defects is paramount for quantitative 3D analysis of dysregulation during abnormal development. With the development of novel and adaptation of current technologies for mid-late stage live in vivo microCT imaging of embryonic development, our understandings and capabilities of studying this elusive stage of morphogenesis will be realized. Coupling high resolution 3D imaging technologies with long term tissue contrast will profoundly increase our current understanding of fundamental morphogenetic analysis.

References

Aillon, K. L., Xie, Y., El-Gendy, N., Berkland, C. J., & Forrest, M. L. (2009). Effects of nanomaterial physicochemical properties on in vivo toxicity. *Advanced Drug Delivery Reviews*, *61*(6), 457–466. http://doi.org/10.1016/j.addr.2009.03.010

Ashton, J. R., Clark, D. P., Moding, E. J., Ghaghada, K., Kirsch, D. G., West, J. L., & Badea, C. T. (2014). Dual-energy micro-CT functional imaging of primary lung cancer in mice using gold and iodine nanoparticle contrast agents: a validation study. *PloS One*, *9*(2), e88129. http://doi.org/10.1371/journal.pone.0088129

Bellairs, R., & Osmond, M. (2014). *Atlas of Chick Development*. *Atlas of Chick Development*. http://doi.org/10.1016/B978-0-12-384951-9.00013-7

Bolin, G., & Burggren, W. W. (2013). Metanephric kidney development in the chicken embryo: Glomerular numbers, characteristics and perfusion. *Comparative Biochemistry and Physiology - A Molecular and Integrative Physiology*, *166*(2), 343–350. http://doi.org/10.1016/j.cbpa.2013.07.011

Boll, H., Nittka, S., Doyon, F., Neumaier, M., Marx, A., Kramer, M., … Brockmann, M. a. (2011). Micro-CT based experimental liver imaging using a nanoparticulate contrast agent: a longitudinal study in mice. *PloS One*, *6*(9), e25692. http://doi.org/10.1371/journal.pone.0025692

Butcher, J. T., Sedmera, D., Guldberg, R. E., & Markwald, R. R. (2007). Quantitative volumetric analysis of cardiac morphogenesis assessed through micro-computed tomography. *Developmental Dynamics : An Official Publication of the American Association of Anatomists*, *236*(3), 802–9. http://doi.org/10.1002/dvdy.20962

Cui, C., Filla, M. B., Jones, E. a V, Lansford, R., Cheuvront, T., Al-Roubaie, S., … Little,

C. D. (2013). Embryogenesis of the first circulating endothelial cells. *PloS One*, *8*(5), e60841. http://doi.org/10.1371/journal.pone.0060841

Czirók, A., Rongish, B. J., & Little, C. D. (2004). Extracellular matrix dynamics during vertebrate axis formation. *Developmental Biology*, *268*(1), 111–22. http://doi.org/10.1016/j.ydbio.2003.09.040

Degenhardt, K., Wright, A. C., Horng, D., Padmanabhan, A., & Epstein, J. a. (2010). Rapid 3D phenotyping of cardiovascular development in mouse embryos by micro-CT with iodine staining. *Circulation. Cardiovascular Imaging*, *3*(3), 314–22. http://doi.org/10.1161/CIRCIMAGING.109.918482

Diaspro, A., Chirico, G., & Collini, M. (2005). Two-photon fluorescence excitation and related techniques in biological microscopy. *Quarterly Reviews of Biophysics*, *38*(2), 97–166. http://doi.org/10.1017/S0033583505004129

Dickinson, M. E., Simbuerger, E., Zimmermann, B., Waters, C. W., & Fraser, S. E. (2003). Multiphoton excitation spectra in biological samples. *Journal of Biomedical Optics*, *8*(3), 329–38. http://doi.org/10.1117/1.1583734

Goodman, C. M., McCusker, C. D., Yilmaz, T., & Rotello, V. M. (2004). Toxicity of gold nanoparticles functionalized with cationic and anionic side chains. *Bioconjugate Chemistry*, *15*(4), 897–900. http://doi.org/10.1021/bc049951i

Graves, J. S., Dunn, B. E., & Brown, S. C. (1986). Embryonic chick allantois: functional isolation and development of sodium transport. *The American Journal of Physiology*, *251*(5 Pt 1), C787–94. Retrieved from http://ajpcell.physiology.org/content/251/5/C787.abstract

Gregg, C. L., & Butcher, J. T. (2012). Quantitative In Vivo Imaging of Embryonic

Development: Opportunities and Challenges. *Differentiation*, *84*(1), 149–162. http://doi.org/10.1016/j.diff.2012.05.003.Quantitative

Gregg, C. L., & Butcher, J. T. (2013). Translational paradigms in scientific and clinical imaging of cardiac development. *Birth Defects Research. Part C, Embryo Today : Reviews*, *99*(2), 106–20. http://doi.org/10.1002/bdrc.21034

Gregg, C. L., Recknagel, A. K., & Butcher, J. T. (2015). Micro/Nano-Computed Tomography Technology for Quantitative Dynamic, Multi-scale Imaging of Morphogenesis. *Methods in Molecular Biology (Clifton, N.J.)*, *1189*, 47–61. http://doi.org/10.1007/978-1-4939-1164-6

Henning, A. L., Jiang, M. X., Yalcin, H. C., & Butcher, J. T. (2011). Quantitative three-dimensional imaging of live avian embryonic morphogenesis via micro-computed tomography. *Developmental Dynamics : An Official Publication of the American Association of Anatomists*, *240*(8), 1949–57. http://doi.org/10.1002/dvdy.22694

Hogers, B., DeRuiter, M. C., Gittenberger-de Groot, a C., & Poelmann, R. E. (1999). Extraembryonic venous obstructions lead to cardiovascular malformations and can be embryolethal. *Cardiovascular Research*, *41*(1), 87–99. Retrieved from http://www.ncbi.nlm.nih.gov/pubmed/10325956

Jia, H. Y., Liu, Y., Zhang, X. J., Han, L., Du, L. B., Tian, Q., & Xu, Y. C. (2009). Potential oxidative stress of gold nanoparticles by induced-NO releasing in serum. *Journal of the American Chemical Society*, *131*(1), 40–41. http://doi.org/10.1021/ja808033w

Johnson, J. T., Hansen, M. S., Wu, I., Healy, L. J., Johnson, C. R., Jones, G. M., … Keller, C. (2006). Virtual histology of transgenic mouse embryos for high-throughput phenotyping. *PLoS Genetics*, *2*(4), e61.

http://doi.org/10.1371/journal.pgen.0020061

Kim, J. S., Min, J., Recknagel, A. K., Riccio, M., & Butcher, J. T. (2011). Quantitative Three-Dimensional Analysis of Embryonic Chick Morphogenesis Via Microcomputed Tomography. *The Anatomical Record: Advances in Integrative Anatomy and Evolutionary Biology*, *294*(1), 1–10. http://doi.org/10.1002/ar.21276

Lee, C.-L., Min, H., Befera, N., Clark, D., Qi, Y., Das, S., … Kirsch, D. G. (2014). Assessing Cardiac Injury in Mice wit hDual Energy-microCT, 4D-microCT and microSPECT Imaging Following Partial-Heart Irradiation. *Int. J Radiat Oncol Biol Phys*, *88*(3), 686–693. http://doi.org/10.1016/j.ijrobp.2013.11.238.Assessing

Liu, X., Yu, L., Primak, A. N., & McCollough, C. H. (2009). Quantitative imaging of element composition and mass fraction using dual-energy CT: three-material decomposition. *Medical Physics*, *36*(5), 1602–1609. http://doi.org/10.1118/1.3097632

Melancon, M. P., Zhou, M., Zhang, R., Xiong, C., Allen, P., Wen, X., … Li, C. (2014). Selective uptake and imaging of aptamer- and antibody-conjugated hollow nanospheres targeted to epidermal growth factor receptors overexpressed in head and neck cancer. *ACS Nano*, *8*(5), 4530–8. http://doi.org/10.1021/nn406632u

Metscher, B. D. (2009). MicroCT for developmental biology: a versatile tool for high-contrast 3D imaging at histological resolutions. *Developmental Dynamics : An Official Publication of the American Association of Anatomists*, *238*(3), 632–40. http://doi.org/10.1002/dvdy.21857

Metscher, B. D., & Müller, G. B. (2011). MicroCT for molecular imaging: quantitative visualization of complete three-dimensional distributions of gene products in

embryonic limbs. *Developmental Dynamics : An Official Publication of the American Association of Anatomists*, *240*(10), 2301–8. http://doi.org/10.1002/dvdy.22733

Nakamura, H., & Funahashi, J. (2001). Introduction of DNA into chick embryos by in ovo electroporation. *Methods (San Diego, Calif.)*, *24*(1), 43–8. http://doi.org/10.1006/meth.2001.1155

Nebuloni, L., Kuhn, G. a, & Müller, R. (2013). A comparative analysis of water-soluble and blood-pool contrast agents for in vivo vascular imaging with micro-CT. *Academic Radiology*, *20*(10), 1247–55. http://doi.org/10.1016/j.acra.2013.06.003

Pan, Y., Leifert, A., Ruau, D., Neuss, S., Bornemann, J., Schmid, G., … Jahnen-Dechent, W. (2009). Gold Nanoparticles of Diameter 1.4 nm Trigger Necrosis by Oxidative Stress and Mitochondrial Damage. *Small*, *5*(18), 2067–2076. http://doi.org/10.1002/smll.200900466

Risau, W., & Flamme, I. (1995). V asculogenesis. *Annu. Rev. Cell Dev. Biol.*, *11*, 73–91.

Roger, V. L., Go, A. S., Lloyd-Jones, D. M., Adams, R. J., Berry, J. D., Brown, T. M., … Wylie-Rosett, J. (2010). Heart Disease and Stroke Statistics--2011 Update: A Report From the American Heart Association. *Circulation*, 1–193. http://doi.org/10.1161/CIR.0b013e3182009701

Roy, S., Hirano, A., Kochen, J. A., & Zimmerman, H. M. (1974). The fine structure of cerebral blood vessels in chick embryo. *Acta Neuropathologica*, *30*(4), 277–285.

Sabin, F. (1917). Origin and Development of the Primitive Vessels of the Chick and of the Pig. *Carnegie Institution of Washington*, *6*(226), 64.

Scheller, B., Hennen, B., Thünenkötter, T., Mrowietz, C., Markwirth, T., Schieffer, H., & Jung, F. (1999). Effect of X-ray contrast media on blood flow properties after

coronary angiography. *Thrombosis Research*, *96*(4), 253–60. Retrieved from http://www.ncbi.nlm.nih.gov/pubmed/10593427

Shen, Y., Leatherbury, L., Rosenthal, J., Yu, Q., Pappas, M. a, Wessels, a, … Lo, C. W. (2005). Cardiovascular phenotyping of fetal mice by noninvasive high-frequency ultrasound facilitates recovery of ENU-induced mutations causing congenital cardiac and extracardiac defects. *Physiological Genomics*, *24*(1), 23–36. http://doi.org/10.1152/physiolgenomics.00129.2005

Squirrell, J. M., Wokosin, D. L., White, J. G., & Bavister, B. D. (1999). Long-term two-photon fluorescence imaging of mammalian embryos without compromising viability. *Nature Biotechnology*, *17*(8), 763–7. http://doi.org/10.1038/11698

Supatto, W., Débarre, D., Moulia, B., Brouzés, E., Martin, J.-L., Farge, E., & Beaurepaire, E. (2005). In vivo modulation of morphogenetic movements in Drosophila embryos with femtosecond laser pulses. *Proceedings of the National Academy of Sciences of the United States of America*, *102*(4), 1047–52. http://doi.org/10.1073/pnas.0405316102

Supatto, W., Mcmahon, A., Fraser, S. E., & Stathopoulos, A. (2009). Quantitative imaging of collective cell migration during Drosophila gastrulation: multiphoton microscopy and computational analysis, *4*(10), 1397–1412. http://doi.org/10.1038/nprot.2009.130.Quantitative

Turner, M., Golovko, V. B., Vaughan, O. P. H., Abdulkin, P., Berenguer-Murcia, A., Tikhov, M. S., … Lambert, R. M. (2008). Selective oxidation with dioxygen by gold nanoparticle catalysts derived from 55-atom clusters. *Nature*, *454*(7207), 981–983. http://doi.org/10.1038/nature07194

Wen, X., Wu, Q. P., Lu, Y., Fan, Z., Charnsangavej, C., Wallace, S., … Li, C. (2001). Poly(ethylene glycol)-conjugated anti-EGF receptor antibody C225 with radiometal chelator attached to the termini of polymer chains. *Bioconjugate Chemistry*, *12*(4), 545–53. Retrieved from http://www.ncbi.nlm.nih.gov/pubmed/11459459

Wessels, A., & Sedmera, D. (2003). Developmental anatomy of the heart: a tale of mice and man. *Physiological Genomics*, *15*(3), 165–76. http://doi.org/10.1152/physiolgenomics.00033.2003

Yalcin, H. C., Shekhar, A., McQuinn, T. C., & Butcher, J. T. (2011). Hemodynamic patterning of the avian atrioventricular valve. *Developmental Dynamics : An Official Publication of the American Association of Anatomists*, *240*(1), 23–35. http://doi.org/10.1002/dvdy.22512

Yu, B., Mao, Y., Bai, L., Herman, S. E. M., Wang, X., Ramanunni, A., … Muthusamy, N. (2015). Targeted nanoparticle delivery overcomes off-target immunostimulatory effects of oligonucleotides and improves therapeutic efficacy in chronic lymphocytic leukemia, *121*(1), 136–148. http://doi.org/10.1182/blood-2012-01-407742.

Yu, Q., Shen, Y., Chatterjee, B., Siegfried, B. H., Leatherbury, L., Rosenthal, J., … Lo, C. W. (2004). ENU induced mutations causing congenital cardiovascular anomalies. *Development (Cambridge, England)*, *131*(24), 6211–23. http://doi.org/10.1242/dev.01543

Zamir, E. a, Czirók, A., Cui, C., Little, C. D., & Rongish, B. J. (2006). Mesodermal cell displacements during avian gastrulation are due to both individual cell-autonomous and convective tissue movements. *Proceedings of the National Academy of Sciences of the United States of America*, *103*(52), 19806–11.

http://doi.org/10.1073/pnas.0606100103

Zarschler, K., Prapainop, K., Mahon, E., Rocks, L., Bramini, M., Kelly, P. M., … Dawson, K. a. (2014). Diagnostic nanoparticle targeting of the EGF-receptor in complex biological conditions using single-domain antibodies. *Nanoscale*, *6*(11), 6046–56. http://doi.org/10.1039/c4nr00595c

CHAPTER 3

LONGITUDINAL, QUANTITATIVE IN VIVO THREE DIMENSIONAL ANALYSIS OF LIVE AVIAN MORPHOGENESIS WITH HIGH RESOLUTION MICRO-COMPUTED TOMOGRAPHY IMAGING DURING MID-LATE STAGES OF DEVELOPMENT

3.1 Abstract

Clinically relevant congenital malformations arise and manifest during mid-late stages of development that are inaccessible for live embryonic imaging through traditional optical means. MicroCT imaging coupled with nanoparticle based exogenous soft tissue contrast provides a rapid and inexpensive 3D imaging technology with the high spatial and temporal resolutions required to capture this elusive stage in live samples. Here we establish longitudinal quantification of live embryonic development with characterization of biodistribution and persistence of nanoparticle contrast media spatially and temporally in chick embryos ranging from days 4-11 of development. We demonstrate the use of live microCT imaging for the capacity of high resolution virtual histology and identification of tissue boundaries comparable to that of standard histological sectioning and that non-boundary regions produce higher signal intensities than that of their histological counterparts. Furthermore, we establish that particle biodistribution is spatially unique with high contrast enhancement in the vascular structures but within 24 hours post injection of contrast media, extravasation and sequestration of contrast media is heterogeneous demonstrating particles sequestered in certain organs systems

over others and enhancement of the surround connective mesenchyme within the embryo proper. We identified that contrast perfusion from the blood into the tissue was also heterogeneous within a single organ, where we specifically focused on bulk particle perfusion into the left and right myocardium. We identified side specific and age specific perfusion metrics for rates of perfusion fit to a piece-wise Gaussian distribution. The modeled curves shift with embryonic age and with the left myocardium reflecting an increase in peak bulk perfusion rate location reflecting an overall slower rate of perfusion into the myocardium suggesting a sequestering of particles into the myocardium. Collectively we quantified longitudinal, live embryonic morphogenesis in three dimensional during the mid-late stages of development demonstrating high resolution of morphology and changing morphodynamics that occur with embryonic age with spatial and temporal heterogeneity.

3.2 Introduction

Embryonic development is a rapid and dynamic three-dimensional process characterized by the growth and differentiation of immature cell populations into a complex organizational network of tissues. Dysregulation of morphogenetic processes can result in a congenital malformation. Approximately 3% of all live births result in a congenital defect accounting for 2.6 billion dollars in medical care annually and a 20% infant mortality rate (Gregg & Butcher, 2013). In most instances, genetic evidence is insufficient to explain the prevalence and variety of malformations observed clinically. Altering early stage morphogenetic patterning is nearly always lethal but clinically survivable malformations arise and manifest during the mid-late stages of development

when tissue differentiation and maturation have already begun (Roger et al., 2010). A vast majority of live embryonic studies have focused on the initiating events of development spanning gastrulation and heart tube formation with the onset of beating (Cui et al., 2013; Czirók, Rongish, & Little, 2004; Zamir, Czirók, Cui, Little, & Rongish, 2006). In contrast, live embryonic studies conducted during mid-late stages of development are far more limited, requiring a reliable animal model and high resolution, deep tissue imaging. Confocal and multiphoton microscopy has been standards in quantitative and qualitative live embryonic analysis with an array of excitable flurophores and imaging depths capable to 2mm (Diaspro, Chirico, & Collini, 2005; Dickinson, Simbuerger, Zimmermann, Waters, & Fraser, 2003; Squirrell, Wokosin, White, & Bavister, 1999; Supatto et al., 2005; Supatto, Mcmahon, Fraser, & Stathopoulos, 2009). Beyond the earliest stages of development, embryonic tissue is dense and light scattering rendering optical techniques ineffective for analysis of live samples. Ultrasound imaging has been a useful tool for screening hemodynamic profiles of developing embryos coupling nicely for computational analysis of fluid-solid tissue interactions (Shen et al., 2005; Wessels & Sedmera, 2003; B. Yu et al., 2015; Q. Yu et al., 2004). Unfortunately, ultrasound imaging is inherently two dimensional (2D), suffers from poor signal to noise ratio, and differential tissue contrast (Metscher, 2009). For live three dimensional (3D) whole specimen imaging during mid-late stages, magnetic resonance imaging (MRI) and micro-computed tomography (microCT) are the current options available. Whole specimen MRI studies are emerging as rf coil designs improve for analysis of the given animal model and more sophisticated post-processing techniques. MRI is expensive with scan times exceeding $400/hour and acquisition

time spanning several hours leading to additional considerations for environmental control to maintain healthy, viable samples (Gregg & Butcher, 2012).

MicroCT has been a valuable imaging tool for characterizing tortuous anatomy with high spatial and temporal resolutions (Hogers, DeRuiter, Gittenberger-de Groot, & Poelmann, 1999). Exogenous soft tissue contrast is critical for producing high quality images for discerning relevant quantitative information. Contrast agents are typically comprised of high atomic weight molecules nearly all of which are toxic. Henning et al first quantified development with live in vivo microCT imaging (Henning, Jiang, Yalcin, & Butcher, 2011) establishing the safety of microCT imaging on embryos and the lethality of exogenous soft tissue contrast yielding a single non-toxic contrast agent available, the iodinated molecule iodixanol (Henning et al., 2011). Dose dependent biodistribution kinetics and volumetric analysis using iodixanol in live avian embryos has recently been done (Henning et al., 2011). Organ specific analysis of contrast distribution is critical for establishing anatomical changes during mid-late stages of development. Long term in vivo microCT imaging of soft tissues is prohibited by rapid clearance and/or scavenging of free molecule exogenous contrast media. Nanoparticles have demonstrated long residence times and high levels of x-ray attenuation becoming a promising option for embryonic imaging contrast (Ashton et al., 2014; Boll et al., 2011; Lee et al., 2014; Nebuloni, Kuhn, & Müller, 2013). Nanoparticles can be fabricated out of multiple materials (gold, earth metals, tungsten, liposomes encapsulating iodixanol, ect.) and have been a prominent part of cancer research as an imaging and delivery tool (Melancon et al., 2014; Zarschler et al., 2014). Biomolecule conjugation to the nanoparticle surface can result in molecular targeting experiments for different tissue

types (Melancon et al., 2014; Wen et al., 2001). Recently we published the first to our knowledge study on the extension of nanoparticle based exogenous soft tissue contrast to live in vivo microCT imaging (Gregg et al in review). We demonstrated that alkaline earth 110nm metallic nanoparticles are highly radiopaque and persist for a minimum of 24 hours post injection in day 4 embryos as compared to their 15nm and 1.9nm gold nanoparticle counterparts yielding high tissue boundary delineation with time dependent and organ dependent contrast enhancement. Quantification of relative perfusion of the 110nm alkaline earth metal particles moving out of the dorsal aorta into the surrounding dorsal mesenchyme revealed an exponential increase in perfusion coefficient compared to perpendicular distance from the dorsal aorta over an 8 hour time period post injection (Gregg et al in review 2016).

In this study, we extended the use of the 110nm alkaline earth metal particles into day 4, 7, and 10 chick embryos for longitudinal analysis of particle biodistribution and persistence over 24 hours at multiple stages of development. We found that sample age correlates to increased particle persistence along with spatial and temporal heterogeneous particle distribution that is unique at each embryonic age. Furthermore, we establish virtual histological analysis of mid-late stage embryos as compared to standard histological sections, revealing sequestered particle distribution and gross morphological changes of tissue assembly. We modeled organ growth metrics spanning days 4-11 of chick development revealing organ specific changes in the heart, left and right lung, and eyes. Lastly, we extend methods previously discussed (Chapter 2) related to nanoparticle perfusion into the tissue to quantify bulk particle transport into

the left and right myocardium and concentration of nanoparticles versus distance into the myocardium through semi-automated interpretation of line scan contrast enhancement measurements. Concentration and bulk transport metrics reveals spatial and age related heterogeneity emerging patterns reflective of morphogenetic divergence in the tissue properties.

3.3 Experimental Procedures

Preparation of embryonic samples and in vivo microinjections

White leghorn eggs (Cornell Poultry) were accessed through an in ovo culture (Nakamura & Funahashi, 2001) after three days of incubation at 99.5˚F and 55% humidity. For culturing, the external egg shell was cleaned with 70% ethanol. Using dissection scissors, a small opening was made at the non-blunt end of the egg and 6-7mL of albumen was removed with a sterile syringe and 21 gauge needle. The opening was secured with masking tape and two strips of masking tape were placed lengthwise down the egg. A small window was cut in the egg shell with dissection scissors, giving access and visualization to the embryo. For the remaining experimental time, embryos were housed in Styrofoam incubators with temperature and humidity maintenance.

Borosillicate glass capillary tubes (OD 1.0mm, ID 0.75mm) were drawn and beveled at 45˚ forming microneedles with 20μm diameters. A micromanipulator, silicon tubing, syringe, and microneedles were used for a gravity driven pressure gradient to inject chick embryos on days 4, 7,and 10. Soft tissues were visualized with a dissecting light microscope and 110nm alkaline earth metal particles (110nm EXTN, Miltenyi Biotec)

were injected into the extraembryonic vasculature at 10uL, 55uL, and 140uL volumes for days 4, 7, and 10 respectively.

Skeletal muscle paralysis agent toxicity based on heart rate and morphology

Tubocurarine hydrochloride efficacy and toxicity was determined from day 6 to day 10 of development for temporary skeletal muscle paralysis. Tubocurarine hydrochloride was administered in a 100uL volume onto the chorioallantoic membrane (CAM) in 0.5mg, 1mg, and 2mg dosages dissolved in Tyrodes's salt solution (Sigma Aldrich, pH = 7.4) with Tyrode's salt solution without Tb serving as the negative control. Heart rate measurements were taken in 15 second intervals approximately every ten minutes with a starting heart rate measurement prior to treatment at t=0. Any visualized contraction, either limb or whole body, was considered an instance of skeletal muscle movement. The samples were monitored until skeletal muscle movements returned. Chick samples were treated daily from day 6 to day 10 of development and sacrificed on day 12 of development. The crown-rump length (CRL), dorsal-ventral length (DVL), wing length (WL), and eye diameter (ED) were measured in ImageJ (National Institutes of Health). Any significant decline in anatomical measurement from negative control values was determined to be toxic.

In vivo microCT scanning

Embryos were placed in a custom built polycarbonate imaging chamber and scanned on a GE Healthcare eXplore CT 120 machine at 50μm resolution for 5 minutes with a total of 800 projections and a voltage of 80KeV. Image datasets were reconstructed

from calibration to a bone standard (SB3, GE Healthcare) based on previously published methods (Gregg et al 2016 accepted). Post-processing was completed in MicroView (GE Healthcare) for quantification of spatial contrast levels and virtual histological sectioning, in OsiriX (Apple Inc.) for three dimensional volumetric and maximum intensity reconstructions, and MatLab (MathWorks) for modeling relative tissue perfusion changes.

Image analysis and quantification

Contrast intensities were determined spatially and temporally through virtual 2D cross sections analyzed using the Line Tool in MicroView. Contrast enhancement and degradation were modeled over 24 hours in the heart, dorsal aorta, head, and limb for samples ranging from days 4-11 of development. Virtual histological sections were taken from saggital anatomical planes in MicroView and compared to standard histology slices representing the same plane (Bellairs & Osmond, 2014). Growth metrics of the heart, lungs, and eyes were modeled as a power function (Equation 1) with a log-log scale and overall longitudinal embryonic growth was modeled as an exponential function (Equation 2).

$$F(x) = mX^n \quad (Equation\ 1)$$

$$F(x) = Ae^{Bx} \quad (Equation\ 2)$$

DICOM image stacks were imported into OsiriX and used to produce maximum intensity projections (MIP) and volumetric renderings (VR) of representative samples.

Line scan data, exported from MicroView, was plotted in MatLab for quantified contrast enhancement in the embryonic heart for days 7-8 and days 10-11 of development. Bulk nanoparticle concentration and transport was modeled from Fick's First Law (Equation 3), measured from line scan data taken perpendicularly into the myocardium from the lumen. Contrast enhancement values were converted to an amount of metal and a concentration of metal per volume calibrated to a per unit contrast in Hounsfield units based on a method previously published (Gregg et al 2016 accepted). This method enabled calculation of the flux (J), change in concentration (dC), and change in distance (dX). The concentration of nanoparticles versus distance into the myocardium was modeled to a piece-wise Gaussian distribution (Equation 4) and the transport of nanoparticles versus distance into the myocardium was modeled as an exponential distribution.

$$J = -P\frac{dC}{dX} \quad (Equation\ 3)$$

$$F(x) = Ae^{\left(-\left(\frac{B-x}{C^2}\right)\right)} \quad (Equation\ 4)$$

Statistics

A one way and two way ANOVA and post-hoc T-Test was used to compare tubocuraine hydrochloride and contrast enhancement data. Data are presented as a mean and standard deviation.

3.4 Results

Acute and long term tubocurarine hydrochloride toxicity effects and paralysis of skeletal muscle for mid-late stage live in vivo imaging

Acute and long term effects from tubocurarine hydrochloride exposure (Tb) was assessed via time of skeletal muscle paralysis as compared to Tb dosage, anatomical analysis from long term exposure, and heart rate analysis for acute and long term

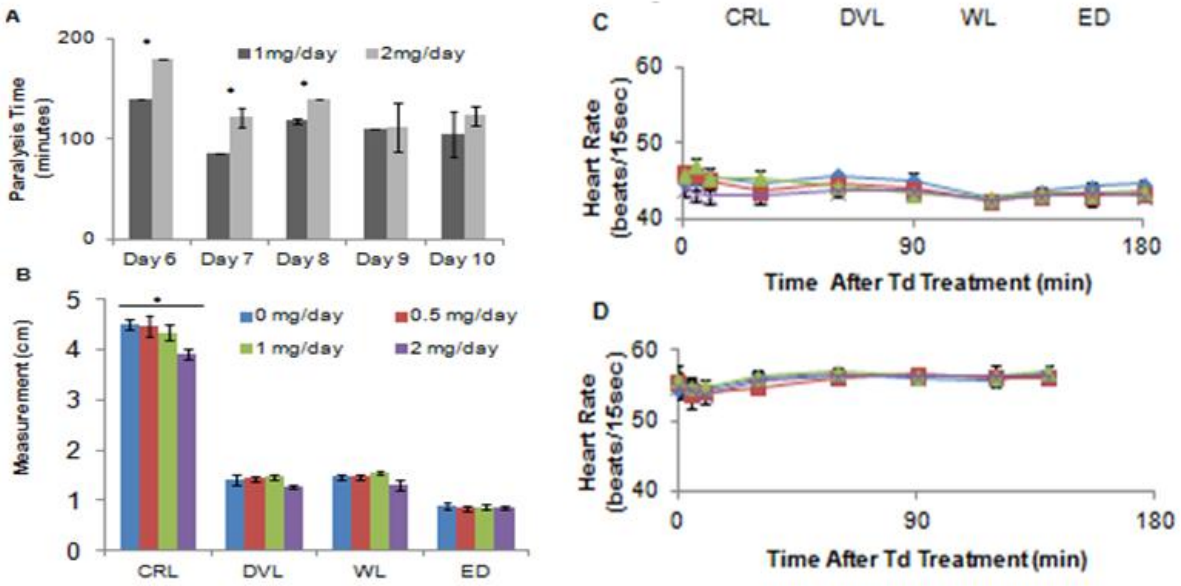

Figure 3.1 - Tb skeletal muscle paralysis efficacy and toxicity. (A) paralysis time with 1mg and 2mg Tb dosages, (B) anatomical analysis of Tb long term exposure, (C) heart rate analysis for the first and last days of long term Tb exposure

response to Tb. It was found that dosage of 1mg and 2mg of Tb was sufficient for skeletal muscle paralysis. An additional dosage of 0.5mg of Tb was proved to be insufficient for paralysis of skeletal muscles. Chick embryo samples ranging from days 6-10 of development were paralyzed for a minimum of 90 minutes before skeletal muscle function was restored (Figure 3.1A). Chick embryos were sacrificed on day 12 of development for analysis of gross morphology. The crown rump length was found to be significantly smaller than controls for 2mg dosage of Tb (Figure 3.1B) but there was no difference in the dorsal-ventral length, wing length, and eye diameter. During

paralysis, embryonic heart rate was monitored for transient changes from acute exposure to Tb and analyzed longitudinally for any progressive heart changes. Heart rates remained steady during skeletal muscle paralysis (Figure 3.1C). Furthermore, heart rates remained normal and unchanged from controls after multi-day exposure to Tb (Figure 3.1C) with rates increasing from approximately 45 beats per 15 seconds for day 6 embryos to 55 hearts per 15 seconds for day 10 embryos indicating healthy growth of samples regardless of long term Tb exposure (Figure 3.1C). From this analysis we conclude that 1mg dosage of Tb is sufficient for paralyzing skeletal muscle without causing teratogenic changes in embryo morphology. For all imaging studies presented, 1mg exposure of Tb was used for all studies using day 7-11 embryos.

Quantitative and qualitative assessment of virtual histology reveals morphological changes and tissue assembly with spatial, temporal, and age related biodistribution and persistence of nanoparticle contrast media

Virtual histology sections demonstrate the spatial, temporal, and age related heterogeneity of nanoparticle persistence measured in day 4, 7, and 10 chicks over 24 hours (Figure 3.2). Saggital sections of live embryos (Figure3. 2 A-C) qualitatively show the change of distribution and fidelity of tissue visualization with live microCT imaging. Developing tissue mesechyme and immature organ systems are readily visualized immediately post injection in day 4 embryos (Figure 3.2A) with labeled anatomy representing the heart, dorsal aorta, limb, mesocoele, and oesophagus mesenchyme (Figure 3.2A). At 8 hours post injection, the contrast media has moved out of the vasculature into the surrounding tissue mesenchyme and extra-embryonic space,

highlighting the entire embryonic body and specific delineation in some immature organ systems (Figure 3.2A) as compared to a standard histological section (Bellairs & Osmond, 2014). We consistently found that nanoparticle persistence was lowest in day 4 embryos most likely due to the immaturity of the tissue at this stage of development with particularly fast perfusion out of the vasculature. These results are consistent with our previous study (Gregg et al 2016 in review) where visualization of the embryo by 24 hours post injection was apparent but details of the embryonic body were not easily seen yielding 8 hours post injection the time at which the embryonic tissue mesenchyme is readily observable and details of select internal tissues visualized and vascularized structures readily seen immediately post injection prior to extensive nanoparticle perfusion.

Virtual histological sections of day 7 embryos immediately and 24 hours post injection demonstrate the rising spatial heterogeneity of contrast persistence in the embryo (Figure 3.2B). Highly vascularized structures are easily visualized immediately post injection including the heart, dorsal aorta, and liver along with eye chamber and part of the developing nervous system including the optic lobe and floor of the myelencephalon (Figure 3.2B). At 24 hours post injection, many of the organ systems visualized immediately post injection are still seen but spatial heterogeneity of nanoparticle biodistribution becomes evident. In the heart, nanoparticles have sequestered themselves into the myocardial wall with clear delineation between the left myocardial wall, right myocardial wall, and septum (Figure 3.2B). Furthermore, contrast has perfused into the developing soft tissue of the liver and the mesenchyme on the dorsal

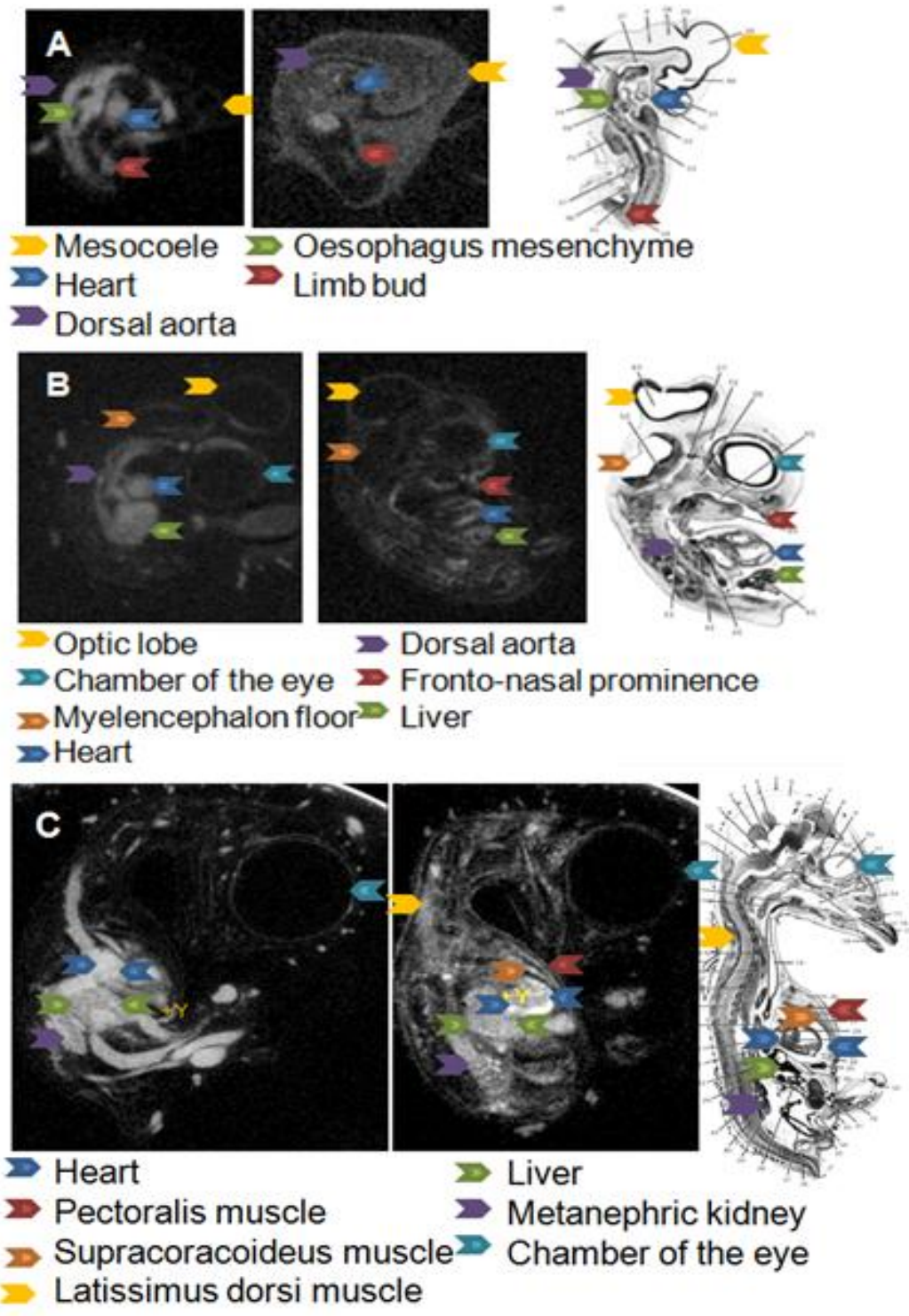

Figure 3.2 - Virtual histological sections of live embryos compared to standard histology controls. Day 4 (A), day7 (B), and day 10(C) 2D saggital sections. Day 4 (A) embryos are given at immediately post injection (left) and 8 hours post injection (right). For day 7 (B) and day 10 (C) images are given that represent immediately post injection (left) and 24 hours post injection (right)

side of the embryo. Cranial-facial features become more prominent revealing details in

the developing face, one such feature identified in the histological sections is the fronto-nasal prominence (Figure 3.2B).

Spatial and temporal contrast heterogeneity increases at day 10 of development from that of day 7 embryos with dramatic qualitative differences observed throughout the tissue. Structures associated with high vascularity are evident immediately post injection and appear to have relatively homogenous contrast enhancement with the heart, metenephric kidney, and liver being some of the more prominent features (Figure 3.2C). Virtual histology of the sample embryo 24 hours later reveals perfusion of the particle contrast into the surrounding soft tissues with appearance of the muscle and connective tissues in the head, neck, and chest (Figure 3.2C). Additionally, contrast media perfuses into the myocardial tissue, consistent with the results in day 7 embryos (Figure 3.2C). Longitudinal analysis of virtual histological sections demonstrates increasing tissue assembly and heterogeneity resulting in spatially and temporally specific nanoparticle biodistribution and increasing contrast media persistence within the embryonic body. Furthermore, comparison to standard histological sections reveals morphogenetic tissue assembly and maturation is readily visualized with increasing complexity in large scale developing organ systems that would have previously been analyzed in fixed tissue specimens. Additionally, time dependent contrast enhancement of vascularized tissues versus the surrounding mesenchyme highlights different anatomical structures depending on the time post injection of nanoparticle contrast media, all of which is non-invasively evaluated in live systems over multiple stages of development.

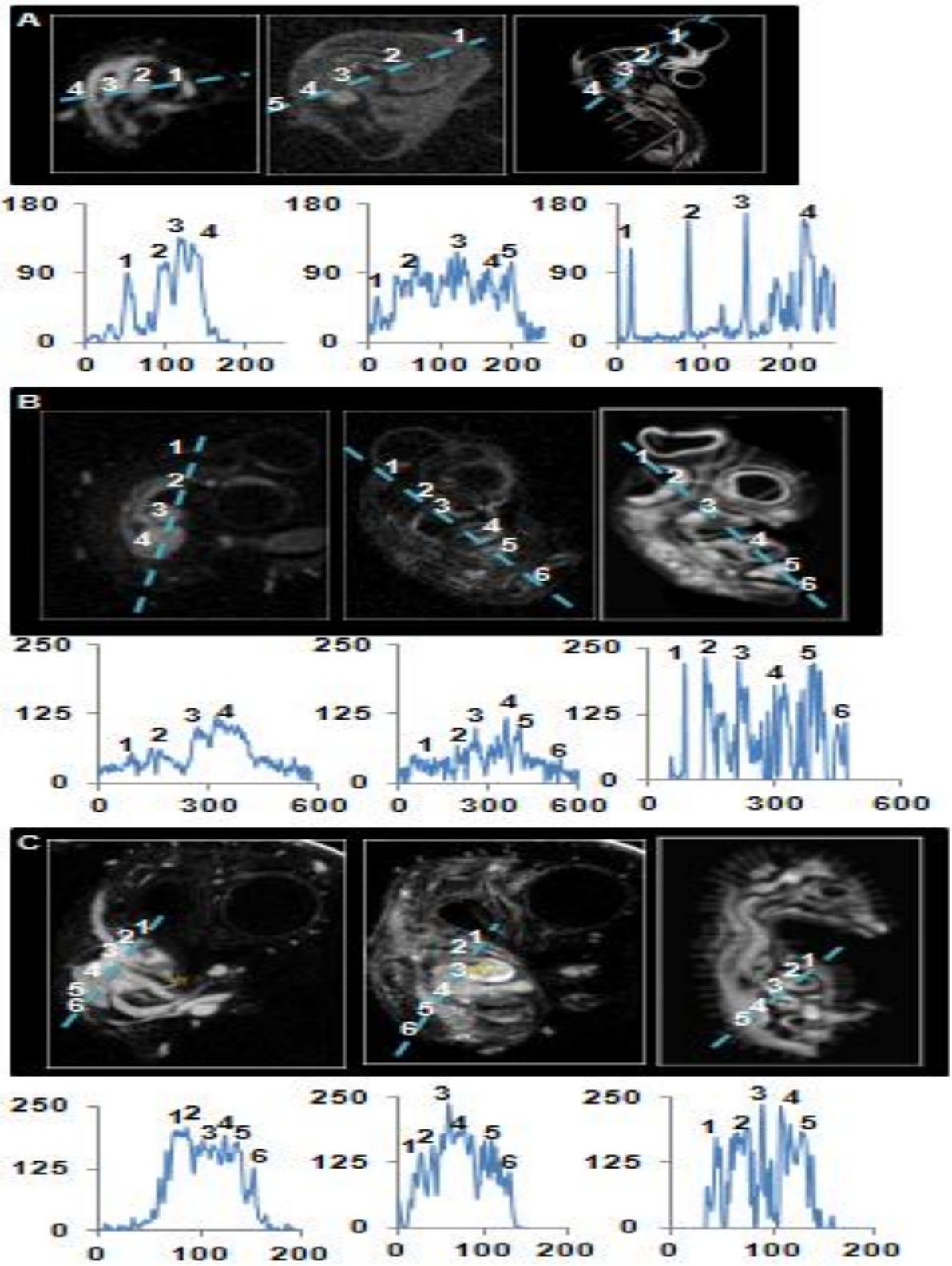

Figure 3.3 - Tissue boundary identification via grayscale mapping of line scans. Day 4 (A), day 7 (B), and day (C) representations of immediately post injection (left) and either 8 hours (A, right) or 24 hours post injection (right, B-C) as compared to standard histological sections

Quantification of tissue boundaries from virtual histological sections is comparable to

that of standard histology (Figure 3.3). Boundary signal, given in gray scale units, is stronger with standard histology than the virtual 2D cross sections of similar planes and line scan sampling but non-boundary regions have higher signal in the microCT images than that of their histological counterparts. Furthermore, longitudinal analysis of days 4, 7, and 10 embryos reveals stronger non-boundary signal intensity at later time points post injection, a consistent observation across all embryonic ages (Figure 3.3). Non-

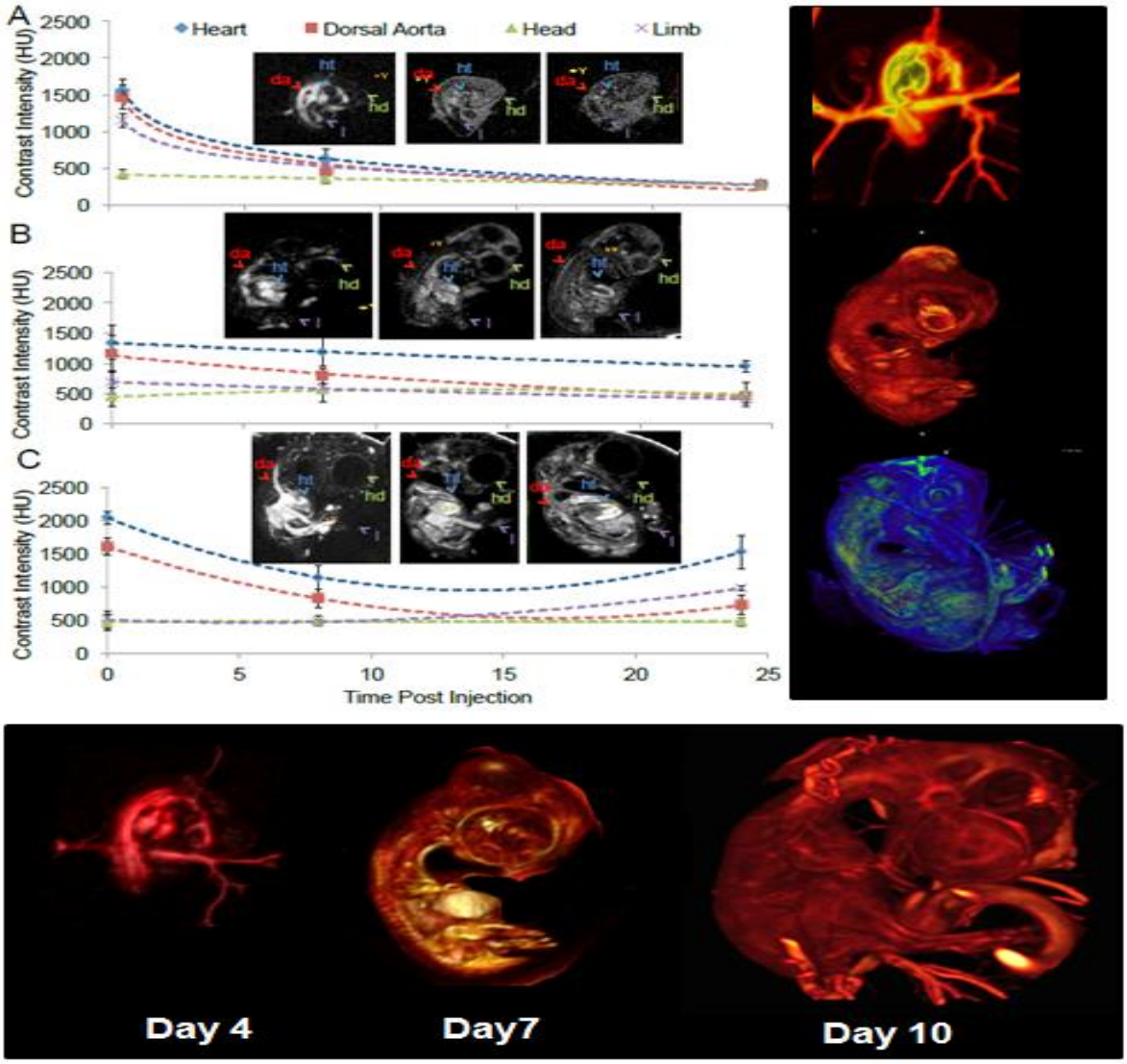

Figure 3.4 - Longitudinal biodistribution of nanoparticle contrast over multiple organ systems. Day 4 (A), day 7 (B), and day 10 (C) embryos with quantified contrast enhancement changes in the heart, dorsal aorta, head, limb, and allantois. Corresponding maximum intensity projections are given to the right of each plot. Furthermore, volumetric renderings are given for days 4, 7, and 10 embryos demonstrating the large growth of the total embryo body.

boundary signal is largely gained from developing soft connective tissues around large organ boundaries, features not as easily captured in standard histology or in early time point nanoparticle virtual histological analysis due to the persistence of particles largely in the vasculature. Nanoparticle perfusion into the surrounding tissue, enhances non-boundary signal intensities and subtle variations within these regions (Figure 3.3). Furthermore, intra-tissue anatomical details are more easily observed within standard histology but microCT 2D cross sections are qualitatively and quantitatively similar. Additionally, spatially heterogeneous sequestration of particle contrast suggests inherent tissue specific differences across the embryo with increasing divergence over development. This phenomenon, most easily observed within the developing heart, yields signal intensity specificity across tissue boundaries proportional to amount of nanoparticles present, a feature that is not present in standard histology (Figure 3.3). More specifically, quantified longitudinal nanoparticle persistence and biodistribution in selective organ systems captures the spatial, temporal, and age related differences observed in the virtual histological sections based on contrast enhancement line scan measurements (Figure 3.4). Peak contrast enhancement measurements were taken in the heart, dorsal aorta, head, and limb at three time points over 24 hours post injection at days 4, 7, and 10 of development. Biodistribution of nanoparticle contrast enhancement quickly converges in day 4 embryos regardless of organ system considered suggesting that embryonic tissues are largely similar yielding similar passive and dynamic transport responses of the particles in the embryo (Figure 4A). Significant contrast decreases in the heart, dorsal aorta, and limb within 8 hours post injection with levels changing from 1550HU to 608HU, 1460HU to 445HU, and 1145HU to 523HU

respectively (Figure 3.4A). Contrast enhancement in the head remained relatively stable and low over 24 hours post injection with levels never exceeding 400HU (Figure 3.4A). This is further visualized in the small 2D grayscale inset images with labeled anatomy (Figure 3.4A). A corresponding maximum intensity projection shows relative distribution of particles within the embryo proper and extra-embryonic vasculature (Figure 3.4A). Quantification of contrast intensity for day 7 embryos shows less convergence within the embryo with a maximum range of 500HU between any and all organ systems measured (Figure 3.4B). Contrast decreases over 24 hours post injection were far less drastic in day 7 embryos with no significant changes observed in any of the organs considered. Highest contrast was observed in the vascular structures of the heart and dorsal aorta with values being 1345HU and 1160HU respectively (Figure 3.4B). Contrast enhancement is consistently lowest in the head maintaining a tight range of 440-480HU over the course of the experiment (Figure 3.4B). The heart remains the organ with the highest proportion of nanoparticles 24 hours post injection with 950HU, particularly found in the myocardium (Figure 3.4B). MIP of day 7 embryos demonstrates tissues with sequestered particle concentrations, an observation also found in the 2D inset grayscale images with labeled anatomy (Figure 3.4B). The largest divergence of contrast enhancement is found in day 10 embryos (Figure 3.4C). The lack of convergence in contrast by 24 hours post injection further demonstrates the increase in tissue maturation and heterogeneity with age, affecting the longitudinal biodistribtution and nanoparticle persistence within the sample (Figure 3.4C). Persistence of nanoparticles within the embryonic body remains high, matching or exceeding contrast enhancement at the day 4 and day 7 embryonic counterparts

(Figure 3.4C). Additionally, spatial heterogeneity of particle distribution becomes significantly evident with differences in contrast enhancement and the pattern of contrast change measured over time. This is quintessentially observed in the limb where contrast enhancement increased from 510-980HU over 24 hours post injection, most likely due to particles moving and sequestering into the tissue of the limb (Figure 3.4C). Furthermore, large divergence in starting contrast enhancement quantified immediately post injection shows a spread of 1600HU suggesting that biodistribution is positively correlated with embryonic age (Figure 3.4C). Visualization of complex exogenous contrast intensity measurements through MIP 3D renderings of day 10 embryos demonstrates the extent of tissue assembly and maturation, a striking difference in tissue assembly and morphogenetic process that occur between days 4-10 of development (Figure 3.4 A-C). Further evidence of visualized tissue assembly and morphogenetic changes is visualized through 3D volumetric reconstructions of day 4, 7, and 10 embryos (Figure 3.4D). Tissue assembly and maturation can be seen through the increasing size and complexity within the reconstructions.

Establishment of Quantitative, Dynamic Growth Metrics through Volumetric Analysis of Live Embryos

Three dimensional volumetric image analysis via segmentation and identification of regions of interest of the heart, left/right lungs, and left/right eye were analyzed for embryonic development ranging days 4-10 in live samples (Figure 3.5B-D). ROIs were specified around each organ, thresholded by pixel intensity, and semi-automatically determined for all 2D image slices containing the organ of interest. In general, non-

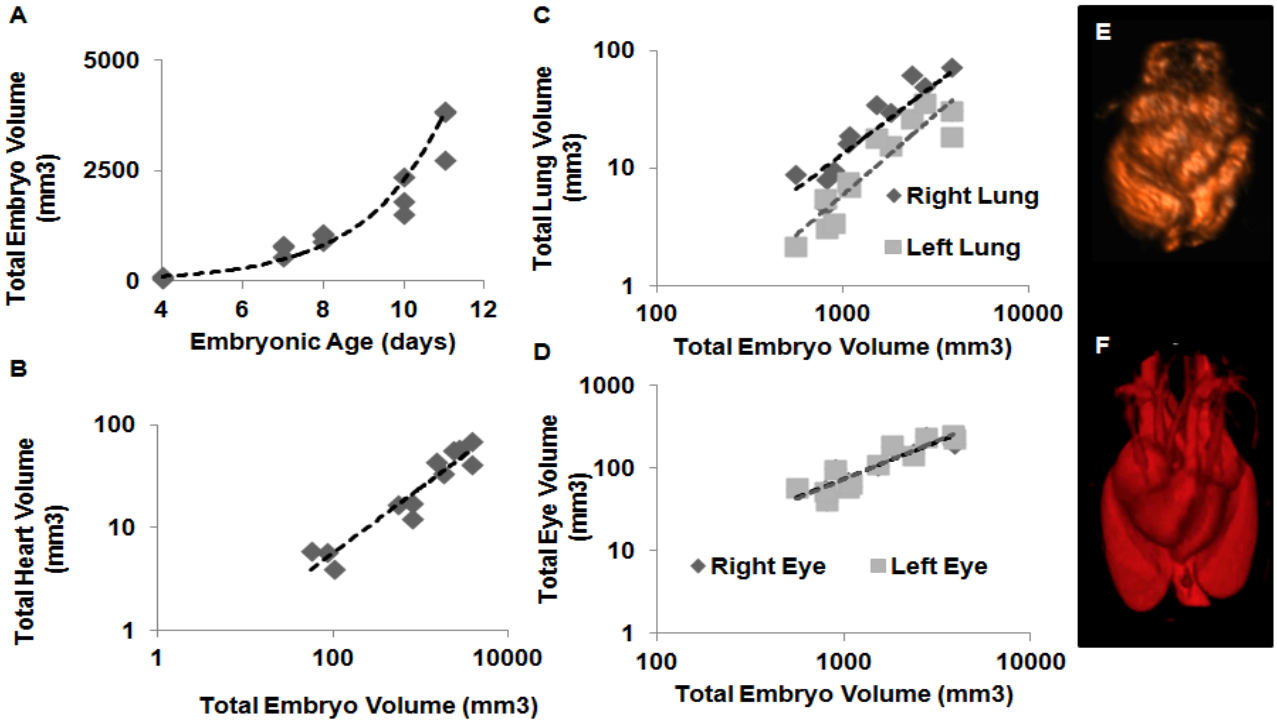

Figure 3.5 - Long term live in vivo modeled growth metrics. (A) total embryo growth vs. embryonic age showing exponential growth, heart (B), lung (C), and eye (D) growth fit to a power model. (E-F) heart and surrounding lung 3D volumetric reconstructions for day 7 (E) and day 10 (F) embryos showing the relative growth and orientation of the major thoracic organ systems

linear growth metrics were determined with organ specific spatial variance identified when appropriate, specifically in the case of the left and right lung volumes. Regression metrics were determined based on methods previously described (Kim, Min, Recknagel, Riccio, & Butcher, 2011), modeled to a power function and given in Table 3.1. Total embryonic volumetric growth was exponential over the time period assessed (days 4-11) without any significant changes in rate observed and over one full order of magnitude of growth (Figure 3.5A). Total embryonic heart growth grew by an order in magnitude between days 4-11 of development with steady volumetric growth throughout the entire time period assessed (Figure 3.5B). The right and left lungs grew steadily and at similar rates both growing between 7-8 fold between days7-11 of development. The left-right asymmetry was evident throughout the time period assessed with the left

lung consistently smaller than the right lung by approximately a factor of 1.8-2. This difference was maintained throughout development suggesting consistent growth without any significant changes in rate (Figure 3.5C). Conversely to the lungs, the eye growth was nearly identical between the left and right eyes with starting volumes of 49.3 +/- 8.3mm^3 and 50.2 +/- 8.5 mm^3 beginning on day 7 and a 4.5 fold increase in total volume to 234.5 +/- 12.2 mm^3 and 222.7 +/- 23.6 mm^3 by day 11 of development (Figure 3.5D). Three dimensional volumetric reconstructions of the heart and lungs are given for a day 7 (Figure 3.5E) and day 10 (Figure 3.5F) embryo. Increases in total growth are evident along with increased tissue assembly demonstrating a mature phenotype.

Table 3.1 - Modeled coefficients and fit for embryonic organ growth metrics

Volumetric Growth Measurement	Model Coefficients $F(x) = Ae^{(Bx)}$ $F(x) = F(x) = mX^{(n)}$	Fit (R^2)
Total Embryo Volume	A = 13.403 B = 0.5134	0.9431
Total Heart Volume	m = 0.3098 n = 0.6324	0.9029
Right Lung	m = 0.0035 n = 1.1922	0.7697
Left Lung	m = 0.0005 n = 1.364	0.8446
Right Eye	m = 0.1616 n = 0.8875	0.8281
Left Eye	m = 0.1147 n = 0.9341	0.8427

Organ Specific Spatial and Temporal Tissue Heterogeneity Captured Trough Longitudinal Analysis of Ventricular Myocardial and Lumen Contrast Enhancement Changes

Spatial and temporal nanoparticle heterogeneity throughout the embryo demonstrates the changes in tissue assembly and maturation through divergent contrast sequestration in different tissues but also the longitudinal morphological changes. We observe that spatial changes exist not only across the embryonic body but within specific organ systems, in particular organ systems with a direct vascular supply enabling transport of contrast media into the tissue. This is most apparent and readily appreciated within the developing embryonic heart. Cross section images of the day 7 (Figure 3.6A) and day 10 (Figure 3.6E) at immediately and 24 hours post injection clearly show sequestration of nanoparticle contrast media into the ventricular myocardial wall and septum with minimal contrast remaining within the ventricular lumen 24 hours post injection. Line scans sampled across the heart immediately and 24 hours post injection of day 7 hearts yields plots of contrast intensity spectra versus length across the heart (Figure 3.6B-C). Blue highlighted peaks (Figure 3.6B) represent the contrast intensity within the right and left ventricular lumen where the contrast media largely exists immediately post injection whereas the red highlighted peaks (Figure 3.6C) shows the peak accumulation of contrast media in the right, left, and septum of the ventricular myocardium. The day 7 line scan data represents a shift in contrast media from the lumen into the tissue with relatively even rates into the tissue as evident by the magnitude of contrast intensity. The average contrast intensity for each region of the line scan curves is given in the bar graph (Figure 3.6D) where significantly

decreased values of contrast intensity were found in the lumen over a 24 hour period post injection.

Similar to results in day 7 hearts, day 10 hearts magnify the changes of spatial contrast enhancement observed temporally post injection. Furthermore, right and left myocardial differences become increasingly evident in day 10 hearts over their day 7 counterparts. Visually this is seen in the 2D grayscale cross sections of the same day 10 embryonic heart immediately and 24 hours post injection. Line scan plots highlight the changes in contrast enhancement spatially and temporally. As with the day 7 hearts, the blue highlighted peaks (Figure 3.6F) capture the contrast enhancement measured in the right and left ventricular lumens whereas the red lighted peaks (Figure 3.6G) show the sequestration of contrast in the right, left, and septum ventricular tissue. Additionally, lumen contrast enhancement immediately post injection is nearly identical, representing the homogenously distributed particles within the blood but 24 hours post injection, there are striking differences in the contrast enhancement spatially across the heart suggesting material differences between the right and left sides of the heart. This diverges from day 7 hearts where nanoparticle distributions within the heart were heterogeneous but relatively even in either the myocardium or lumen at a given time point. Average contrast enhancement is summarized in the bar graph (Figure 3.6H) where significant differences were found in the ventricular lumen and nearly significant differences in contrast in the myocardium, particularly in the left ventricular myocardium.

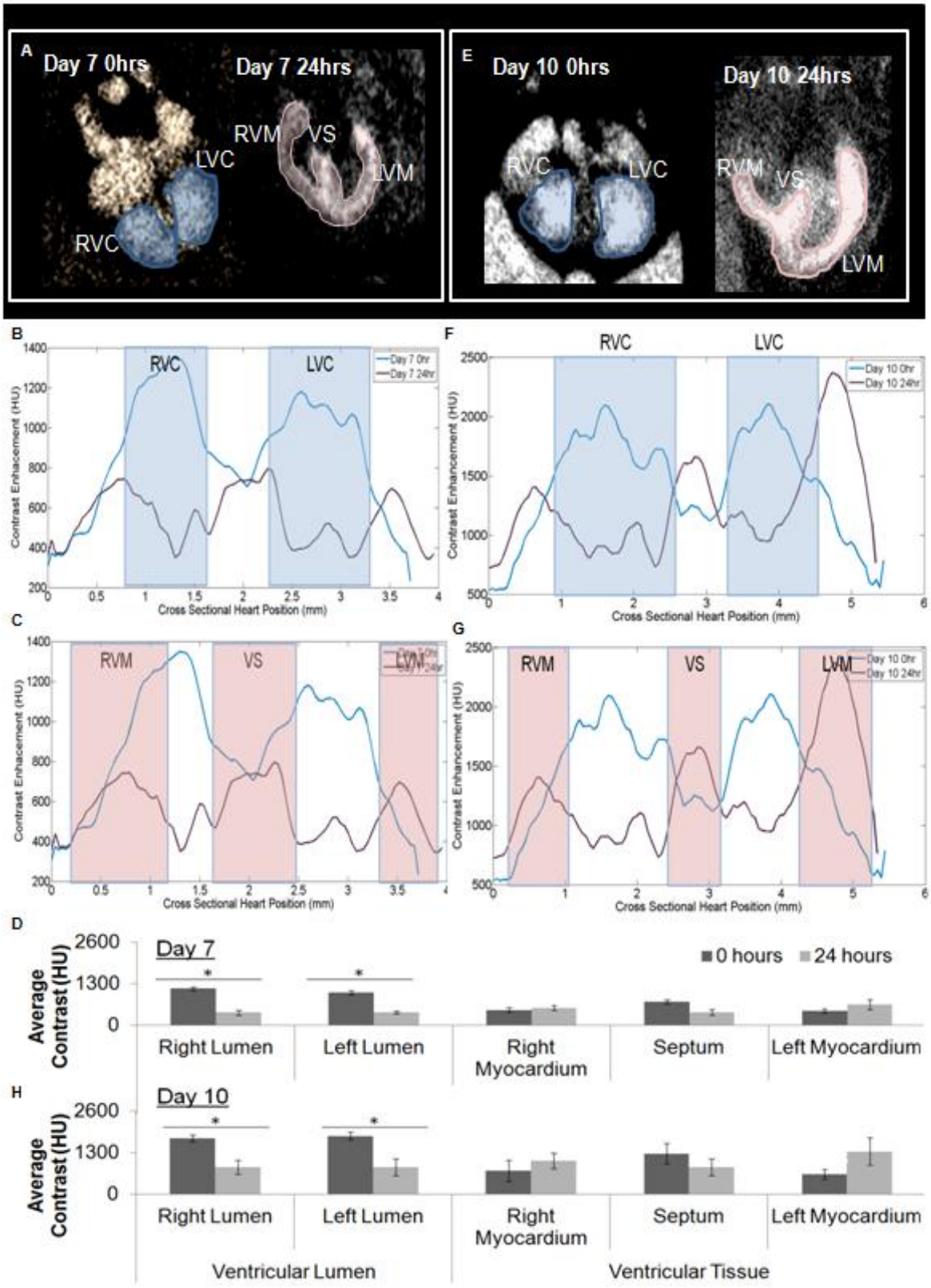

Figure 3.6 - Longitudinal myocardial analysis of spatial and temporal contrast dynamics. Day 7 (A-D) and day 10 (E-H) analysis of spatial and temporal heterogeneous contrast enhancement changes in the ventricular heart lumen and myocardium. Highlighted line scans represent peak contrast enhancement changes with overall quantified average changes given below

Longitudinal Modeled Concentration and Bulk Transport of Nanoparticle Contrast Media into the Left and Right Myocardium

Nanoparticle concentration and bulk particle transport was quantified over 24 hours into the left and right myocardium (Figure 3.7). Maximum intensity projections with corresponding color map for contrast intensity of day 7 (Figure 3.7A) and day 10 (Figure 3.7D) are given. Day 7 hearts have uniformity in the left and right myocardium with net changes of 444.5 +/- 62 HU to 650.9 +/- 150 HU and 477.9 +/- 75 HU to 545.1 +/-82.6 HU respectively suggesting small material differences within the entire myocardial walls. Conversely, day 10 hearts display increased heterogeneity between the left and right myocardial walls along with spatial differences within each wall itself elucidating inherent material differences within the myocardium as a result of increased tissue assembly and maturation. On average, changes in contrast intensity went from 623.2HU +/- 151.6HU to 1338.7HU +/- 431.6HU and 739.3HU +/- 335.4HU to 1048.1HU +/- 242.1HU for the left and right myocardium respectively. Based on the line scan data (Figure 3.6) and a nanoparticle calibration curve for amount of material per unit of contrast previously published (Gregg et al 2016 accepted), nanoparticle concentration and bulk transport was calculated over 24 hours using Fick's law and a 1D axisymmetric system. The concentration of nanoparticles between day 7 and day 10 hearts 24 hours post injection over doubles suggesting that particles are being significantly sequestered within the tissue indicative of more compact myocardium. Rates of transport, in mm^2/s, versus distance into the myocardium were plotted (Figure 3.7 B-C, E-F) and fit to an exponential distribution. For day 7 hearts, modeled transport reveals a slightly exponential increase with distance into the myocardium revealing minimal sequestration

within the tissue that would dramatically affect the concentration gradient and thus the transport rate. In day 10 embryonic hearts, the exponential increase in transport rate with distance as compared to day 7 counterparts is staggering suggesting the increased compaction of the tissue. Furthermore, a sharper ascent of the modeled curve found in the right myocardium at day 10 demonstrates an overall increase in transport rate into the myocardium elucidating to less dense muscle as compared to the left myocardium with a more depressed exponential farther into the tissue. This suggests that the transport of nanoparticles is relatively slow into the left myocardium with high accumulation of particles, resulting in the high contrast enhancement visualized. Overall concentration of nanoparticles dramatically increases in the myocardium between day 7 and day 10 of development and the rates of transport show preferentiality for particle sequestration in the left myocardium suggesting significant tissue heterogeneity by day 10 of development in the left and right myocardium. Modeled coefficients can be found in Table 3.2.

3.5 Discussion

Reliable quantitative, longitudinal live in vivo imaging of embryonic development is imperative for establishing normal and abnormal tissue patterning in response to genetic and/or environmental influences. In this study we establish to the first of our knowledge a long term live imaging platform for analysis of mid-late stage avian development. Dose dependent toxicity of Tb reveals 1mg dosage safe and effective of skeletal muscle paralysis, a necessary component for minimizing artifacts within the dataset. Furthermore, we establish longitudinal contrast enhancement biodistribution and persistence qualitatively and quantitatively between days 4-11 of development and

delineation between tissue boundary and non tissue boundary contrast intensity signals as compared to standard histological sectioning. Spatial, temporal, and longitudinal heterogeneity of nanoparticle biodistribution was evident across the embryo at the given embryonic ages assessed. Heterogeneity was observed within tissues of individual organs, particularly systems with distinct vascular supplies. We found that contrast movement in the embryonic heart from the ventricular lumen into the myocardium was spatially preferential and the rate of preferentiality changed with embryonic age. Quantifying nanoparticle concentration and rates of transport into the left and right ventricular myocardium reveal spatial differences between the right and left sides of the heart, differences that become more pronounced with older embryonic age suggesting inherent changes in material properties most likely related to tissue assembly and maturation.

Table 3.2 - Modeled parameters for bulk nanoparticle concentration and transport over 24 hours. Myocardial concentrations were fit to a piece-wise Gaussian distribution and bulk nanoparticle transport was modeled as an exponential

Myocardial Concentration Measurement	Model Coefficients $F(x) = Ae^{(-(x-B)/C)^2)}$	Fit (R^2)
Day 7 LVM	A = 13.53 B = 0.423 C = 0.3785	0.55
Day 7 RVM	A = 11.21 B = 0.4574 C = 0.5084	0.70
Day 10 LVM	A = 35.23 B = 0.5661 C = 0.5436	0.62
Day 10 RVM	A = 18.82 B = 0.6289 C = 0.6134	0.58

Myocardial Rate of Particle Transport Measurement	Model Coefficients $F(x) = Ae^{(Bx)}$	Fit (R^2)
Day 7 LVM	A = 0.00001705 B = 4.872	0.70
Day 7 RVM	A = 0.00002556 B = 2.93	0.72
Day 10 LVM	A = 0.00005647 B = 3.319	0.76
Day 10 RVM	A = 0.00001581 B = 5.71	0.73

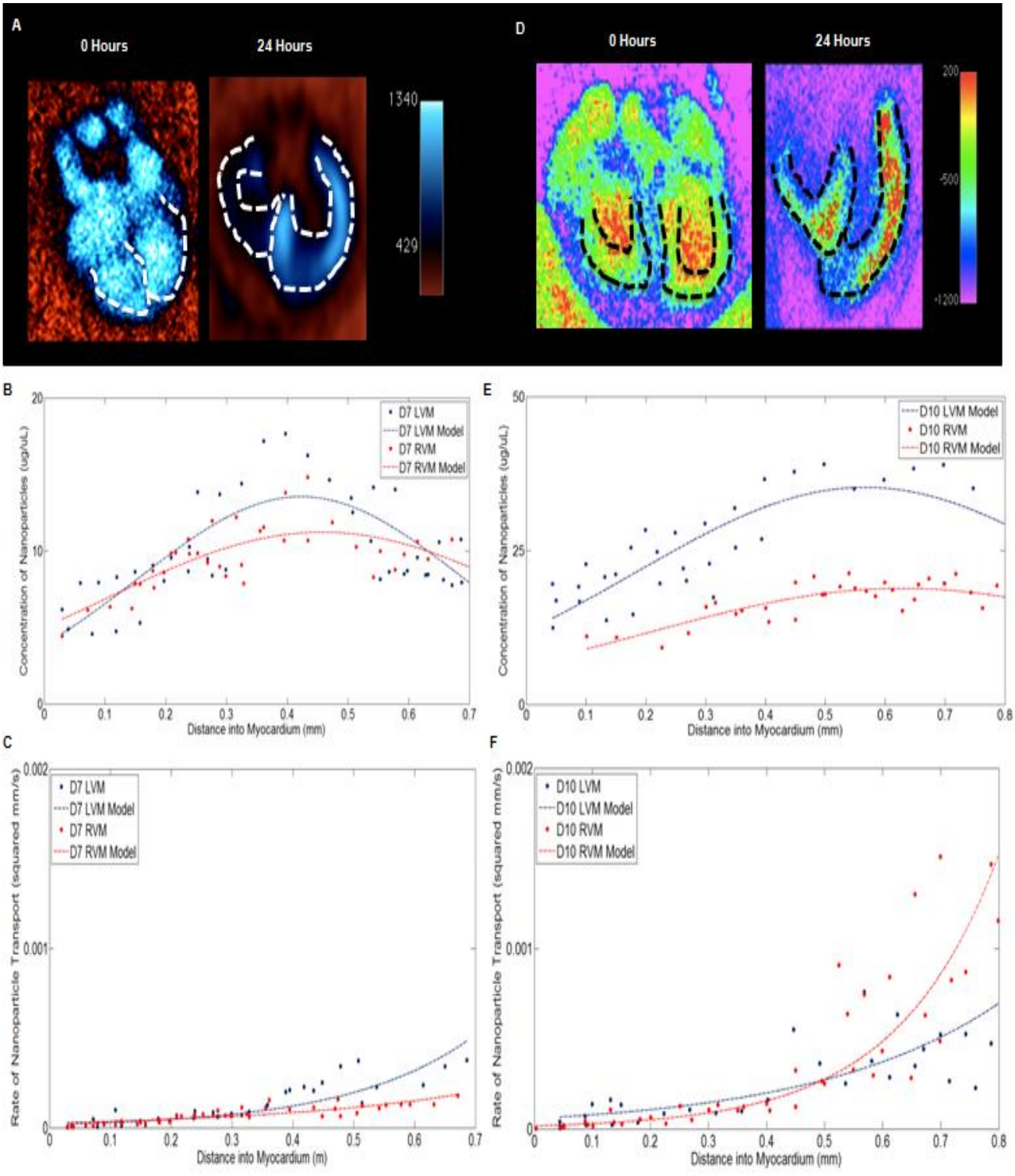

Figure 3.7 - Longitudinal transport analysis into the left and right myocardium. Day 7 (A-C) and ay 10 (D-F) concentration and bulk transport quantification into the left and right myocardium modeled as a piece-wise Gaussian and exponential distribution respectively

While microCT technologies have been used in the field of embryological research for the past 15 years (Butcher, Sedmera, Guldberg, & Markwald, 2007), they have only recently been extended to live samples. Compared to other 2D and 3D imaging technologies capable of capturing mid-late stages of development, microCT matches or exceeds other modalities in resolution, ability for high throughput image acquisition, and scan times (Kim et al., 2011). We previously screened and characterized different metallic nanoparticle contrast media for use in live embryonic samples (Gregg et al 2016 accepted) concluding that 110nm alkaline earth metal particles produced the highest amount of contrast enhancement and persisted longest in the embryo becoming the most ideal candidate for extensive live imaging studies. The use of nanoparticle based exogenous contrast media is not unique, being a valuable tool for adult animal studies across an array of biomedical applications (Ashton et al., 2014; Singh et al., 2014). Through the longitudinal study presented here, we found that nanoparticle based contrast media can be used as an imaging tool for visualization of mid-late term embryonic tissues. In addition, heterogeneous nanoparticle movements enable fundamental transport phenomena to be known, indicative of changing tissue microarchitecture. Line scan data across the ventricular lumens and myocardium revealed the spatial changes of contrast enhancement over time and embryonic age revealing bulk transport metrics into the myocardium from the lumen on the left and right sides of the heart with the assumption of uniform perfusion on the left and right sides of the heart. Color mapping of the embryonic heart reveals that the left and right myocardium are not uniform with each other or throughout each side, particularly observed in older stage embryos suggesting myocardial microarchitecture is more

formed at this time. Previous studies have demonstrated the spatial changes in the ventricular myocardium in the left and right ventricles over development (Sedmera, Pexieder, Norman, & Clark, 1997). By day 7 of development, secondary trabeculae in the ventricles are apparent and isotropic with a dorsal-ventral orientation in the left ventricle and a radial orientation in the right ventricle (Sedmera et al., 1997). Furthermore, basal trabeculae in both ventricles are finer and has a perpendicular orientation that has increasing compaction over development leading to the thick myocardium at the basal apex of the heart (Sedmera et al., 1997). Tertiary trabeculae arise at day 7 of development and continue to organize and mature with side specific orientations. Specifically, left ventricular tertiary trabeculae are primarily longitudinal with spiral ridges and some oblique connecting segments with overall similar orientation as the muscle fibers in the compact myocardium (Sedmera et al., 1997). Conversely, the pattern of tertiary trabeculae in the right ventricle is more complicated being arranged in a counter clockwise spiral beginning cranially, moving towards the apex, and then to the conotruncus mirroring the muscle fibers found in the mature right sided heart muscle (Sedmera et al., 1997). Additionally, the contribution of tertiary trabeculae in the right ventricle to the total myocardial mass is significantly higher than its left ventricle counterpart. Overall, we speculate that side specific differences in the compact myocardium along with the secondary and tertiary trabeculae are contributing to the differences in perfusion rate of the nanoparticles into the left and right myocardium both at each embryonic age assessed and the longitudinal changes quantified over multiple embryonic days. Further analysis into corroborating the ventricular microarchitecture changes with the dynamic transport of particles opens a

wealth of research opportunity for understanding critical differences in heart morphogenesis that translates directly to functional changes. Extension of this data into a three dimensional finite element model with coupled fluid-solid interactions would elucidate the spatial heterogeneity across all of the myocardium eliminating some of the assumptions we required for this study. Pairing a finite element model approach with high resolution imaging data and standard tissue sectioning and histological assays can give an ever increasing, more comprehensive analysis to the complex tissue assembly occurring during mid-late stage development. Even more so, extension of this analysis into diseased heart models would greatly contribute to the functional consequences of congenital abnormalities on cardiogenesis. While genetic models in avian embryos is far limited, environmental alterations through surgical ligations (Gould et al., 2015) given an opportunity to reveal long term functional consequences through changing the hemodynamic environments on the avian embryo and the downstream cascade of events from fluid-tissue interactions, phenomena which has been an active part of embryological research for over 20 years (Sedmera, Pexieder, Rychterova, Hu, & Clark, 1999) but lacking in all of the experimental tools necessary for gaining a complete understanding.

In conclusion, we demonstrate a novel imaging platform for capturing live embryonic morphogenesis with high resolution microCT imaging during mid-late stages of development. The data presented here represents live, static imaging with particular emphasis on the efficacy of nanoparticle contrast media on tissue enhancement, persistence, and biodistribution within the embryo at multiple stages. We also focus on

the utility of nanoparticle based contrast enhancement through quantification of bulk particle transport within the embryo. Establishing baseline metrics is critical for understanding normal tissue assembly for live embryonic development. Coupling the imaging platforms and utility of nanoparticle contrast media described here with well established gene and protein expression assays has the potential for targeting key molecular pathways implicated at multiple stages of morphogenesis. This becomes increasingly more power when these technologies are coupled with diseased models, for parsing out functional consequences of altered morphological events. Ultimately, therapeutic targets for clinical use are often targeted on the gene and protein expression levels but assessing the intervention and restored function will largely occur on the tissue scale. The ability for live in vivo 3D imaging of not only anatomical changes but material changes as well is critical for understanding underlying biological fate decisions. Future studies focusing on these outcomes could address such questions as 1) development of novel particle systems with appropriate surface chemistry for biomolecule conjugation, 2) development of coupled prospective gating image acquisition for analysis of cardiovascular dynamic in normal and diseased tissues, and 3) development of computational analysis platforms for high throughput analysis of multi-scale tissue assembly. With the development of novel and adaptation of current technologies for mid-late stage live in vivo microCT imaging of embryonic development, our understandings and capabilities of studying this elusive stage of morphogenesis will be realized.

Acknowledgements

The authors acknowledge Mark Riccio and Dr. Fred VonStein for their technical assistance in the operation of the microCT machine and image reconstructions along with the Cornell Institute for Biotechnology. J.T.B is funded by the National Heart, Lung, and Blood Institute (HL110328), National Science Foundation (CBET-0955172), and the Hartwell Foundation. C.L.G. is funded by the National Heart, Lung, and Blood Institute and the National Science Foundation.

References

Ashton, J. R., Clark, D. P., Moding, E. J., Ghaghada, K., Kirsch, D. G., West, J. L., & Badea, C. T. (2014). Dual-energy micro-CT functional imaging of primary lung cancer in mice using gold and iodine nanoparticle contrast agents: a validation study. *PloS One*, *9*(2), e88129. http://doi.org/10.1371/journal.pone.0088129

Bellairs, R., & Osmond, M. (2014). *Atlas of Chick Development*. *Atlas of Chick Development*. http://doi.org/10.1016/B978-0-12-384951-9.00013-7

Boll, H., Nittka, S., Doyon, F., Neumaier, M., Marx, A., Kramer, M., … Brockmann, M. a. (2011). Micro-CT based experimental liver imaging using a nanoparticulate contrast agent: a longitudinal study in mice. *PloS One*, *6*(9), e25692. http://doi.org/10.1371/journal.pone.0025692

Butcher, J. T., Sedmera, D., Guldberg, R. E., & Markwald, R. R. (2007). Quantitative volumetric analysis of cardiac morphogenesis assessed through micro-computed tomography. *Developmental Dynamics : An Official Publication of the American Association of Anatomists*, *236*(3), 802–9. http://doi.org/10.1002/dvdy.20962

Cui, C., Filla, M. B., Jones, E. a V, Lansford, R., Cheuvront, T., Al-Roubaie, S., … Little, C. D. (2013). Embryogenesis of the first circulating endothelial cells. *PloS One*, *8*(5), e60841. http://doi.org/10.1371/journal.pone.0060841

Czirók, A., Rongish, B. J., & Little, C. D. (2004). Extracellular matrix dynamics during vertebrate axis formation. *Developmental Biology*, *268*(1), 111–22. http://doi.org/10.1016/j.ydbio.2003.09.040

Diaspro, A., Chirico, G., & Collini, M. (2005). Two-photon fluorescence excitation and related techniques in biological microscopy. *Quarterly Reviews of Biophysics*,

38(2), 97–166. http://doi.org/10.1017/S0033583505004129

Dickinson, M. E., Simbuerger, E., Zimmermann, B., Waters, C. W., & Fraser, S. E. (2003). Multiphoton excitation spectra in biological samples. *Journal of Biomedical Optics*, *8*(3), 329–38. http://doi.org/10.1117/1.1583734

Gould, R. A., Yalcin, H. C., MacKay, J. L., Sauls, K., Norris, R., Kumar, S., & Butcher, J. T. (2015). Cyclic Mechanical Loading Is Essential for Rac1-Mediated Elongation and Remodeling of the Embryonic Mitral Valve. *Current Biology*, *26*(1), 27–37. http://doi.org/10.1016/j.cub.2015.11.033

Gregg, C. L., & Butcher, J. T. (2012). Quantitative In Vivo Imaging of Embryonic Development: Opportunities and Challenges. *Differentiation*, *84*(1), 149–162. http://doi.org/10.1016/j.diff.2012.05.003.Quantitative

Gregg, C. L., & Butcher, J. T. (2013). Translational paradigms in scientific and clinical imaging of cardiac development. *Birth Defects Research. Part C, Embryo Today : Reviews*, *99*(2), 106–20. http://doi.org/10.1002/bdrc.21034

Henning, A. L., Jiang, M. X., Yalcin, H. C., & Butcher, J. T. (2011). Quantitative three-dimensional imaging of live avian embryonic morphogenesis via micro-computed tomography. *Developmental Dynamics : An Official Publication of the American Association of Anatomists*, *240*(8), 1949–57. http://doi.org/10.1002/dvdy.22694

Hogers, B., DeRuiter, M. C., Gittenberger-de Groot, a C., & Poelmann, R. E. (1999). Extraembryonic venous obstructions lead to cardiovascular malformations and can be embryolethal. *Cardiovascular Research*, *41*(1), 87–99. Retrieved from http://www.ncbi.nlm.nih.gov/pubmed/10325956

Kim, J. S., Min, J., Recknagel, A. K., Riccio, M., & Butcher, J. T. (2011). Quantitative

Three-Dimensional Analysis of Embryonic Chick Morphogenesis Via Microcomputed Tomography. *The Anatomical Record: Advances in Integrative Anatomy and Evolutionary Biology*, *294*(1), 1–10. http://doi.org/10.1002/ar.21276

Lee, C.-L., Min, H., Befera, N., Clark, D., Qi, Y., Das, S., … Kirsch, D. G. (2014). Assessing Cardiac Injury in Mice wit hDual Energy-microCT, 4D-microCT and microSPECT Imaging Following Partial-Heart Irradiation. *Int. J Radiat Oncol Biol Phys*, *88*(3), 686–693. http://doi.org/10.1016/j.ijrobp.2013.11.238.Assessing

Melancon, M. P., Zhou, M., Zhang, R., Xiong, C., Allen, P., Wen, X., … Li, C. (2014). Selective uptake and imaging of aptamer- and antibody-conjugated hollow nanospheres targeted to epidermal growth factor receptors overexpressed in head and neck cancer. *ACS Nano*, *8*(5), 4530–8. http://doi.org/10.1021/nn406632u

Metscher, B. D. (2009). MicroCT for developmental biology: a versatile tool for high-contrast 3D imaging at histological resolutions. *Developmental Dynamics : An Official Publication of the American Association of Anatomists*, *238*(3), 632–40. http://doi.org/10.1002/dvdy.21857

Nakamura, H., & Funahashi, J. (2001). Introduction of DNA into chick embryos by in ovo electroporation. *Methods (San Diego, Calif.)*, *24*(1), 43–8. http://doi.org/10.1006/meth.2001.1155

Nebuloni, L., Kuhn, G. a, & Müller, R. (2013). A comparative analysis of water-soluble and blood-pool contrast agents for in vivo vascular imaging with micro-CT. *Academic Radiology*, *20*(10), 1247–55. http://doi.org/10.1016/j.acra.2013.06.003

Roger, V. L., Go, A. S., Lloyd-Jones, D. M., Adams, R. J., Berry, J. D., Brown, T. M., … Wylie-Rosett, J. (2010). Heart Disease and Stroke Statistics--2011 Update: A

Report From the American Heart Association. *Circulation*, 1–193. http://doi.org/10.1161/CIR.0b013e3182009701

Sedmera, D., Pexieder, T., Norman, H. U., & Clark, E. B. (1997). Developmental changes in the myocardial architecture of the chick. *Anatomical Record*, *248*(3), 421–432. http://doi.org/10.1002/(SICI)1097-0185(199707)248:3<421::AID-AR15>3.0.CO;2-R

Sedmera, D., Pexieder, T., Rychterova, V., Hu, N., & Clark, E. B. (1999). Remodeling of Chick Embryonic Ventricular Myoarchitecture Under Experimentally Changed Loading Conditions, *252*(March 1998), 238–252.

Shen, Y., Leatherbury, L., Rosenthal, J., Yu, Q., Pappas, M. a, Wessels, a, … Lo, C. W. (2005). Cardiovascular phenotyping of fetal mice by noninvasive high-frequency ultrasound facilitates recovery of ENU-induced mutations causing congenital cardiac and extracardiac defects. *Physiological Genomics*, *24*(1), 23–36. http://doi.org/10.1152/physiolgenomics.00129.2005

Singh, A., Agarwal, R., Diaz-Ruiz, C. a, Willett, N. J., Wang, P., Lee, L. A., … García, A. J. (2014). Nanoengineered particles for enhanced intra-articular retention and delivery of proteins. *Advanced Healthcare Materials*, *3*(10), 1562–7, 1525. http://doi.org/10.1002/adhm.201400051

Squirrell, J. M., Wokosin, D. L., White, J. G., & Bavister, B. D. (1999). Long-term two-photon fluorescence imaging of mammalian embryos without compromising viability. *Nature Biotechnology*, *17*(8), 763–7. http://doi.org/10.1038/11698

Supatto, W., Débarre, D., Moulia, B., Brouzés, E., Martin, J.-L., Farge, E., & Beaurepaire, E. (2005). In vivo modulation of morphogenetic movements in

Drosophila embryos with femtosecond laser pulses. *Proceedings of the National Academy of Sciences of the United States of America*, *102*(4), 1047–52. http://doi.org/10.1073/pnas.0405316102

Supatto, W., Mcmahon, A., Fraser, S. E., & Stathopoulos, A. (2009). Quantitative imaging of collective cell migration during Drosophila gastrulation: multiphoton microscopy and computational analysis, *4*(10), 1397–1412. http://doi.org/10.1038/nprot.2009.130.Quantitative

Wen, X., Wu, Q. P., Lu, Y., Fan, Z., Charnsangavej, C., Wallace, S., … Li, C. (2001). Poly(ethylene glycol)-conjugated anti-EGF receptor antibody C225 with radiometal chelator attached to the termini of polymer chains. *Bioconjugate Chemistry*, *12*(4), 545–53. Retrieved from http://www.ncbi.nlm.nih.gov/pubmed/11459459

Wessels, A., & Sedmera, D. (2003). Developmental anatomy of the heart: a tale of mice and man. *Physiological Genomics*, *15*(3), 165–76. http://doi.org/10.1152/physiolgenomics.00033.2003

Yu, B., Mao, Y., Bai, L., Herman, S. E. M., Wang, X., Ramanunni, A., … Muthusamy, N. (2015). Targeted nanoparticle delivery overcomes off-target immunostimulatory effects of oligonucleotides and improves therapeutic efficacy in chronic lymphocytic leukemia, *121*(1), 136–148. http://doi.org/10.1182/blood-2012-01-407742.

Yu, Q., Shen, Y., Chatterjee, B., Siegfried, B. H., Leatherbury, L., Rosenthal, J., … Lo, C. W. (2004). ENU induced mutations causing congenital cardiovascular anomalies. *Development (Cambridge, England)*, *131*(24), 6211–23. http://doi.org/10.1242/dev.01543

Zamir, E. a, Czirók, A., Cui, C., Little, C. D., & Rongish, B. J. (2006). Mesodermal cell

displacements during avian gastrulation are due to both individual cell-autonomous and convective tissue movements. *Proceedings of the National Academy of Sciences of the United States of America*, *103*(52), 19806–11. http://doi.org/10.1073/pnas.0606100103

Zarschler, K., Prapainop, K., Mahon, E., Rocks, L., Bramini, M., Kelly, P. M., … Dawson, K. a. (2014). Diagnostic nanoparticle targeting of the EGF-receptor in complex biological conditions using single-domain antibodies. *Nanoscale*, *6*(11), 6046–56. http://doi.org/10.1039/c4nr00595c

CHAPTER 4

THREE DIMENSIONAL, LIVE IN VIVO DYNAMIC MICRO-COMPUTED TOMOGRAPHY IMAGING OF AVIAN CARDIOGENESIS THROUGH PROSPECTIVE GATING ACQUISITION

4.1 Abstract

Dynamic imaging of live heart development is essentially for understanding the functional contributions of morphological events that contribute to normal and abnormal heart development. Clinically relevant congenital heart defects arise during the mid-late stages of development where live optic imaging techniques are ineffective at capturing the dense and tortuous anatomy. Here we establish a means for prospectively gating imaging acquisition of 3D microCT datasets of the avian embryonic heart beat. Through fiber optic visualization of the heart beat, a user defined tracking algorithm enables peak systole and peak diastole image datasets to be gathered in real time. Timed image specification was achieved through following light intensity changes from heart and/or proximal blood vessel movements from user defined sampling sections in the field of view. Dynamic imaging analysis at days 9 and 11 of development reveals volumetric changes and the ejection fraction at a single age and longitudinally over multiple ages. Dynamic volume changes between peak systole and peak diastole increased between 1.4-2.0mm^3 between days 9-11 of development and the ejection fraction increased up to 55% in some instances. Contour and surface mapping of peak systolic and diastolic ventricles reveals obvious differences in ventricular shape, location and relative amount

of remaining blood within the lumen, and changing myocardial architecture with apparent orientation of heart morphology circumferentially and longitudinally with respect to the apical-basal axis for the right and left ventricle respectively. Coupling cardiac morphodynamics to known morphogenetic patterning events is a critical step in fully understanding healthy and diseased tissue progression.

4.2 Introduction

Long term function and fidelity of biological tissues is established through the assembly and organization of tissue patterning during embryonic development. The processes driving tissue composition and mitigating healthy and unhealthy anatomy is poorly understood. When developmental programming between genetic and/or environmental cues proceeds incorrectly, there is a risk of congenital malformation. The most common and deadly congenital malformation, congenital heart defects (CHDs), have an estimated incidence rate as high as 10 in 1000 live births (Hoffman & Kaplan, 2002). Furthermore, 45% of deaths resulting from congenital disease are due to a cardiac malformation (Yang, Khoury, & Mannino, 1997). Detailed mechanistic understandings of early cardiac development have been thoroughly established from experimental perturbations and genetic manipulations in a variety of animal models (e.g. chick, mouse, zebrafish (Chakraborty, Combs, & Yutzey, 2010; Olson & Nes, 2006; Person, Klewer, & Runyan, 2005)). Genetic contributions to congenital disease vary but less than 10% of CHDs can be traced to a direct genetic origin (Pierpont et al., 2007) but instead arise from alterations in the interactions of multiple signaling networks with

transcriptome-wide changes following genetic (Chakraborty, Cheek, Sakthivel, Aronow, & Yutzey, 2008; Kruzynska-frejtag, Machnicki, Rogers, Markwald, & Conway, 2001; Tkatchenko et al., 2009) or mechanical perturbations (deAlmeida, McQuinn, & Sedmera, 2007; Lucitti et al., 2007).

Live embryonic imaging studies have almost exclusively been performed during the earliest stages of development spanning gastrulation and axis orientation events using optical techniques. Clinically survivable congenital malformations occur at later stages of development where there has been a critical unmet need for technologies allowing 3D live in vivo embryonic imaging for the study of longitudinal consequences in tissue patterning (Henning et al., 2011). We have recently shown that micro-computed tomography (microCT) imaging is highly effective for live 3D imaging of embryonic development during the mid-late stages (Henning et al., 2011, Gregg et al 2016 in review). MicroCT has the high spatial and temporal resolution needed to capture the dense and tortuous anatomical changes longitudinally during development. Specifically for cardiogenesis, static live 3D imaging is limited for capturing the anatomical and physiological changes occurring. While high resolution static imaging can yield 3D information about the embryonic heart, the continual movement impedes data acquisition and phase specific information is unable to be known. Data based on functional consequences of normal and abnormal development requires dynamic imaging with gated acquisition.

Dynamic heart imaging is essential for revealing mechanisms that underlie cardiogenesis. Having timed specification for image acquisition – gating – reduces motion artifacts and results in clearer image datasets. Image gating can be completed in one of two ways 1) prospectively and 2) retrospectively. Prospective image gating is performed during the image scan, timing acquisition with a periodic signal, commonly the heart beat (Gregg & Butcher, 2012). Prospectively gated images are "phase locked" meaning all captured images of the heart are taken with the same conformation, specified by the user. Conversely, retrospective gating acquires all images for the dataset and then they are sorted by either spatial or temporal periodic signals (Gregg & Butcher, 2012). An electrocardiogram is not available for the embryo and gating is typically acquired off of movement from the heart or large blood vessel achieved optically (Taylor et al., 2011)(Chan, Lin, & Cheng, 2009). There are many successful examples of retrospective gating in the embryo (Liebling, Forouhar, Gharib, Fraser, & Dickinson, 2014)(Liu, Wang, Thornburg, & Rugonyi, 2014)(Yoo, Larina, Larin, Dickinson, & Liebling, 2011) but it requires tremendous amounts of data to be rapidly acquired, stored, and sophisticated post-processing algorithms to be developed for binning the information based on periodic signals in the dataset (Gregg & Butcher, 2012).

Coupling 3D micro-computed tomography (microCT) imaging technology with prospectively gated image acquisition is a promising and attractive means for obtaining high resolution, dynamic image data sets of the live embryonic heart. The embryo does not have an established ECG and electrical leads cannot be attached to the embryo;

therefore, it is imperative to design a non-invasive, reliable system that tracks the embryonic heart beat and supplies a trigger to the imaging system. In this study, we fabricated and validated a prospective image gating system that visualized the heart rate by focusing a CCD camera connected to a 30,000 element fiber optic custom built with a lens over the extra-embryonic vasculature for identifying an oscillating blood vessel in close proximity to the embryonic heart. Furthermore, two dimensional motion control of the fiber optic enables hands free user defined focusing while the sample is in the bore of the microCT. A custom built tracking algorithm processes the heart rate and triggers the microCT machine at peak systole or peak diastole. Gated image analysis reveals peak volumetric changes of the right and left ventricles at day 9 and day 11 of development with extrapolated ejection fraction. Comparison to negative, non-gated controls reveals phase specific dynamic heart information versus blurred, ambiguous heart conformation in the non-gated image datasets. We conclude that dynamic live in vivo microCT imaging of cardiogenesis via prospectively gated image acquisition is critical for insights into functional consequences of development reflecting real time tissue assembly and maturation.

4.3Experimental Procedures

Gating Hardware and Motorization

A 30,000 element fiber optic cable with a custom lens (Myriad Fiber Imaging Tech) and a mirror positioned at 45˚ was used to visualize the sample with a working distance of approximately 1cm. The non-lens fiber end was imaged with a 10x objective connected to a CCD camera (Grey Point Systems). Coupled to the fiber optic was a light guide

connected to a standard white light LED. A 3D translational stage (Thor Labs) adjusts the field of view (FOV) and focus of the image. Two dimensional motion control of the coupled fiber optic and light guide was controlled by actuating and Servo motors. An elongated actuator that moves the whole hardware assembly into and out of the microCT bore resting on the machine platform. A rotational Servo motor attached to the fiber optic and light guide moves the hardware in a second direction. The fiber optic cable and light guide are moved in a single degree stepwise manner while being supported on a horizontal surface; therefore it moves in a single direction.

Tracking algorithm development, integration with, and triggering of the microCT machine

To maintain the viability of the embryo, a non-invasive approach was required to track the heart rate without having any physical connections to the embryo. Traditionally, the heart rate is obtained from an electrocardiogram, something of which is inaccessible in the embryo. Furthermore, attaching electrodes to the embryo would most certainly be lethal to the embryo. Direct visualization of the beating heart or proximal oscillating blood vessel is the safest and easiest accessible mean to determine the heart rate. Oscillating blood vessel images are analyzed by in-house software. The program displays the images (30 frames/second) and a running plot of the blood vessel oscillations (sine wave) visualized by the user in real time. The user selects the area on the image to be analyzed by highlighting it by a green rectangle, generating the sampling area. This must be placed at an edge of the blood vessel where the light intensity oscillates with each pulse. The peak maxima (systole) or minima (diastole) are

detected by analyzing the intensity at the edge of the blood vessel over the past 5 points sampled. The algorithm determines where the maxima and minima are is as follows: if the third time point has a higher intensity than the other four points then that third time point must have been a maximum but if the third time point is lower than the other four points then that third point must have been a minimum. This algorithm is run for every single data point that is acquired in real time to detect the maxima and minima as they occur. The light intensity coming from the lamp and reflecting on the embryo can flicker either because of variations in intensity of the lamp itself or because of subtle movements by the embryo and extra embryonic space. These variations in intensity can introduce a distortion in the algorithm which might detect a maximum or minimum in intensity which was not caused by the heart rate. To deal with this problem, the values of intensity that are used by the algorithm are normalized to the average value of the background intensity of the image. This assumes that the changes in intensity due to artifacts are evenly spread across the image. The maximum or minimum images that correspond to that detected by the algorithm are rapidly stored for validation consistent peak signal detection. An Arduino microcontroller is used to trigger the microCT machine when it receives the signal via the algorithm by sending a 5V TTL pulse to the machine. The microCT machine can gate at a speed of 500ms with a 10ms delay time period.

Preparation of embryonic samples and in vivo microinjections

Fertilized white leghorn eggs (Cornell Poultry) were cultured in ovo after 3 days of incubation at 99.5˚F and 55% humidity based on a previously described protocol

(Nakamura & Funahashi, 2001). The shell is cleaned with 70% ethanol and 6-7mL of albumen was removed with a sterile syringe and 21 gauge needle placed through the shell at the narrowest end of the egg. Masking tape is used to secure the hole from the needle and two additional strips of masking tape are placed down the length of the egg. Sterilized dissecting scissors were used to make a small window in the shell for visualization and experimental access to the embryo. The window is secured with sterile plastic wrap for the duration of the experiment and the embryo is housed in a sterile Styrofoam incubator maintained at proper temperature and humidity.

A gravity driven pressure gradient connected to a micromanipulator was used to inject day 9 and day 11 chick embryos with 110nm alkaline earth metal nanoparticle (110nm EXTN, Miltenyi Biotec) contrast media which has already previously been characterized for microCT based embryonic imaging technologies (Gregg et al 2016 in review, Gregg et al in preparation). Embryos were imaged immediately post injection in order to have contrast media remain within the vasculature for imaging prior to extravasating into the tissue. The embryos were treated with 1mg tubocurarine hydrochloride (Tb) for temporary skeletal muscle paralysis for the duration of the experiment. Tb has already been characterized in a previous study (Gregg et al in preparation).

In vivo microCT scanning and post-processing

Embryos were scanned on a GE Healthcare eXplore CT 120 machine at 50µm resolution with a total of 220 projections for a scan lasting approximately 10 minutes. Non-gated controls were imaged at the same, resolution, x-ray tube voltage, and

number of projections. Image datasets were calibrated to a bone standard (SB3, GE Healthcare). Post-processing was completed in OsiriX (Apple Inc.) for chamber volumetric analysis and 3D volumetric reconstructions and MatLab (MathWorks) for 3D surface plots of grayscale intensity changes. Regions of interest (ROI) were defined within each chamber measuring total blood volume at the given time point within the cardiac cycle with peak systole and peak diastole blood volume measurements being of interest. Ejection fraction was calculated based on the volumetric changes measured (Equation 1).

$$Ejection\ Fraction = \frac{(end\ diastolic\ volume - end\ systolic\ volume)}{end\ distolic\ volume}\ x\ 100 \quad (Equation\ 1)$$

Contour and surface mapping was completed in MatLab (MathWorks Inc.). Segmented three dimensional surfaces of the right and left ventricles based on 3D volumetric rendering data was imported into MatLab and converted to grayscale. Contrast intensities from the original 3D surface was mapped as an 8bit image and then scaled from 0-1 for color mapping correlating to the initial 0-255 grayscale for all contours and surfaces (Figure 4.1).

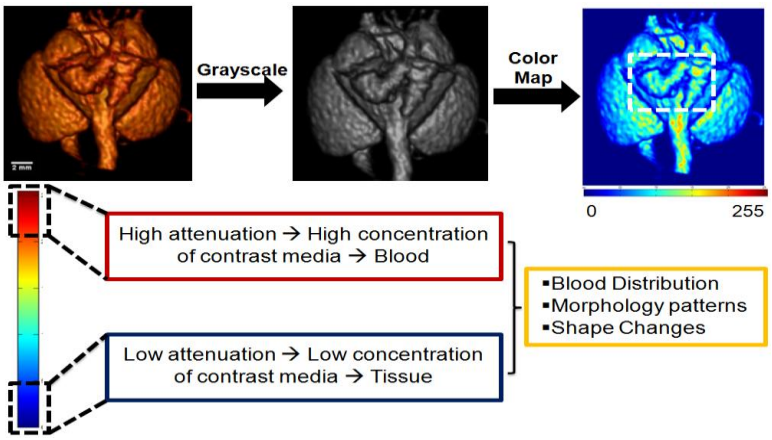

Figure 4.1 - Functional flow diagram of surface and contour plots. Surface and contour plots produced in MatLab were constructed based off of attenuation.

Statistics

One way and two way ANOVA with post T-test was used to determine significance. All data are reported as mean and standard deviation with a $p<0.05$ determining statistical significance.

4.4 Results

Signal acquisition, tracking, and synchronization with microCT imaging produces high fidelity prospective image gating

The gating hardware and software were designed to operate in a continual loop for the duration of a microCT imaging scan. In the instance of this study, a single scan consisted of 220 projections for a single rotation of the gantry. Once the oscillating blood vessel was visualized, the tracking algorithm continuously monitored the oscillations from a user defined sampling area of the vessel edge. A flow diagram is given in Figure 4.2 of the looped sequential events that are required for gathering a single data set. Once the signal is visualized by the user, collection of maximum or minimum image data is gathered by tracking the signal and triggering the microCT machine with a 5V pulse (Figure 4.2). Once the image is acquired, the gantry rotates approximately 1.64˚, a process that takes roughly 600ms. Once all 220 projections have been acquired, a separate scan gathers an image dataset for the opposite heart conformation yielding a total of 2 image datasets, one at peak systole (maximum) and one at peak diastole (minimum). A fail safe mechanisms will trigger after 2 seconds if the tracking algorithm does not identify a maximum or minimum peak (Figure 4.2) for

protection of the microCT machine and x-ray tube. The number of “dummy” pulses is recorded for identification of accuracy of the scan. It is natural for a small percentage of projections to be the result of the “dummy” signal based on the natural variations in embryonic heart rate over time and/or light intensity artifacts that can occasionally be encountered. All image data used for the results presented here were based on an 85% accuracy rate or higher for data collection.

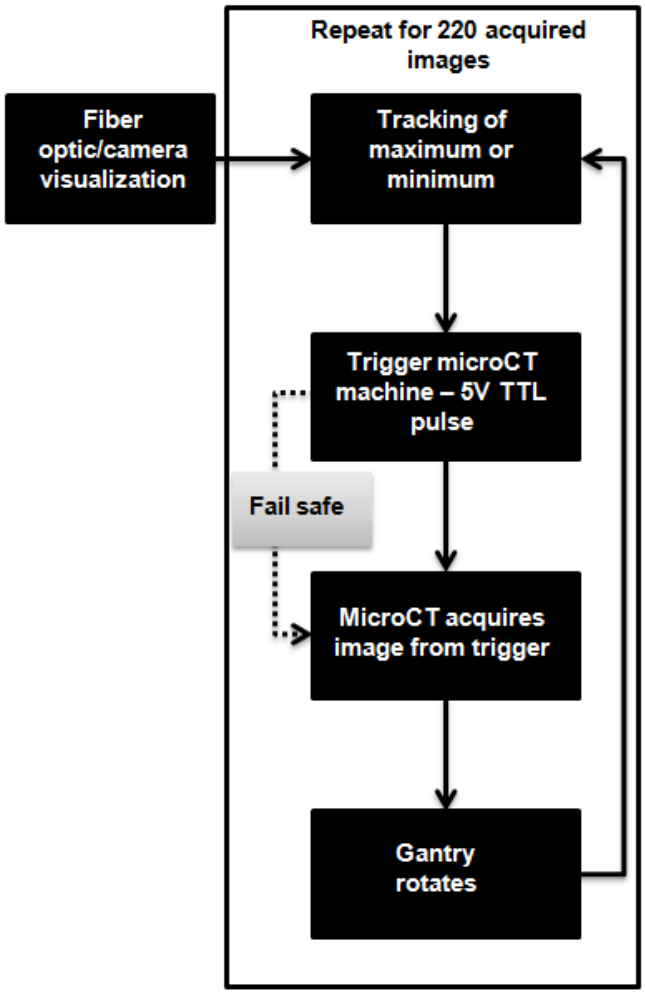

Figure 4.2 - Functional flow diagram of prospectively gated image acquisition

The gating hardware is comprised of a 30,000 optical fiber bundle with a custom built lens and coupled to a light guide for visualization of the embryo during the entire imaging acquisition (Figures 4.3A-B). A dichroic mirror is placed at a 45˚to focus the light onto the embryo. The end of the fiber optic is imaged by a 10x objective connected to a CCD camera with a speed of 30 frames per second (Figures 4.3A-C). Actuating and servo motors enable 2D motion control of the fiber and light guide (Figure 4.2A). The embryo and extra-embryonic blood vessel networks are illuminated by a white light LED (Figure 4.3D). Embryonic blood vessel networks are visualized through the fiber optic (Figure 4.4A) based on an oscillating heart rate signal (Figure 4.4C). Total light intensity values are calculated by a user defined sampling area (Figure 4.4A) denoted by a green rectangle. The sampling area is best placed on the edge of the oscillating blood vessel (Figure 4.4B), for strong additive change of light intensity based on the blood vessel edge cyclically moving into and out of the sampled region (Figure 4.4B).

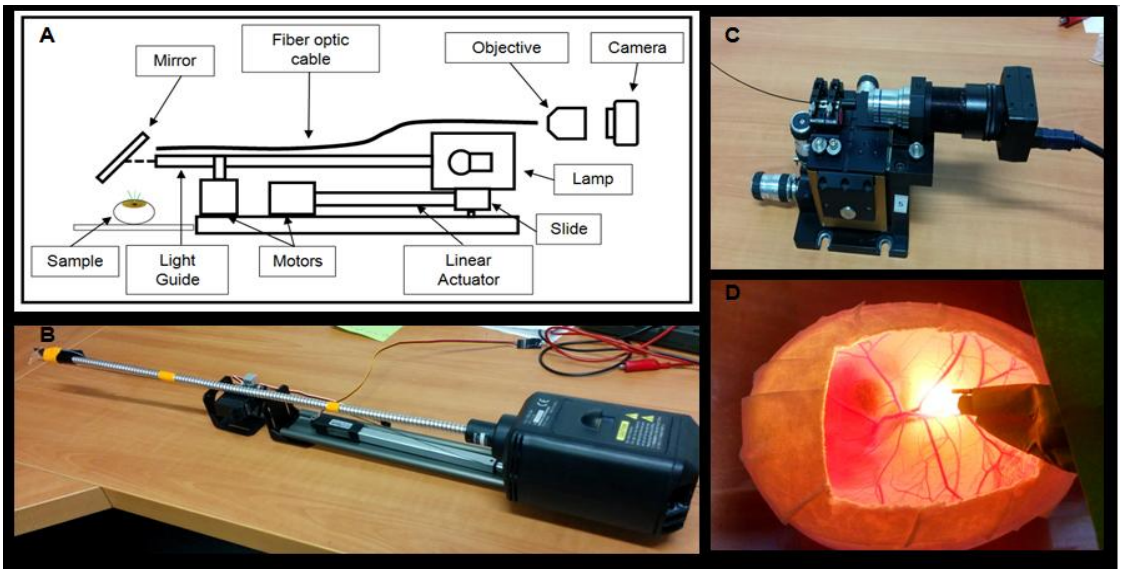

Figure 4.3 - Gating hardware schematic and images. (A) Direct visualization hardware with a 30,000 fiber optic bundle and camera, (B) fiber optic and light guide coupled together with a white light LED, (C) the fiber optic is imaged with a 10X objective and camera, and (D) day 9 chick embryo sample with direct visualization of an oscillating blood vessel

Real time tracking of the heart rate sinusoid is critical for having appropriate triggering. Prospective gating is based on discrete, precise image acquisition within the cycle (Figure 4.5A). A tracking algorithm based on the continuous sampling of 5 point clusters determined the maximum or minimum. Sampled points p1, p2, p3, p4, and p5 represent a set of points being evaluated. If p3 is larger than p2 and p4, p2 is larger than p1, and p4 is larger than p5 then p3 is the maximum and a 5V pulse is sent to the microCT machine via an Arduino microcontroller (Figure 4.5B) with the opposite sequence being true for a minimum. A graphical user interface (GUI) was designed for implementation of maximum and minimum gating (Figure 4.5C). The interface displays the real time plot of light intensity versus time and the image captured by the fiber optic (Figure 4.5C). The user denotes prior to gating if the maximum or minimum will be acquired. The algorithm operates on a greater than 85% accuracy for all image data sets acquired (Figure 4.5D). An oscillating sine wave (blue) of a day 9 embryo and vertical indications of triggering points (red) represent a standard waveform gathered during gating (Figure 4.5D).

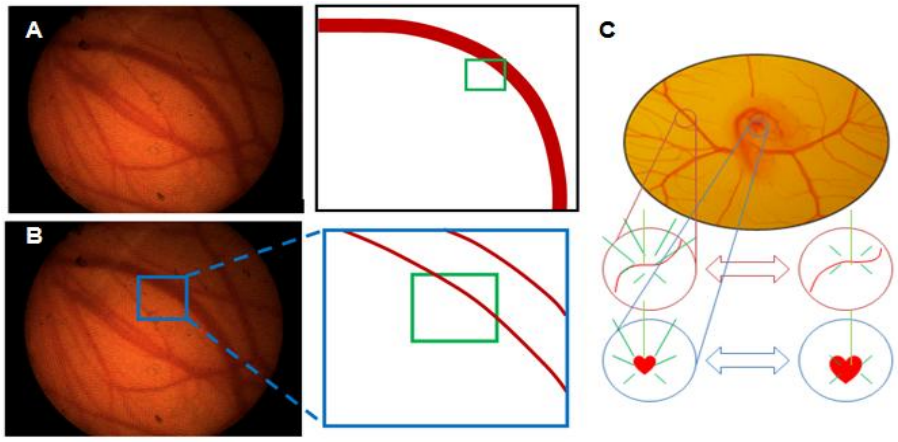

Figure 4.4 - Visualization of embryo heart beat tracking. (A) direct visualization of the heart or oscillating proximal blood vessel. (B) user defined sampling area tracks the movement of the edge of the vessel through changes in light intensity, and (C) identification of the signal origin through visualization of the heart or proximal oscillating blood vessel

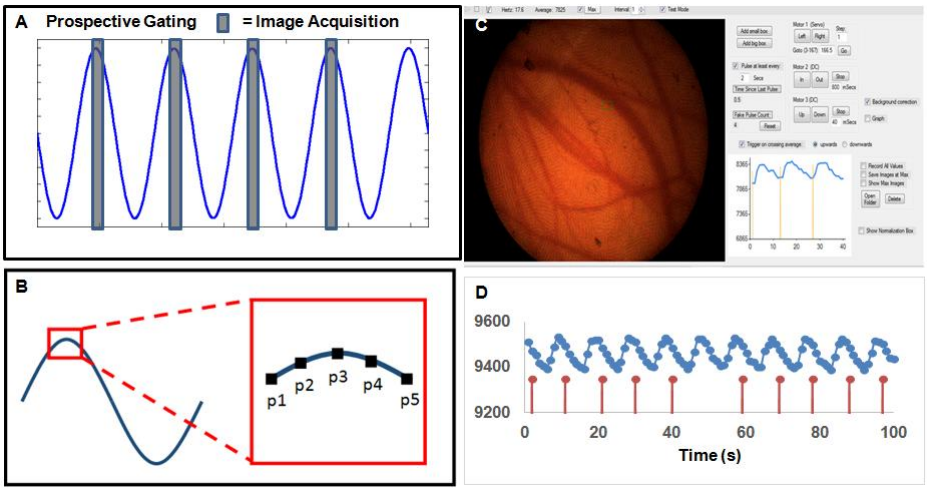

Figure 4.5 – Tracking algorithm for identification of the maximum or minimum. (A) schematic of prospective gating logic, (B) sampling of 5 continuous points if p1<p2<p3>p4>p5 then a maximum is determined. The opposite logic holds true for a minimum. (C) software user interface with real time image and running light intensity plot from the sampling area. (D) real time sampled data with the blue sine wave of the heart beat and the red vertical bars show where triggering occurs on the maximum

Prospectively gated image data produces phase specific 3D live in vivo images of dynamic and functional contributions to embryonic heart development

Volumetric renderings of day 9 and day 11 chick embryos gated at peak systole and peak diastole compared to non-gated controls demonstrate the phase specific information obtained through the gated image data sets (Figure 4.6). Non-gated controls are non-descript and ambiguous regarding the phase of the heart. Furthermore, dynamic information within the cardiac cycle of a single embryonic age and functional information based on longitudinal assessment over multiple embryonic ages is impossible to know without the gated image data sets. Gated images are shown of the heart and surrounding lungs for perspective on the chamber dynamics at the extremes within the cardiac cycle (Figure 4.6). Volumetric assessment determined systolic and diastolic right and left ventricular chamber volumes (Figure 4.6, Table 4.1).

Significant changes between diastolic and systolic chamber volumes were found for both the right and left ventricles (Figure 4.6). This is corroborated by volumetric reconstructions of representative systolic and diastolic hearts given for both day 9 and day 11 samples (Figure 4.6). Peak volume changes in the left ventricle increased from 3.3mm^3 to 4.7mm^3 between days 9-11 of development (Figure 4.6, Table 4.1). This is reflected in an increase in ejection fraction from 42.8% to 49.8%, demonstrating enhanced tissue function and maturation over the time period assessed. Similarly, the right ventricular chamber volume peak changes increased from 3.3mm^3 for day 9 embryos to 5.3mm^3 in day 11 embryos which yielded an ejection fraction change from 44.5% to 53.6% (Figure 4.6, Table 4.1). Collectively, the average volumetric ventricular change during the cardiac cycle increases from 3.3mm^3 to 5mm^3 and the ejection fraction rises to 53% from 44.6% from day 9 to day 11 of development suggesting enhanced overall myocardial function of the heart and increased heart micro-architectural tissue assembly.

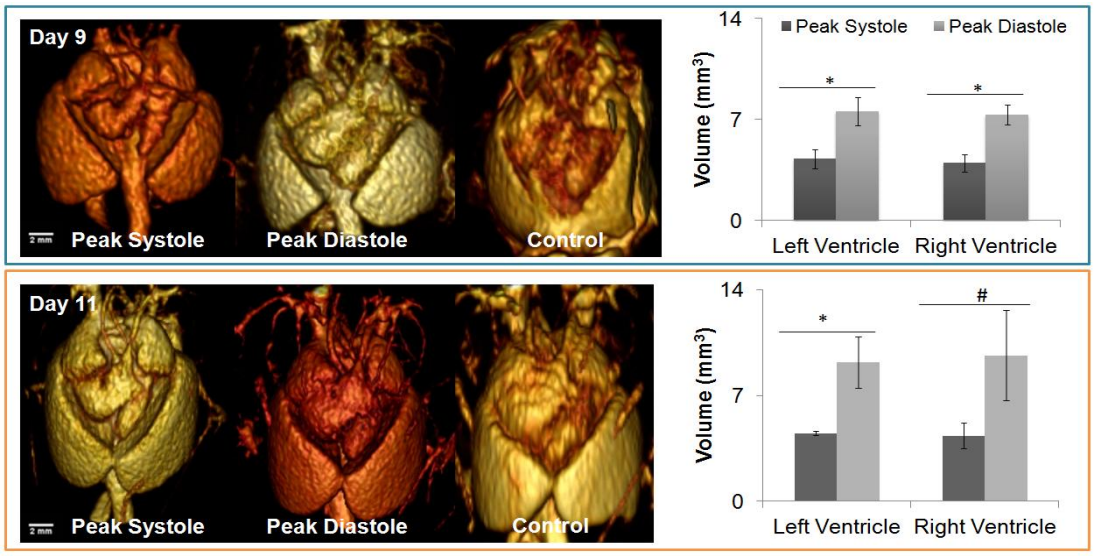

Figure 4.6 - Dynamic volumetric analysis of day 9 and day 11 embryonic chick hearts. Systolic, diastolic, and control 3D volumetric reconstructions for day 9 (top) and day 11 (bottom) embryos with corresponding measured lumen volume changes in the right and left ventricles.

Table 4.1 - Dynamic and functional volume and ejection fraction changes in day 9 and day 11 embryonic hearts

Metrics	Left Ventricle		Right Ventricle	
Dynamic Analysis Metrics	Day 9	Day 11	Day 9	Day 11
Dynamic Volume Change (mm^3)	3.3 +/- 0.65	4.7 +/- 0.93	3.3 +/- 0.81	5.3 +/- 1.9
Dynamic Ejection Fraction (%)	42.8 +/- 13	49.8 +/- 9.5	44.5 +/- 15	53.6 +/- 11

Ventricular Chamber Morphology, Blood Distribution, and Trabecular Density via Dynamic Contrast Enhancement Changes in the Cardiac Cycle

Through volumetric 3D reconstructions, right and left ventricular chambers were segmented, converted to grayscale and modeled as contour and surface plots (Figures 4.7-4.8). Contour and surface plots were calibrated to a color map with intensities ranging from 0 (blue) to 1 (dark red) representing the range of grayscale intensities (0-255). Gated image data is collected immediately post injection; therefore, nearly all contrast media is retained within the blood. The highest contrast intensities (red) represent where blood is within the ventricular chambers via where the highest contrast enhancement from the particles resides whereas lower contrast intensities (blue) reveals where the myocardial tissue is, largely devoid of contrast media. Day 9 ventricular heart chambers (Figure 4.7) reveal complex differences between systole and diastole in the right and ventricular chambers. Specifically, the right ventricle reveals circumferential orientation of the myocardial architecture around the apical-basal axis of the heart from the banding between the high intensity and low intensity information

(Figure 4.7B). Furthermore, a majority of the high intensity information is clustered around the center of the chamber, showing that remaining blood within the chamber is in the center of the lumen. In contrast, the right ventricle in diastole has a large amount of high intensity information that is clustered through the center and around the side of the chamber wall, representing the dilated chamber prior to contraction (Figure 4.7E). In addition, the observable change in chamber shape is captured through the segmented images with a contracted chamber (Figure 4.7B) capturing the somewhat traditional “crescent” shape of the chamber with the extension of myocardium continuing towards the pulmonary side of the outflow tract and the fully relaxed chamber with an elongated shape and loss of defined myocardium leading to the outflow tract (Figure 4.7E).

Observations of the day 9 left ventricle reveal specific differences between systole and diastole. As was seen in the right ventricle, the highest intensity information is found in the center of the chamber during contraction (Figure 4.7C) and pattern information reveals orientation of the myocardial architecture in the longitudinal direction with respect to the chamber, oriented on the apical-basal axis of the heart (Figure 4.7B). The distinctive differences in shape between the left and right ventricular chambers during systole are apparent (Figure 4.7B-C). During diastole, the left ventricle is dilated with loss of the tapering of the chamber apex (Figure 4.7F). Furthermore, the high intensity information is found around the edge of the chamber similar to the right ventricular chamber during diastole.

Identical analysis for day 11 embryonic hearts (Figure 4.8) reveals parallel information to the day 9 hearts but features are becoming more magnified with the older hearts. The right ventricular chambers during systole show that high intensity information from the contrast media resides in the center of the chamber (Figure 4.8B). The level of intensity remaining in the chamber during systole is low, with values only reaching 0.5 based on the color map (Figure 4.8B). Circumferential patterns are loosely maintained in the right ventricular chamber oriented with the apical-basal axis of the heart (Figure 4.8B). A dramatic shift in right ventricular shape is observed with a concentration of high intensity blood information at the apex of the ventricle (Figure 4.8E). Similarly to the right ventricle, the left shows minimal high intensity information within the center of the chamber suggesting a nearly complete emptying of the chamber upon contraction (Figure 4.8C). Longitudinal banding in the chamber reveals orientation of the myocardial morphology along the apical-basal axis (Figure 4.8C). Shape fidelity is roughly maintained between systole and diastole (Figure 4.8C, F) with a similar but dilated chamber shape observed during diastole (Figure 4.8F). As was seen in the right ventricle, the highest intensity information is clustered at the apex of the ventricle with color map intensity levels reaching 0.8, in stark contrast to the intensities during systole reaching levels not exceeding 0.5 (Figure 4.8C,F).

Trabecular density was established through the built in stereology analysis package in MicroView. Regions of interest were sampled at the apical, middle, and basal spatial locations within the right and left ventricles of day 9 and day 11 embryos at peak systole and peak diastole. Using a measured contrast intensity threshold within each region on interest, the stereology measurements were made establishing relative trabecular

density (Figure 4.9). Since ultimately the trabecular analysis is influenced based on a contrast intensity, the threshold used was the level of blood (high attenuation) within the ventricle; therefore, the density measurements recorded represent the complementary values to that of that trabeculae or the relative volumetric amount of blood present or the absence of trabecular structure. To reduce inherent differences within heart size, the ratio of systole to diastole is reported with a value of 1 representing equal trabecular density between systole and diastole (Figure 4.9). All values are less than 1 with the exception of the apical region of the right ventricle meaning measured systolic blood quantities within the region of interest were lower than that of diastolic which suggests

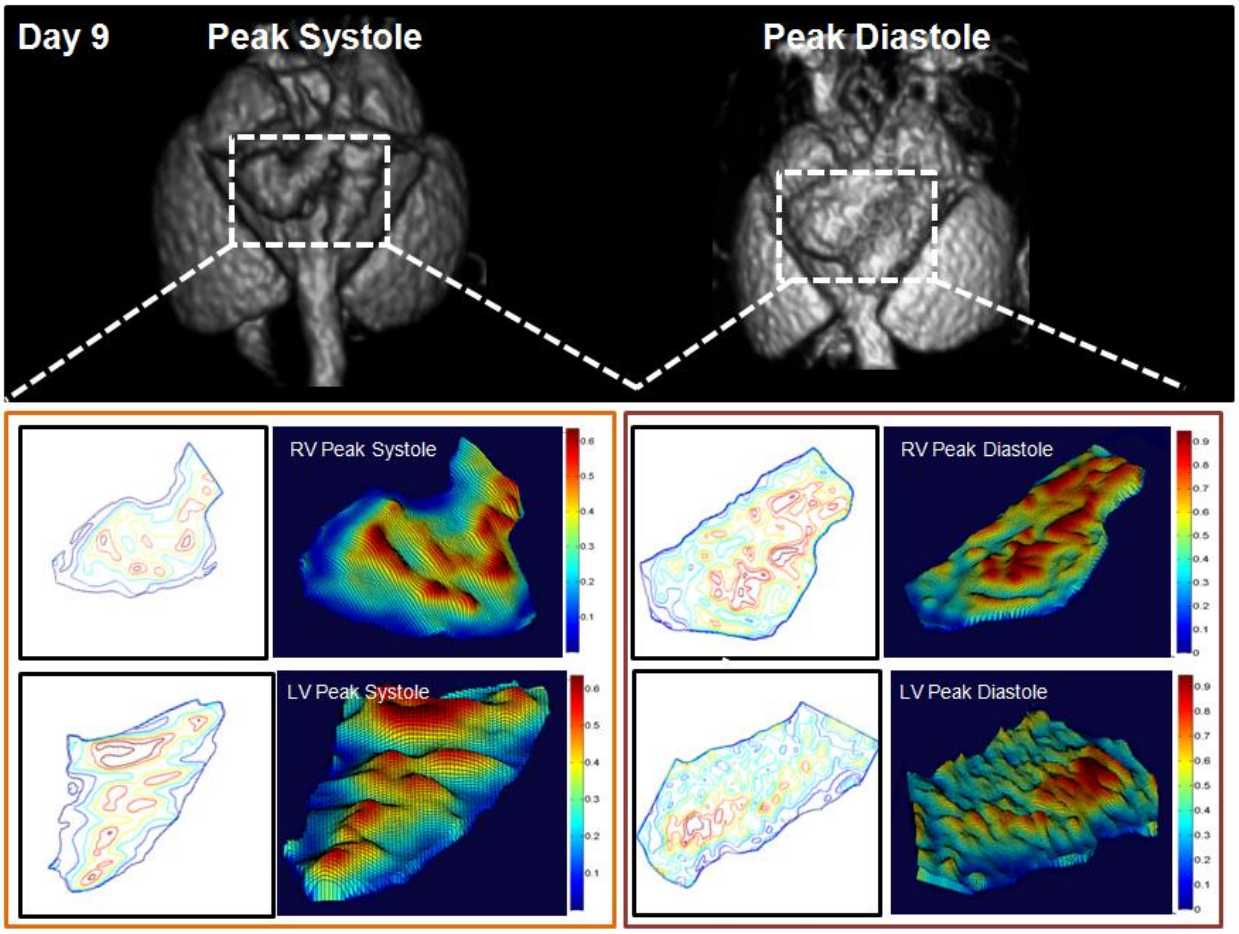

Figure 4.7 - Day 9 contour and surface mapping of the right and left ventricles. (A-C) peak systolic changes and (D-F) peak diastolic changes

that the bulk trabecular density across nearly all regions of the embryonic heart is higher at systole when the heart is fully contracted and the ventricular volumes are smallest (Figure 4.9).

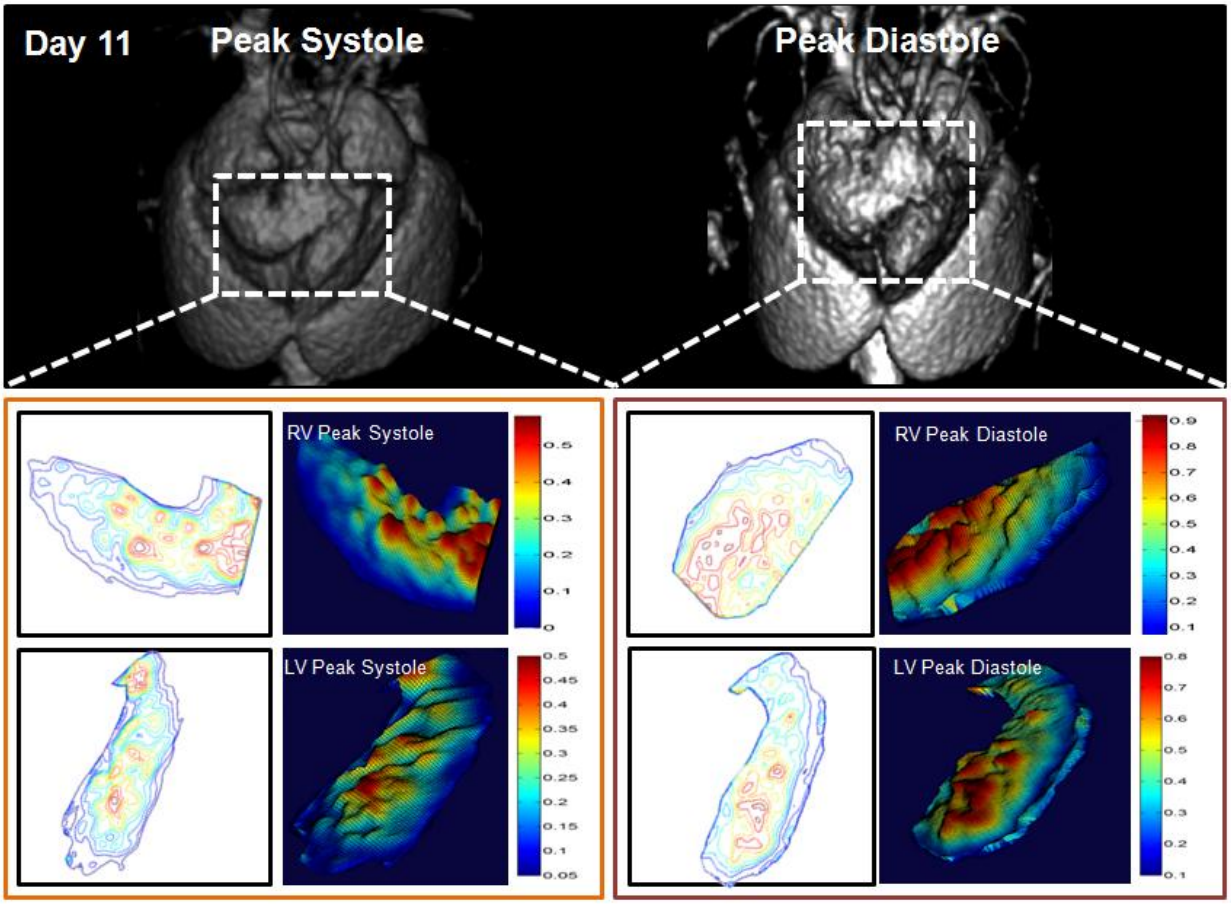

Figure 4.8 - Day 11 contour and surface mapping of the right and left ventricles. (A-C) peak systolic changes and (D-F) peak diastolic changes

Discussion

We established a means for prospectively gating image acquisition of the embryonic heart during mid-late stages of development through direct visualization via a fiber optic bundle and white light illumination. Through tracking of peak systole and peak diastole

from a user defined sampling, we found the peak volumetric changes for day 9 and day 11 chick embryos along with the ejection fractions for both ventricles at each embryonic age assessed. We established baseline metrics of dynamic changes during the cardiac cycle and functional consequences of normal cardiogenesis. Furthermore, we establish a means for visualization of dynamic morphology changes within the ventricular lumen through contour and surface mapping revealing striking ventricular shape changes and myocardial architecture between peak systole and peak diastole. Bulk trabecular density analysis establishes increased density during peak systole almost exclusively across the entire heart along the apical-basal axis through defining a blood attenuation threshold. The technology advancements and quantification of cardiac dynamics presented here are much needed contributions to the understanding of normal tissue assembly and give opportunity for future work in diseased animal models.

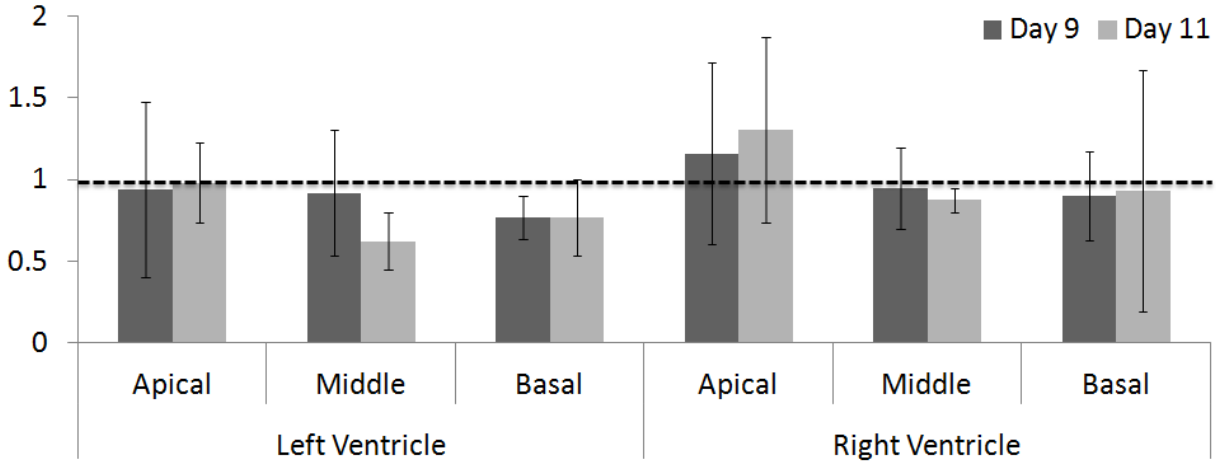

Figure 4.9 - Relative bulk trabecular density based on volumetric blood changes. A ratio of trabecular density changes based on a comparison between peak systole and peak diastole is given for day 9 and day 11 chick embryos along the apical-basal axis with three measurement points. Values below 1 represent lower volumetric blood measurements indicating an increase in bulk trabecular density

Having timed specification for image acquisition – gating – reduces motion artifacts and results in clearer image datasets. Prospective image gating is performed during the image scan, timing acquisition with a periodic signal, commonly the heart beat (Gregg & Butcher, 2012). Prospectively gated images are “phase locked” meaning all captured images of the heart are taken with the same conformation (peak systole, peak diastole, ect.), specified by the user. An electrocardiogram is not available for the embryo and gating is typically acquired off of movement from the heart or large blood vessel achieved optically (Chan et al., 2009; Taylor et al., 2011). While many gating approaches have been using for imaging the developing heart in early stage embryos with optical imaging techniques (Liebling et al., 2014; Ohn, Tsai, & Liebling, 2009; Yoo et al., 2011), extension of gated image datasets to mid-late stage development was not possible. Furthermore, the enclosed imaging bore and lack of access for the user during the imaging scan guided the design considerations made for the presented system.

MicroCT has been used widely in embryological imaging for the past 15 years for characterizing tortuous anatomy with the high spatial and temporal resolutions required(Hogers et al., 1999). Exogenous soft tissue contrast is critical for producing high quality images for discerning relevant quantitative information. Contrast agents are typically comprised of high atomic weight molecules nearly all of which are toxic. Recently we published several manuscripts establishing the safety of microCT imaging on embryos for mid-late stages of development and non-lethal contrast media (Henning, Jiang, Yalcin, & Butcher, 2011, Gregg et al 2016 accepted, Gregg et al 2016 in

preparation). We found that the free molecule Visipaque (VP, GE Healthcare Live microCT) was non-toxic delivered in volumes less than 20% blood volume and produced high levels of contrast enhancement immediately post injection but VP quickly extravasated out of the embryonic structures becoming ineffective for long term studies. In contrast, we have found that a 110nm metallic nanoparticle contrast media (EXTN, Miltenyi Biotec) has increased biodistribution and residence time as compared to free molecule contrast. These particles have been extended for long term imaging studies during mid-late stages comparable to the period of morphogenesis presented here (Gregg et al 2016 in preparation). The slow perfusion of the 110nm particles into the tissue makes it an ideal candidate for dynamic heart analysis, enabling segmentation of ventricular lumen and myocardium via bulk particle contrast enhancement. Up to 2 hours post injection, metallic nanoparticle contrast remains almost exclusively in the blood producing high contrast in vascularized structures. The disparity in contrast between vascularized structures and surrounding mesenchyme reveals a unique ability for determining changing dynamics and morphology within the tissue. In this study, we capitalized on this phenomenon by mapping the ventricular chamber. Areas of high intensity represent where contrast media is present in blood (ventricular lumen) but low contrast reflects where myocardial tissue resides (ie. trabeculae). Building upon measureable attenuation differences, measured trabeculae density is revealed to be highest at peak systole.

Overall volumes measured in this study correlated to previously imaged fixed tissue specimens, perfused with a casting polymer (MicroFil) (Butcher et al., 2007). In

particular we informed our peak diastole volumes from perfused fixed tissue specimens a landmark for agreement between our gating technology and previously measured anatomy in the literature. We found overall increases in the dynamic volumetric change within the cardiac cycle between days 9-11 of development which correlated to an increased ejection fraction. Interestingly, the right ventricle consistently had a high dynamic volume change and ejection fraction but overall increasing trends remained consistent between the left and right sides of the heart. Additionally, we demonstrated that 3D volumetric reconstructions from gated image scans clearly shows differences in heart conformation between peak systole and peak diastole whereas non-gated control images are ambiguous on heart conformation and of an overall lower quality demonstrating the need for gated image datasets for analysis of cardiogenesis. Future analysis and technological improvements should focus on integrating gated image acquisition with more robust scan protocols including increases in spatial resolution and number of total projections collected with a single rotation of the gantry. In this study, we measured bulk trabecular density because identification of individual trabeculae is below the resolution capabilities of the scan protocol used. Futhermore, analysis of small regions of interest is increasingly difficult with the resolutions used and relatively few number of image projections; therefore, higher amounts of error are to be expected. If improvements can be made in the spatial resolution and number of projections acquired all while maintaining the viability of the embryo, the potential for more and higher sensitivity quantitative information will be greatly increased.

Dynamic image analysis is critical for understanding normal morphodynamics and altered scenarios. Furthermore, with dynamic heart imaging in the literature exclusively confined to early stage heart development (Liebling et al., 2014; Mickoleit et al., 2014; Squirrell et al., 1999; Yoo et al., 2011), changes in ventricular shape, morphology, and myocardial architecture dynamics has been impossible to discern for mid-late stages of development where high resolution imaging studies have been confined to fixed tissue specimens (Butcher et al., 2007; Kim et al., 2011; Sedmera et al., 1997). While fixed tissue specimens of mid-late stage heart imaging have informed changes in morphology, elucidating morphodynamics of lumen and myocardial architecture are essential for revealing functional parameters in cardiogenesis. Implementation of altered heart anatomy through well established microsurgical perturbations is a critical next step for gated heart analysis. Left atrial ligation (LAL) surgeries have been well documented in embryological cardiac research (Gould et al., 2015; Hogers et al., 1999) and represent a severe clinically relevant defect reminiscent of hypoplastic left heart syndrome. LALs critically alter myocardial patterning and left ventricular formation resulting in impaired left heart function and overall blood supply deficiency. Coupling live imaging methods described here with gene/protein analysis can provide a powerful multi-scale understanding of the molecular signaling inputs that manifest themselves in a morphological structure-function relationship that is clinically relevant. Surgical interventions have to potential to elucidate the extent of functional loss correlated to genetic and protein level changes and can inspire targeted therapeutic pathways for biological intervention to restore functionality either partially or fully. Implemented in a diseased model, dynamic heart analysis reveals the functional consequences of

abnormal tissue morphogenesis and could possibly underpin the tissue patterning changes that are required for this defect to occur. In conclusion, understanding dynamic cardiac function is imperative for revealing normal morphodynamics and tissue assembly through uncovering the functional outcomes of normal and abnormal development.

References

Aillon, K. L., Xie, Y., El-Gendy, N., Berkland, C. J., & Forrest, M. L. (2009). Effects of nanomaterial physicochemical properties on in vivo toxicity. *Advanced Drug Delivery Reviews*, *61*(6), 457–466. http://doi.org/10.1016/j.addr.2009.03.010

Aleksandrova, A., Czirok, A., Szabo, A., Filla, M. B., Julius, M., Whelan, P. F., … Rongish, B. J. (2013). Convective tissue movements play a major role in avian endocardial morphogenesis, *363*(2), 348–361. http://doi.org/10.1016/j.ydbio.2011.12.036.Convective

Ashton, J. R., Clark, D. P., Moding, E. J., Ghaghada, K., Kirsch, D. G., West, J. L., & Badea, C. T. (2014). Dual-energy micro-CT functional imaging of primary lung cancer in mice using gold and iodine nanoparticle contrast agents: a validation study. *PloS One*, *9*(2), e88129. http://doi.org/10.1371/journal.pone.0088129

Bellairs, R., & Osmond, M. (2014). *Atlas of Chick Development*. *Atlas of Chick Development*. http://doi.org/10.1016/B978-0-12-384951-9.00013-7

Boll, H., Nittka, S., Doyon, F., Neumaier, M., Marx, A., Kramer, M., … Brockmann, M. a. (2011). Micro-CT based experimental liver imaging using a nanoparticulate contrast agent: a longitudinal study in mice. *PloS One*, *6*(9), e25692. http://doi.org/10.1371/journal.pone.0025692

Butcher, J. T., Sedmera, D., Guldberg, R. E., & Markwald, R. R. (2007). Quantitative volumetric analysis of cardiac morphogenesis assessed through micro-computed tomography. *Developmental Dynamics : An Official Publication of the American Association of Anatomists*, *236*(3), 802–9. http://doi.org/10.1002/dvdy.20962

Chakraborty, S., Cheek, J., Sakthivel, B., Aronow, B. J., & Yutzey, K. E. (2008). Shared

gene expression profiles in developing heart valves and osteoblast progenitor cells. *Physiological Genomics*, *35*(1), 75–85. http://doi.org/10.1152/physiolgenomics.90212.2008

Chakraborty, S., Combs, M. D., & Yutzey, K. E. (2010). Transcriptional regulation of heart valve progenitor cells. *Pediatric Cardiology*, *31*(3), 414–21. http://doi.org/10.1007/s00246-009-9616-x

Chan, P. K., Lin, C. C., & Cheng, S. H. (2009). Noninvasive technique for measurement of heartbeat regularity in zebrafish (Danio rerio) embryos. *BMC Biotechnology*, *9*, 11. http://doi.org/10.1186/1472-6750-9-11

Coffin, J. D., & Poole, T. J. (1988). Embryonic vascular development: immunohistochemical identification of the origin and subsequent morphogenesis of the major vessel primordia in quail embryos. *Development (Cambridge, England)*, *102*(4), 735–48. Retrieved from http://www.ncbi.nlm.nih.gov/pubmed/3048971

Cui, C., Filla, M. B., Jones, E. a V, Lansford, R., Cheuvront, T., Al-Roubaie, S., … Little, C. D. (2013). Embryogenesis of the first circulating endothelial cells. *PloS One*, *8*(5), e60841. http://doi.org/10.1371/journal.pone.0060841

Czirók, A., Rongish, B. J., & Little, C. D. (2004). Extracellular matrix dynamics during vertebrate axis formation. *Developmental Biology*, *268*(1), 111–22. http://doi.org/10.1016/j.ydbio.2003.09.040

Darnell, D. K., & Schoenwolf, G. C. (2000). The chick embryo as a model system for analyzing mechanisms of development. *Methods in Molecular Biology (Clifton, N.J.)*, *135*, 25–9. Retrieved from http://www.ncbi.nlm.nih.gov/pubmed/10791301

deAlmeida, A., McQuinn, T., & Sedmera, D. (2007). Increased ventricular preload is

compensated by myocyte proliferation in normal and hypoplastic fetal chick left ventricle. *Circulation Research*, *100*(9), 1363–70. http://doi.org/10.1161/01.RES.0000266606.88463.cb

Degenhardt, K., Wright, A. C., Horng, D., Padmanabhan, A., & Epstein, J. a. (2010). Rapid 3D phenotyping of cardiovascular development in mouse embryos by micro-CT with iodine staining. *Circulation. Cardiovascular Imaging*, *3*(3), 314–22. http://doi.org/10.1161/CIRCIMAGING.109.918482

Diaspro, A., Chirico, G., & Collini, M. (2005). Two-photon fluorescence excitation and related techniques in biological microscopy. *Quarterly Reviews of Biophysics*, *38*(2), 97–166. http://doi.org/10.1017/S0033583505004129

Dickinson, M. E., Simbuerger, E., Zimmermann, B., Waters, C. W., & Fraser, S. E. (2003). Multiphoton excitation spectra in biological samples. *Journal of Biomedical Optics*, *8*(3), 329–38. http://doi.org/10.1117/1.1583734

Edwards, K. A., & Baeumner, A. J. (2007). Synthesis of a liposome incorporated 1-carboxyalkylxanthine-phospholipid conjugate and its recognition by an RNA aptamer. *Talanta*, *71*(1), 365–372. http://doi.org/10.1016/j.talanta.2006.04.031

Eichmann, A., Marcelle, C., Brant, C., Douarin, N. M. Le, De, A., & Gabrielle, B. (1993). Two molecules related to the VEGF receptor are expressed in early endothelial cells during avian embryonic development F //////////// A I, *42*, 33–48.

Goodman, C. M., McCusker, C. D., Yilmaz, T., & Rotello, V. M. (2004). Toxicity of gold nanoparticles functionalized with cationic and anionic side chains. *Bioconjugate Chemistry*, *15*(4), 897–900. http://doi.org/10.1021/bc049951i

Gould, R. A., Yalcin, H. C., MacKay, J. L., Sauls, K., Norris, R., Kumar, S., & Butcher, J.

T. (2015). Cyclic Mechanical Loading Is Essential for Rac1-Mediated Elongation and Remodeling of the Embryonic Mitral Valve. *Current Biology*, *26*(1), 27–37. http://doi.org/10.1016/j.cub.2015.11.033

Graves, J. S., Dunn, B. E., & Brown, S. C. (1986). Embryonic chick allantois: functional isolation and development of sodium transport. *The American Journal of Physiology*, *251*(5 Pt 1), C787–94. Retrieved from http://ajpcell.physiology.org/content/251/5/C787.abstract

Gregg, C. L., & Butcher, J. T. (2012). Quantitative In Vivo Imaging of Embryonic Development: Opportunities and Challenges. *Differentiation*, *84*(1), 149–162. http://doi.org/10.1016/j.diff.2012.05.003.Quantitative

Gregg, C. L., & Butcher, J. T. (2013). Translational paradigms in scientific and clinical imaging of cardiac development. *Birth Defects Research. Part C, Embryo Today : Reviews*, *99*(2), 106–20. http://doi.org/10.1002/bdrc.21034

Gregg, C. L., Recknagel, A. K., & Butcher, J. T. (2015). Micro/Nano-Computed Tomography Technology for Quantitative Dynamic, Multi-scale Imaging of Morphogenesis. *Methods in Molecular Biology (Clifton, N.J.)*, *1189*, 47–61. http://doi.org/10.1007/978-1-4939-1164-6

Henning, A. L., Jiang, M. X., Yalcin, H. C., & Butcher, J. T. (2011). Quantitative three-dimensional imaging of live avian embryonic morphogenesis via micro-computed tomography. *Developmental Dynamics : An Official Publication of the American Association of Anatomists*, *240*(8), 1949–57. http://doi.org/10.1002/dvdy.22694

Hoffman, J. I. E., & Kaplan, S. (2002). The incidence of congenital heart disease. *Journal of the American College of Cardiology*, *39*(12), 1890–900. Retrieved from

http://www.ncbi.nlm.nih.gov/pubmed/12084585

Hogers, B., DeRuiter, M. C., Gittenberger-de Groot, a C., & Poelmann, R. E. (1999). Extraembryonic venous obstructions lead to cardiovascular malformations and can be embryolethal. *Cardiovascular Research*, *41*(1), 87–99. Retrieved from http://www.ncbi.nlm.nih.gov/pubmed/10325956

Jia, H. Y., Liu, Y., Zhang, X. J., Han, L., Du, L. B., Tian, Q., & Xu, Y. C. (2009). Potential oxidative stress of gold nanoparticles by induced-NO releasing in serum. *Journal of the American Chemical Society*, *131*(1), 40–41. http://doi.org/10.1021/ja808033w

Johnson, J. T., Hansen, M. S., Wu, I., Healy, L. J., Johnson, C. R., Jones, G. M., … Keller, C. (2006). Virtual histology of transgenic mouse embryos for high-throughput phenotyping. *PLoS Genetics*, *2*(4), e61. http://doi.org/10.1371/journal.pgen.0020061

Kim, J. S., Min, J., Recknagel, A. K., Riccio, M., & Butcher, J. T. (2011). Quantitative Three-Dimensional Analysis of Embryonic Chick Morphogenesis Via Microcomputed Tomography. *The Anatomical Record: Advances in Integrative Anatomy and Evolutionary Biology*, *294*(1), 1–10. http://doi.org/10.1002/ar.21276

Kruzynska-frejtag, A., Machnicki, M., Rogers, R., Markwald, R. R., & Conway, S. J. (2001). Periostin (an osteoblast-speci ® c factor) is expressed within the embryonic mouse heart during valve formation, *103*, 183–188.

Lamers, W. H. (2002). Cardiac Septation: A Late Contribution of the Embryonic Primary Myocardium to Heart Morphogenesis. *Circulation Research*, *91*(2), 93–103. http://doi.org/10.1161/01.RES.0000027135.63141.89

Le Douarin, N. M. (2008). Developmental patterning deciphered in avian chimeras.

Development, Growth & Differentiation, *50 Suppl 1*(December 2007), S11–28. http://doi.org/10.1111/j.1440-169X.2008.00989.x

Lee, C.-L., Min, H., Befera, N., Clark, D., Qi, Y., Das, S., … Kirsch, D. G. (2014). Assessing Cardiac Injury in Mice wit hDual Energy-microCT, 4D-microCT and microSPECT Imaging Following Partial-Heart Irradiation. *Int. J Radiat Oncol Biol Phys*, *88*(3), 686–693. http://doi.org/10.1016/j.ijrobp.2013.11.238.Assessing

Liebling, M., Forouhar, A. S., Gharib, M., Fraser, S. E., & Dickinson, M. E. (2014). Four-dimensional cardiac imaging in living embryos via postacquisition synchronization of nongated slice sequences. *Journal of Biomedical Optics*, *10*(5), 054001. http://doi.org/10.1117/1.2061567

Liu, A., Wang, R., Thornburg, K. L., & Rugonyi, S. (2014). Efficient postacquisition synchronization of 4-D nongated cardiac images obtained from optical coherence tomography: application to 4-D reconstruction of the chick embryonic heart. *Journal of Biomedical Optics*, *14*(4), 044020. http://doi.org/10.1117/1.3184462

Lucitti, J. L., Jones, E. a V, Huang, C., Chen, J., Fraser, S. E., & Dickinson, M. E. (2007). Vascular remodeling of the mouse yolk sac requires hemodynamic force. *Development (Cambridge, England)*, *134*(18), 3317–26. http://doi.org/10.1242/dev.02883

Manner, J. (2000). Cardiac Looping in the Chick Embryo : A Morphological Review With Special Reference to Terminological and Biomechanical, *262*(March), 248–262.

Melancon, M. P., Zhou, M., Zhang, R., Xiong, C., Allen, P., Wen, X., … Li, C. (2014). Selective uptake and imaging of aptamer- and antibody-conjugated hollow nanospheres targeted to epidermal growth factor receptors overexpressed in head

and neck cancer. *ACS Nano*, *8*(5), 4530–8. http://doi.org/10.1021/nn406632u

Metscher, B. D. (2009). MicroCT for developmental biology: a versatile tool for high-contrast 3D imaging at histological resolutions. *Developmental Dynamics : An Official Publication of the American Association of Anatomists*, *238*(3), 632–40. http://doi.org/10.1002/dvdy.21857

Metscher, B. D., & Müller, G. B. (2011). MicroCT for molecular imaging: quantitative visualization of complete three-dimensional distributions of gene products in embryonic limbs. *Developmental Dynamics : An Official Publication of the American Association of Anatomists*, *240*(10), 2301–8. http://doi.org/10.1002/dvdy.22733

Mickoleit, M., Schmid, B., Weber, M., Fahrbach, F. O., Hombach, S., Reischauer, S., & Huisken, J. (2014). High-resolution reconstruction of the beating zebrafish heart. *Nature Methods*, (July), 1–6. http://doi.org/10.1038/nmeth.3037

Nakamura, H., & Funahashi, J. (2001). Introduction of DNA into chick embryos by in ovo electroporation. *Methods (San Diego, Calif.)*, *24*(1), 43–8. http://doi.org/10.1006/meth.2001.1155

Nebuloni, L., Kuhn, G. a, & Müller, R. (2013). A comparative analysis of water-soluble and blood-pool contrast agents for in vivo vascular imaging with micro-CT. *Academic Radiology*, *20*(10), 1247–55. http://doi.org/10.1016/j.acra.2013.06.003

Ohn, J., Tsai, H.-J., & Liebling, M. (2009). Joint dynamic imaging of morphogenesis and function in the developing heart. *Organogenesis*, *5*(4), 248–55. Retrieved from http://www.pubmedcentral.nih.gov/articlerender.fcgi?artid=2878754&tool=pmcentrez&rendertype=abstract

Olson, E. N., & Nes, V. (2006). Gene Regulatory Networks Evolution and Development

in the of the Heart. *Science*, *313*(5795), 1922–1927.

Pan, Y., Leifert, A., Ruau, D., Neuss, S., Bornemann, J., Schmid, G., … Jahnen-Dechent, W. (2009). Gold Nanoparticles of Diameter 1.4 nm Trigger Necrosis by Oxidative Stress and Mitochondrial Damage. *Small*, *5*(18), 2067–2076. http://doi.org/10.1002/smll.200900466

Patten, B. M., Akd, K., & Barry, A. (n.d.). VALVULAR ACTION IN T H E EMBRYONIC.

Person, A. D., Klewer, S. E., & Runyan, R. B. (2005). Cell Biology of Cardiac Cushion Development. *International Review Cytology*, *243*.

Pierpont, M. E., Basson, C. T., Benson, D. W., Gelb, B. D., Giglia, T. M., Goldmuntz, E., … Webb, C. L. (2007). Genetic basis for congenital heart defects: current knowledge: a scientific statement from the American Heart Association Congenital Cardiac Defects Committee, Council on Cardiovascular Disease in the Young: endorsed by the American Academy of Pediatrics. *Circulation*, *115*(23), 3015–38. http://doi.org/10.1161/CIRCULATIONAHA.106.183056

Risau, W., & Flamme, I. (1995). V asculogenesis. *Annu. Rev. Cell Dev. Biol.*, *11*, 73–91.

Roger, V. L., Go, A. S., Lloyd-Jones, D. M., Adams, R. J., Berry, J. D., Brown, T. M., … Wylie-Rosett, J. (2010). Heart Disease and Stroke Statistics--2011 Update: A Report From the American Heart Association. *Circulation*, 1–193. http://doi.org/10.1161/CIR.0b013e3182009701

Roy, S., Hirano, A., Kochen, J. A., & Zimmerman, H. M. (1974). The fine structure of cerebral blood vessels in chick embryo. *Acta Neuropathologica*, *30*(4), 277–285.

Sabin, F. (1917). Origin and Development of the Primitive Vessels of the Chick and of the Pig. *Carnegie Institution of Washington*, *6*(226), 64.

Scheller, B., Hennen, B., Thünenkötter, T., Mrowietz, C., Markwirth, T., Schieffer, H., & Jung, F. (1999). Effect of X-ray contrast media on blood flow properties after coronary angiography. *Thrombosis Research*, *96*(4), 253–60. Retrieved from http://www.ncbi.nlm.nih.gov/pubmed/10593427

Sedmera, D., Pexieder, T., Norman, H. U., & Clark, E. B. (1997). Developmental changes in the myocardial architecture of the chick. *Anatomical Record*, *248*(3), 421–432. http://doi.org/10.1002/(SICI)1097-0185(199707)248:3<421::AID-AR15>3.0.CO;2-R

Sedmera, D., Pexieder, T., Rychterova, V., Hu, N., & Clark, E. B. (1999). Remodeling of Chick Embryonic Ventricular Myoarchitecture Under Experimentally Changed Loading Conditions, *252*(March 1998), 238–252.

Shen, Y., Leatherbury, L., Rosenthal, J., Yu, Q., Pappas, M. a, Wessels, a, … Lo, C. W. (2005). Cardiovascular phenotyping of fetal mice by noninvasive high-frequency ultrasound facilitates recovery of ENU-induced mutations causing congenital cardiac and extracardiac defects. *Physiological Genomics*, *24*(1), 23–36. http://doi.org/10.1152/physiolgenomics.00129.2005

Singh, A., Agarwal, R., Diaz-Ruiz, C. a, Willett, N. J., Wang, P., Lee, L. A., … García, A. J. (2014). Nanoengineered particles for enhanced intra-articular retention and delivery of proteins. *Advanced Healthcare Materials*, *3*(10), 1562–7, 1525. http://doi.org/10.1002/adhm.201400051

Squirrell, J. M., Wokosin, D. L., White, J. G., & Bavister, B. D. (1999). Long-term two-photon fluorescence imaging of mammalian embryos without compromising viability. *Nature Biotechnology*, *17*(8), 763–7. http://doi.org/10.1038/11698

Supatto, W., Débarre, D., Moulia, B., Brouzés, E., Martin, J.-L., Farge, E., & Beaurepaire, E. (2005). In vivo modulation of morphogenetic movements in Drosophila embryos with femtosecond laser pulses. *Proceedings of the National Academy of Sciences of the United States of America*, *102*(4), 1047–52. http://doi.org/10.1073/pnas.0405316102

Supatto, W., Mcmahon, A., Fraser, S. E., & Stathopoulos, A. (2009). Quantitative imaging of collective cell migration during Drosophila gastrulation: multiphoton microscopy and computational analysis, *4*(10), 1397–1412. http://doi.org/10.1038/nprot.2009.130.Quantitative

Taylor, J. M., Saunter, C. D., Love, G. D., Girkin, J. M., Henderson, D. J., & Chaudhry, B. (2011). Real-time optical gating for three-dimensional beating heart imaging. *Journal of Biomedical Optics*, *16*(11), 116021. http://doi.org/10.1117/1.3652892

Tkatchenko, T. V, Moreno-Rodriguez, R. a, Conway, S. J., Molkentin, J. D., Markwald, R. R., & Tkatchenko, A. V. (2009). Lack of periostin leads to suppression of Notch1 signaling and calcific aortic valve disease. *Physiological Genomics*, *39*(3), 160–8. http://doi.org/10.1152/physiolgenomics.00078.2009

Turner, M., Golovko, V. B., Vaughan, O. P. H., Abdulkin, P., Berenguer-Murcia, A., Tikhov, M. S., … Lambert, R. M. (2008). Selective oxidation with dioxygen by gold nanoparticle catalysts derived from 55-atom clusters. *Nature*, *454*(7207), 981–983. http://doi.org/10.1038/nature07194

Wen, X., Wu, Q. P., Lu, Y., Fan, Z., Charnsangavej, C., Wallace, S., … Li, C. (2001). Poly(ethylene glycol)-conjugated anti-EGF receptor antibody C225 with radiometal chelator attached to the termini of polymer chains. *Bioconjugate Chemistry*, *12*(4),

545–53. Retrieved from http://www.ncbi.nlm.nih.gov/pubmed/11459459

Wessels, A., & Sedmera, D. (2003). Developmental anatomy of the heart: a tale of mice and man. *Physiological Genomics*, *15*(3), 165–76. http://doi.org/10.1152/physiolgenomics.00033.2003

Wilson, J. G., Roth, C. B., & Warkany, J. (1953). An analysis of the syndrome of malformations induced by maternal vitamin A deficiency. Effects of restoration of vitamin A at various times during gestation. *The American Journal of Anatomy*, *92*(2), 189–217. http://doi.org/10.1002/aja.1000920202

Xin, M., Olson, E. N., & Bassel-duby, R. (2013). Mending broken hearts: cardiac development as a basis for adult heart regeneration and repair. *Nature Reviews. Molecular Cell Biology*, *14*(8), 529–541. http://doi.org/10.1038/nrm3619.Mending

Yalcin, H. C., Shekhar, A., McQuinn, T. C., & Butcher, J. T. (2011). Hemodynamic patterning of the avian atrioventricular valve. *Developmental Dynamics : An Official Publication of the American Association of Anatomists*, *240*(1), 23–35. http://doi.org/10.1002/dvdy.22512

Yang, Q., Khoury, M. J., & Mannino, D. (1997). Trends and patterns of mortality associated with birth defects and genetic diseases in the United States, 1979-1992: an analysis of multiple-cause mortality data. *Genetic Epidemiology*, *14*(5), 493–505. http://doi.org/10.1002/(SICI)1098-2272(1997)14:5<493::AID-GEPI4>3.0.CO;2-2

Yoo, J., Larina, I. V, Larin, K. V, Dickinson, M. E., & Liebling, M. (2011). Increasing the field-of-view of dynamic cardiac OCT via post-acquisition mosaicing without affecting frame-rate or spatial resolution. *Biomedical Optics Express*, *2*(9), 2614–

22. http://doi.org/10.1364/BOE.2.002614

Yu, B., Mao, Y., Bai, L., Herman, S. E. M., Wang, X., Ramanunni, A., … Muthusamy, N. (2015). Targeted nanoparticle delivery overcomes off-target immunostimulatory effects of oligonucleotides and improves therapeutic efficacy in chronic lymphocytic leukemia, *121*(1), 136–148. http://doi.org/10.1182/blood-2012-01-407742.

Yu, Q., Shen, Y., Chatterjee, B., Siegfried, B. H., Leatherbury, L., Rosenthal, J., … Lo, C. W. (2004). ENU induced mutations causing congenital cardiovascular anomalies. *Development (Cambridge, England)*, *131*(24), 6211–23. http://doi.org/10.1242/dev.01543

Zamir, E. a, Czirók, A., Cui, C., Little, C. D., & Rongish, B. J. (2006). Mesodermal cell displacements during avian gastrulation are due to both individual cell-autonomous and convective tissue movements. *Proceedings of the National Academy of Sciences of the United States of America*, *103*(52), 19806–11. http://doi.org/10.1073/pnas.0606100103

Zarschler, K., Prapainop, K., Mahon, E., Rocks, L., Bramini, M., Kelly, P. M., … Dawson, K. a. (2014). Diagnostic nanoparticle targeting of the EGF-receptor in complex biological conditions using single-domain antibodies. *Nanoscale*, *6*(11), 6046–56. http://doi.org/10.1039/c4nr00595c

Zipfel, W. R., Williams, R. M., & Webb, W. W. (2003). Nonlinear magic: multiphoton microscopy in the biosciences. *Nature Biotechnology*, *21*(11), 1369–1377. http://doi.org/10.1038/nbt899

CHAPTER 5

CONCLUSIONS AND FUTURE DIRECTIONS

5.1 Conclusions

Embryonic development is a dynamic three dimensional process comprised of the growth, differentiation, and organization of pluripotent progenitor cell populations into complex and specialized tissues. Having a clear understanding of normal tissue assembly is critical for being able to parse out contributing factors in the event of congenital malformation. Approximately 3% of live births result in a congenital malformation, with 1% of those attributed to congenital heart defects(Gregg & Butcher, 2013). Few congenital defects can be traced to a specific genetic origin and instead are thought to arise from a cacophony of genome wide mis-expression from either environmental or biochemical perturbations. Furthermore, a majority of clinically relevant congenital malformations arise during the mid-late stages of development, beyond the scope of nearly all live embryonic imaging studies to date (Roger et al., 2010). Nearly all live embryonic imaging studies have focused on the earliest stages of development primarily comprised of axis patterning, gastrulation, and the onset of heart beating but defects that arise during this period are nearly always lethal (Cui et al., 2013; Czirók, Rongish, & Little, 2004; Zamir, Czirók, Cui, Little, & Rongish, 2006). Defects arising during the mid-late stages are far less lethal during gestation but contribute to a wide array of congenital defects with ranging severities. Understanding complex, three dimensional tissue assembly during these stages contributes to the

multi-scale developmental landscape that scientists and engineers are trying to piece together.

Three dimensional imaging strategies for live embryonic development have nearly always been confined to traditional optical means. Optical imaging techniques have been the most widely used tool for visualization of live development but are limited for mid-late stage development due to the dense and light scattering nature of the tissue restricting light penetration into samples to 2mm at best (Diaspro, Chirico, & Collini, 2005; Dickinson, Simbuerger, Zimmermann, Waters, & Fraser, 2003; Squirrell, Wokosin, White, & Bavister, 1999; Supatto et al., 2005; Supatto, Mcmahon, Fraser, & Stathopoulos, 2009). In some instances, thin tissue sections are imaged sequentially and then interpolated into a 3D volume but this method suffers from registration artifacts between planes and is particularly difficult to resolve highly tortuous anatomy. MicroCT imaging has been used widely for fixed embryonic specimens soaked in high atomic weight contrast media (Butcher, Sedmera, Guldberg, & Markwald, 2007; Kim, Min, Recknagel, Riccio, & Butcher, 2011). Three dimensional, high resolution anatomical data gained from these experiments has been invaluable to the understanding of morphogenesis in vivo and ex vivo but fixed tissue specimens can suffer from artifacts in the fixation process, changing tissue conformations and is limited by not enabling live, longitudinal analysis. Additionally, for analysis using experimental and/or genetic perturbations, inherent sample variability increases for the increased number of samples required to look 1) at multiple stages of development and 2) achieving statistical significance through a high enough sample size. Furthermore, the ability to

examine real time tissue assembly and dynamics is essentially for breaching into higher impact and comprehensive scientific inquiries.

The studies presented in this thesis establish three dimensional high resolution live tissue assembly with microCT imaging ascertaining spatial, temporal, and age related changes that are occurring longitudinally. Furthermore, a prospective image gating systems provided a means for dynamically imaging the embryonic heart for understanding the functional consequences of live tissue assembly and heart maturation demonstrating how and to what degree heart function is varying within the cardiac cycle and how it is increasing over embryonic age. The completion of this work yields important technology development and insights into three dimensional tissue assembly and architectural changes occurring during mid-late stages of development, a time period which was elusive and unable to be captured readily in live samples prior to these studies. The spatial and temporal heterogeneous changes quantified during development are critical landmarks for assessing gross tissue fate decisions, many of which could be altered in an instance of abnormal morphogenetic patterning. A stepwise approach was used to first characterize the appropriate nanoparticle based contrast media and then to move into longitudinal and dynamic imaging analysis. Investigation of three different commercially available metallic nanoparticles yielded that the largest 110nm EXTN particle produced the highest levels of contrast enhancement, with increased particle persistence within the embryonic body as compared to the other particle types (Chapter 2). Using the nanoparticle that outperformed all others from Chapter 2, a longitudinal analysis was conducted establishing heterogeneous patterning

in spatial and temporal tissue assembly (Chapter 3). This also established the inherent tissue changes that are occurring with embryonic age and how material properties via transport of bulk particle movements are not only specific to a particular organ system but are variable throughout a single organ system, suggesting regional material differences increasing with embryonic age (Chapter 3). Lastly, a prospective image gating system was fabricated in house to dynamically image the embryonic heart at specified points within the cardiac cycle, at multiple stages of development (Chapter 4). This has led to the establishment of cyclical changes during the cardiac cycle at a single embryonic age, quantifying peak ventricular volumetric changes and ejection fraction but also functional consequences of tissue assembly through characterization of volumetric change and ejection fraction increases with normal cardiac development (Chapter 4). This chapter discusses the major findings of this thesis and identification of some of the potential future directions for this work to continue.

Chapter 2 evaluates the use of metallic nanoparticle based contrast media for live in vivo microCT imaging of avian development. We demonstrated that nanoparticle toxicity is size dependent with particles <2nm in diameter being embryo lethal. Contrast enhancement, biodistribution, and persistence were related to 1) the material of the particle and 2) with the size of the particle. The 110nm alkaline earth metal particles produced the highest levels of contrast uniformly and persisted in the embryo body for the longest period of time with recorded contrast enhancement up to 24 hours post injection. Furthermore, it was observed that extravasation of particles was size dependent, with fast perfusion of particles out of the vascular structures into the

surrounding tissue by the 1.9nm particles whereas perfusion of the 110nm particles commenced at a significantly slower rate. We suspect this is largely the reason for prolonged visualization of the embryo for at least 24 hours whereas this was not the case for either of the smaller particles which persisted for no longer than 8 hours post injection. Additionally, we quantified relative bulk transport of nanoparticles from the dorsal aorta into the surrounding mesenchyme over 8 hours post injection finding that perfusion increased as a function of distance from the dorsal aorta modeled exponentially. We believe that this represents a “wavefront” of particles with faster rates of perfusion the farther the distance is from the dorsal aorta due to the increasing concentration gradient within the parameter of measurements extending to 0.3mm from the dorsal aorta. Collectively this data supports the idea that metallic nanoparticle based contrast media can be extended to embryonic imaging, particularly larger nanoparticles with have longer persistence within the embryo proper and that the particles can not only be used as a means for tissue visualization for can be as a vehicle for quantifying transport phenomena eluding to bulk changes in material properties.

While we provide some mechanistic understandings of tissue assembly, we delve much more into longitudinal morphogenesis with analysis of days 4-11 chick embryos in Chapter 3. We successfully investigated 1) how nanoparticle based contrast enhancement responds spatially and temporally in older embryos over 24 hours, 2) what can be visualized within the embryos at different times post injection with particles and at different points within development, and 3) how can relative material changes be

measured from bulk particle movement both spatially through the embryo and within specific organ systems. We found that virtual histological sections reveal gross organogenesis and visualization of anatomy was temporally specific with highly vascular structures seen immediately post injection whereas connective tissues were better seen at 24 hours post injection once contrast media had extravasated from the blood vessels into the surrounding tissue. Furthermore, tissue boundary identification was comparable to that seen in a standard histological section but non-boundary signal intensity was better seen in the virtual histology than the traditional thin sections (Bellairs & Osmond, 2014). Having long term visualization of embryos enabled quantification and modeling of growth metrics spanning days 4-11 of development of key organs. In particular, we measured the total volume of the heart, left and right eye, and left and right lung as compared to the total embryo volume. In contrast to volumetric analysis in fixed tissue specimens, these volumes were determined from long term tissue assembly devoid of fixation errors and artifacts from processing of the tissue. We modeled the growth of each organ as a power function and found that growth remained even for organ specific for the time period assessed. Interestingly, we captured the disparity in lung volume between the right and left lung showing parallel of separate growth trajectories with the left lung always remaining smaller than the right lung as what would be expected. We qualitatively observed and quantitatively measured biodistribution and persistence changes in the embryos that were organ specific and age specific. This phenomenon was observed in the virtual histological sections and measured through line scans over 24 hours post injection. More specifically, heterogeneous spatial and temporal particle sequestration was observed

within individual organs themselves with unique patterns observed for different embryonic ages. This was most evident within the heart myocardium. We found that the nanoparticles were homogenously distributed immediately post injection within the heart lumen and then preferentially perfused into the right and left myocardium. The left myocardium consistently had slower perfusion rates up to 0.8mm into the tissue than the right myocardium at day 7 and day 10 embryos. Furthermore, there was a shift in the modeled perfusion between the embryonic ages, showing a relative change in the perfusion rate to being overall slower proportionally. We concluded that this is indicative of the changing microarchitecture and material properties of the myocardium itself. We know from previous literature that the tertiary trabeculae forms between days 7 and 10 of development along with the myocardium orientation and amount of compaction being side specific (Sedmera, Pexieder, Norman, & Clark, 1997). All together, we suggest that the perfusion of the myocardium is reflective of the orientation of the trabeculae and the compaction of the myocardium reflecting that the left side of the heart has more dense myocardium, causing the nanoparticles to become sequestered in the tissue decreasing the effective concentration gradient between the tissue and lumen, resulting in a slower perfusion rate. Taken all together, we found that nanoparticle contrast enhancement is an effective means for quantifying tissue morphogenesis longitudinally with spatial and temporal components to the biodistribution and persistence of the particles. Furthermore, perfusion of bulk particle transport into the tissue is heterogeneous within the tissue, even within specific organ systems. We found that the bulk perfusion of the particles into the myocardium is side

specific, suggesting that the left myocardium is more compact resulting a decrease of perfusion and sequestration of the particles.

In chapter 4, we successfully demonstrated a system for dynamically imaging the embryonic heart. Prospective image gating acquires all images in a single dataset at a specific point within the cardiac cycle. In the case of the embryonic heart, we were unable to use traditional means of gating such as an electrocardiogram signal; therefore, we designed a system that was entirely non-invasive for monitoring the heart rate and triggering off of user defined points within the cycle. We chose direct visualization of the heart or proximal oscillating blood vessel through a fiber optic bundle and light guide connected to a white light LED. The image from the fiber was magnified through a 10x objective and imaged by a camera. Through a user defined sampling area, the heart rate was monitored and the microCT was triggered either off the maximum (peak systole) or minimum (peak diastole). This enabled for datasets to be acquired at the two extremes of the cardiac cycle. We completed for dynamical analysis for the cardiac cycle at a single age and functional analysis completed longitudinally over multiple embryonic ages. We monitored the ejection fraction and the volumetric changes at each time assessed and how they changed over time as well. These results revealed for the first time to our knowledge dynamic, real time data collection and analysis of live embryonic hearts in three dimensions. We determined baseline metrics for normal embryonic development in terms of volumetric changes and ejection fraction between days 9-11 of development, laying the scientific landscape for future studies with both normal and diseased heart samples. Understanding dynamic

cardiac functional has the potential to reveal the functional consequences of normal tissue assembly and abnormal tissue assembly in the case of clinically relevant congenital heart defects.

Overall this work has made significant contributions to the fields of live embryological imaging technology, particularly focused on mid-late stage morphogenesis. More specifically, our nanoparticle based contrast enhancement and long term imaging techniques not only yields three dimensional morphological information about tissue assembly but reveals temporal tissue responses to nanoparticle contrast enhancement suggesting that the contrast media can be a vehicle for elucidating relative bulk material changes within the embryo. With the development of a prospective image gating system, collected datasets for peak systole and peak diastole heart conformations within live embryonic hearts at multiple stages of development demonstrate the capacity of dynamic heart maturation over time. This enabled baseline functional heart metrics to be known, critical for establishing normal heart dynamics and as a comparator for future use of diseased heart models. Our imaging platforms that I presented here open a new realm of scientific real estate to be explored for understanding live, long term tissue assembly and serve for direct, in vivo phenotypic screening and three dimensional analysis for future clinically relevant diseased models.

5.2 Future Directions

Although the work presented in this thesis makes significant contributions in live embryonic imaging technologies and elucidating dynamic tissue changes, it also

presents opportunities for future scientific questions to be explored. Some future directions may include extension of the three dimensional imaging data into 2D and 3D finite element models of the particle transport, in house nanoparticle fabrication for mapping 3D tissue fate decisions, and extension of the presented technologies into diseased animal models for analysis of abnormal morphogenetic processes. While many different research avenues exist, three large and critical areas of need have been identified, a pictorial representation of these areas is given in Figure 5.1

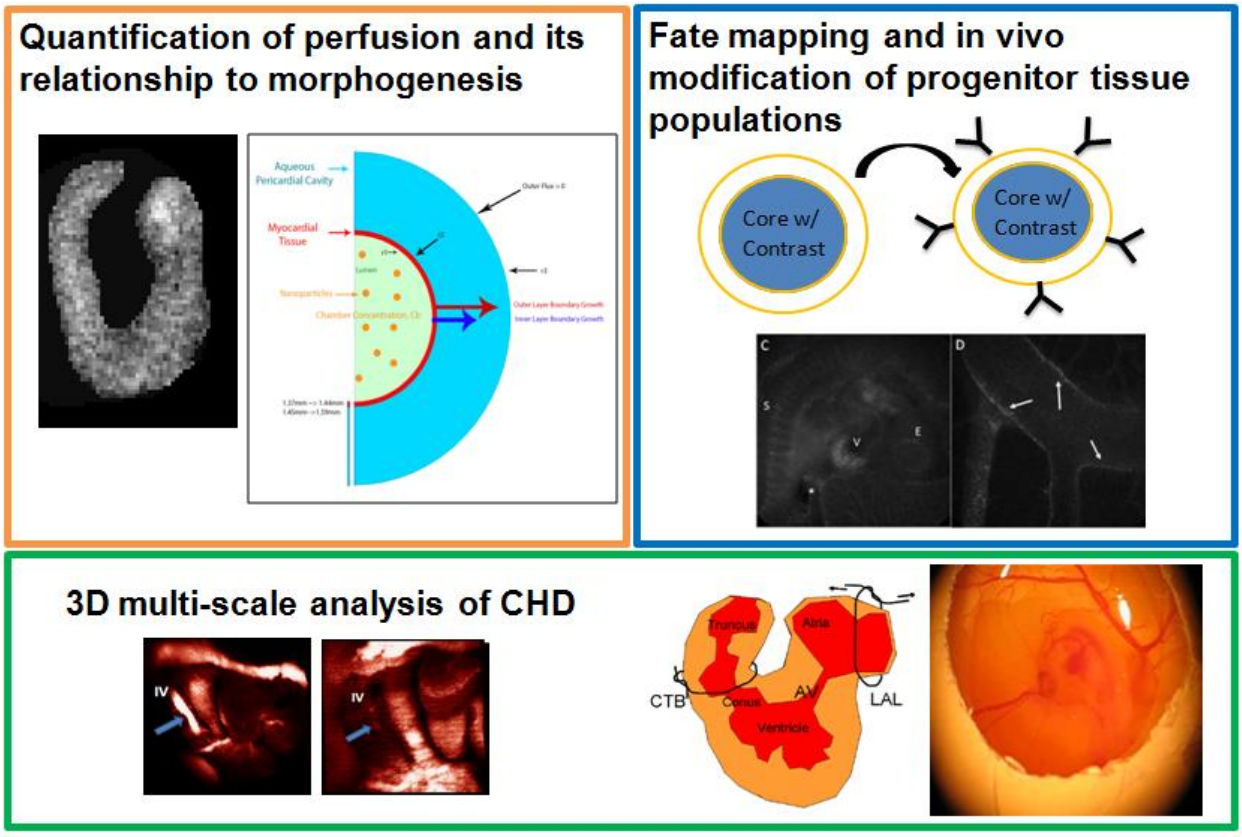

Figure 5.1 - Pictorial representation of key future directions. Three different future directions have been identified for expansion into multi-scale analysis of live morphogenesis using experimental and computational tools.

Quantification of perfusion and its relationship to morphogenesis – mediation of myocardial compaction in comparison to valvulogenesis

Spatial and temporal identification of material properties and heterogeneities are critical for understanding normal tissue changes. Furthermore, ascertaining properties that vary in diseased models can indicate mechanisms for the progression of disease via the deterioration of tissue architecture and overall gross morphology. We found through our analysis that nanoparticle contrast media is not only effective for tissue visualization but can be used for quantification of tissue heterogeneities via bulk particle transport. The type of analysis completed for the presented studies in this thesis were under the assumption that the spatial distribution of particles where the transport was being measured was relatively homogeneous (ie. the left myocardium or right myocardium is spatially the same) and we assumed 1D axisymmetric geometry condensing the sampling into a single line scan. Additionally, we negated pressure terms and converged the system to be quasi-steady state effectively removing temporal components within the model by looking over a single defined time period. The approach presented here was an initial first investigation and showed promising results. For determination of spatial variability even within small areas of tissue, a comprehensive finite element model incorporating known aspects of the fluid, tissue, and particles would enable back calculation of the remaining unknown material properties and how they are spatially varying within selected tissue (Figure 5.2). The advantage to a computational framework is high throughput of simulations from data at multiple stages of development. As we have seen in the work presented here and in multiple other studies (Butcher et al., 2007; Gould et al., 2016; Kim et al., 2011),

embryonic tissues rapidly change and quantitatively understanding these changes can reveal places for abnormal patterning to commence. Using experimental data from the

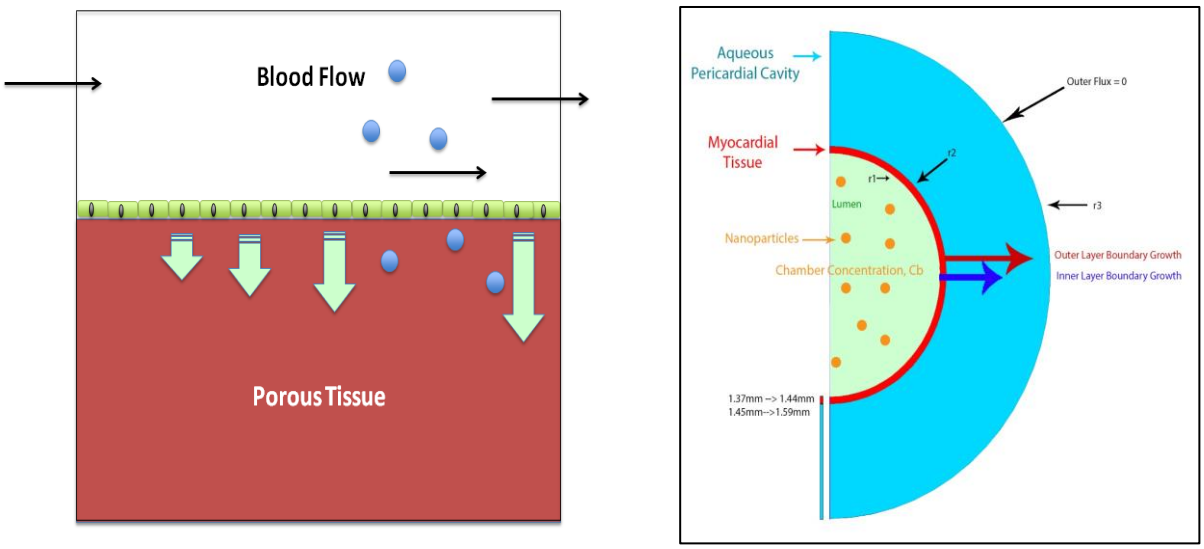

Figure 5.2 - Diagram of 1D and 2D perfusion analysis for finite element modeling of spatial and temporal nanoparticle movements

studies presented here to establish the computational framework needed for quantifying spatial and temporal material properties in the tissue could not only allow for correlation to growth metrics and underlying cellular and molecular changes that are occurring simultaneously but the model could be used as a predictive measure to recapitulate gross changes observed in diseased tissue and indicate where abnormal patterning could theoretically be found. Expansion of experimental and computational tools are described here are of particular importance when parsing out large scale molecular changes during morphogenesis and how they relate to gross tissue assembly. Our lab recently published a paper detailing the heart valve compaction mediating through Rac1 and its importance for proper valvulogenesis (Gould et al., 2016). Valve and myocardial

compaction occur along similar spatial and temporal frameworks leading to an experimental landscape that would begs the question is myocardial compaction also mediated through Raq1 and can alterations in Raq1 through genetic or mechanical perturbations lead to abnormal tissue patterning?

Three dimensional multi-scale analysis of congenital heart defects – effects of altered hemodynamic load on myocardial compaction and fiber orientation

Microsurgical perturbation is a key mechanism for eliciting abnormal tissue patterning in the avian embryo with resultant clinically relevant CHD anatomy. Left atrial ligations (LAL) surgical models have been actively used in research with live in vivo models living to a minimum of day 7 of development and some instances to day 10 of development (Gould et al., 2016) depending on the severity of the defect generated. All studies presented here can be extended to defect model embryos which included longitudinal analysis of CHD progression through the biodistribution and persistence of the contrast media. Extension of the modeled particle transport analysis would elucidate myocardial changes resulting from the ligation surgery. Additionally, rescue surgeries would indicate the recovery mechanisms of the tissue quantifying the dynamic tissue changes and plasticity of the myocardium. We currently have demonstrated successful ligation surgeries (Gould et al., 2016) and recovery surgeries (Figure 5.3) demonstrating disorganized and poor myocardial development through super high resolution images of day 7 chick hearts.

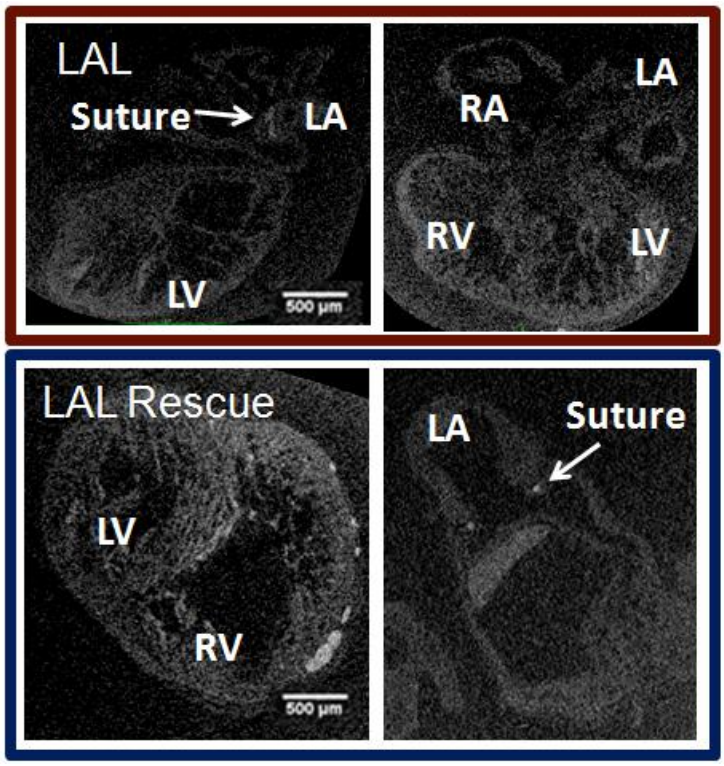

Figure 5.3 - NanoCT images of left atrial ligations and rescues. Impaired lumen and myocardial development is apparent with stunted and altered tissue orientation.

Additionally, extension of dynamic heart imaging through prospective gating will couple myocardial transport analysis with functionality of the myocardial muscle. Severity and extent of CHD generated by the ligation can be correlated to the loss of function measured through volumetric changes and decrease in ejection fraction of the heart. Dynamic analysis combined with bulk particle perfusion will elucidate not only the gross morphological changes as a result from a CHD but may suggest underlying explanations for functional loss such as changing in myocardial compaction resulting in changes perfusion metrics and muscle function. More specifically, we have recently demonstrated that myofibroblastic activity is increased through reduced hemodynamic load via LAL surgeries (Gould et al., 2016). As previously mentioned, valve compaction is mediated through Rac1 and understanding mediation of compaction in the

myocardium as compared to the valve is of great importance for understanding normal cardiogenesis. Furthermore, increases in RhoA and FilGap have been quantified for abnormal valvulogenesis through LAL surgical interventions. Since many CHDs effect more than one aspect of the heart often times valve, myocardial, and lumen abnormalities are coupled, we believe analysis of molecular mediated cellular activity via Rac1, RhoA, and FilGap may reveal connections between valve and myocardial morphogenesis through a mechanical stimulus and returning the hemodynamic load to normal via rescue surgeries can result in a total and/or partial reversal of the abnormalities.

Fate mapping and in vivo modification of progenitor cell populations – biologically targeted nanoparticles for establishing 3D spatial and temporal molecular changes in live embryonic samples

The nanoparticle based contrast media presented here were commercially purchased and incapable of any surface modifications but fabrication of in house particles with controlled surface chemistry would enable targeted imaging through tissue specific biomolecule conjugation. Functionalizing the nanoparticle surface with a specific antibody allows for immune targeting of in the avian embryo. The avian model has few extracellular antibodies to act as a tissue target but one specific antibody that has shown promise in the literature (Eichmann et al., 1993) is the quail endothelial kinase receptor 1 (Quek1). Quek 1 is a vascular endothelial growth factor receptor 2 (VEGFR2) antibody that targets endothelial and endocardial cell lineages. Preliminary data suggest that this marker could be used to target cardiac lineages for monitoring

cell movements and tissue patterning decisions, a mechanism that is critical for understanding tissue assembly and has been paralleled in early stage embryos (Aleksandrova et al., 2013) but has not been extended to live embryos during the mid-late stages (Figure 5.4).

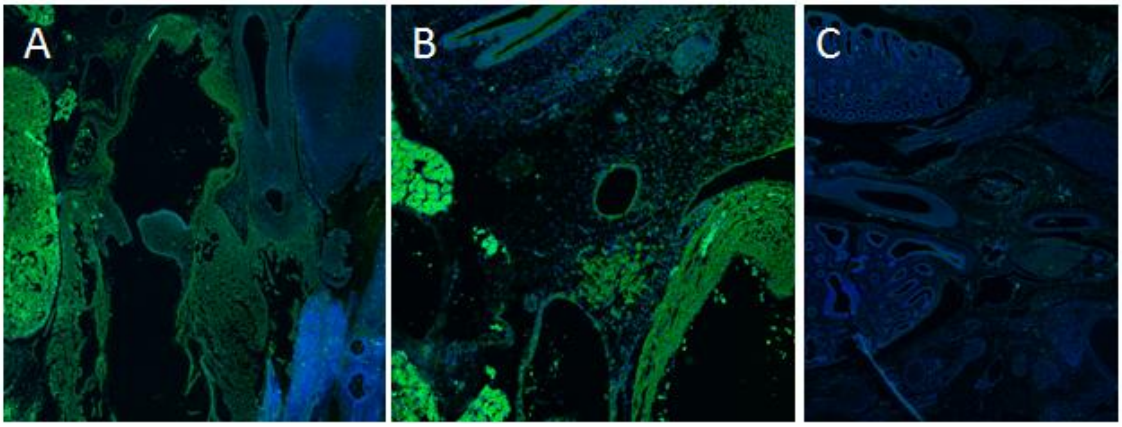

Figure 5.4 - Immunohistochemistry stains of Quek 1 antibody (green) with DAPI nuclear stain (blue) highlighting the valves, heart muscle, and vessel lumen. (A-B) heart valve and pharangeal arch arteries and (C) DAPI secondary control stain (Images courtesy of Jessica Ryvlin)

Multiple types of nanoparticles can be fabricated and two types in particular that have been used in biomedical applications are liposomes (Edwards & Baeumner, 2007) and polymers (Singh et al., 2014). Preliminary results in our lab show that liposome based particles have increased circulation time in embryos as compared to free molecule contrast, shown initially with liposomes containing FITC contrast media (Figure 5.4). High encapsulation efficiencies of contrast media, either FITC for preliminary studies of Visipaque for microCT imaging (Henning, Jiang, Yalcin, & Butcher, 2011), suggest feasibility with in-house particle fabrication with some future challenges with concentration of particles.

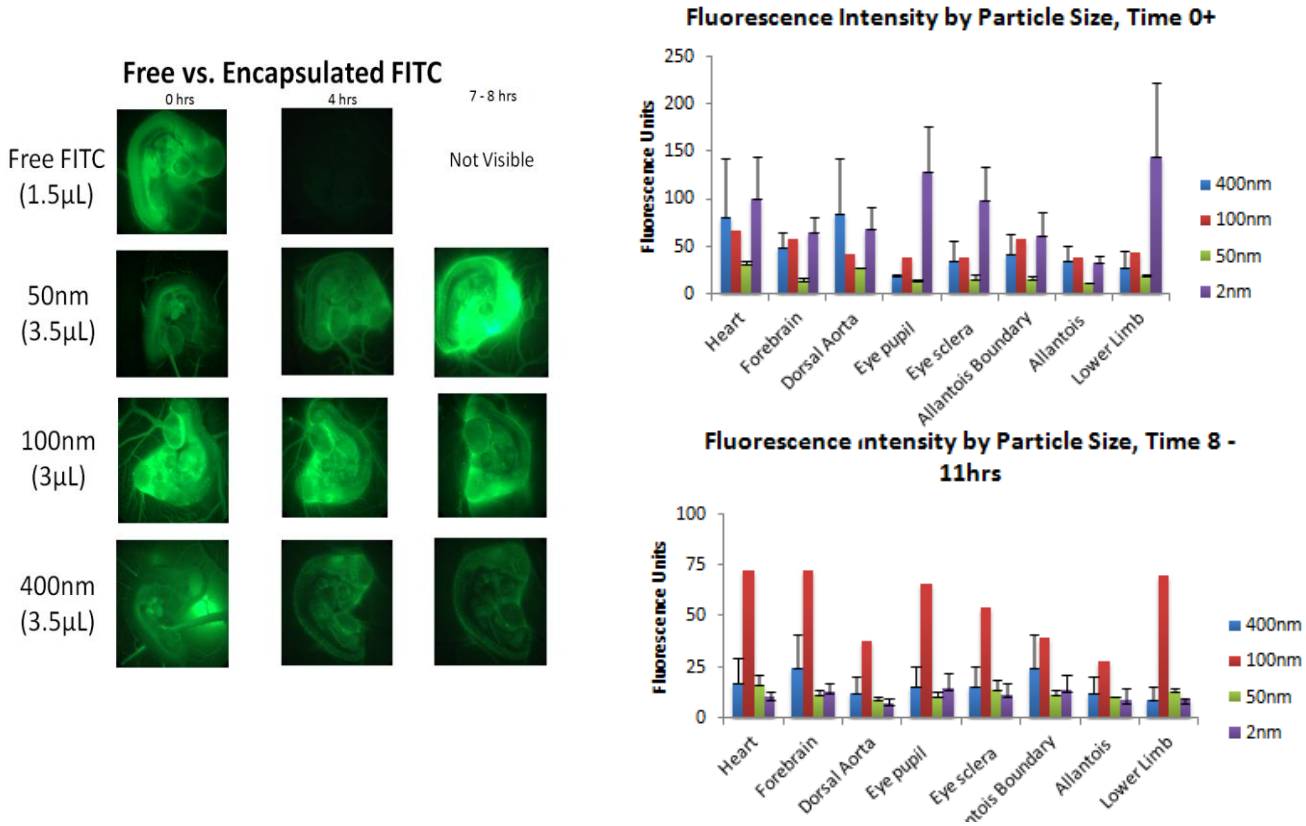

Figure 5.5 - Liposome nanoparticles containing FITC showing increasing persistence as compared to free FITC. Long term analysis of FITC liposomes of different sizes and their contrast enhancement immediately post injection and 8+ hours post injection. (Data courtesy of Tom Derrien)

Longitudinal imaging with tissue targeted contrast media would generate a 3D map of tissue patterning and dynamic changes. Coupled with diseased animal models and computational analysis, 3D mapping immune targeted tissues would reveal bulk cellular movements and identify changes in patterning. With the introduction of a diseased phenotype, underpinnings of the bulk cellular changes would suggest different mechanistic origins for further analysis.

Furthermore, extension of functionalizing the particle surface with microRNA (miRNA) has to potential for 3D quantitative genomic mapping. Specifically, surface conjugation with sequences implicated in cardiovascular development, such as miR-133a, allows for

cardiac genomic patterning with high resolution microCT imaging. More specifically, miR-133a is implicated in RhoA translocation in cardiomyocytes (Chiba & Misawa, 2010), revealing an interesting scientific landscape for probing and modifying transciptome wide changes in RhoA, a factor already implicated in abnormal valve development. Analysis of the synergistic effects between alternations in hemodynamics from LAL defect models and the causal outcomes to the regulatory miRNA networks during cardiogenesis will give multi-scale information for normal and abnormal tissue patterning and revealing genome wide mechanisms associated with gross scale tissue malformation.

All the future directions explored here are associated with cardiogenesis but the technologies presented in this dissertation are not limited to only heart development. Live in vivo microinjections deliver nanoparticles intravenously; therefore, any developing organ system with a high systemic vascular supply would benefit. In particular, we see great promise for understanding cranial-facial and limb development with the live imaging platforms presented here. We found that revealing cranial-facial structures was temporally dependent on post injection imaging time, suggesting that multiple different heterogeneous tissues are present and with continually changing material properties, all of which could be parsed out with longitudinal live 3D microCT imaging with nanoparticle based contrast media. Additionally, the embryonic limb is readily visualized during long term imaging with strong vascular supply highlighted immediately post injection but the soft tissues of the segmented limb along the proximal-distal axis is well seen within 24 hours post injection. Spatial and temporal analysis of

the limb establishes the coupled vascular supply with the soft and cartilaginous tissue maturation is imperative to visualize for assessing proper limb development particularly as it relates to underlying molecular gradients that are paramount during this morphogenetic process. Lastly, it is entirely reasonable to microinject nanoparticles into other circulations with the caveat of visualization of the injection site. Analysis of the lymphatics is of particular interest and has largely been overlooked in many developmental studies. Microinjection and imaging of lymphatic vessels is largely predicated on the ability to visualize the vessels or having a means for injection into circulation that moves directly into the lymphatics. If an animal model would allow for direct visualization of lymphatic vessels (ie fluorescently labeled transgenic models) or injection directly into the gut, then a clear route into the lymphatic circulation could be achieved with nanoparticle contrast media.

In conclusion, the work presented in this dissertation establishes to the first of our knowledge a live 3D imaging platform for mid-late stage development. We characterized nanoparticle based contrast media finding that particle size was an important indicator of contrast media toxicity and ability for long term visualization of soft tissues. Image datasets collected in live samples over 24 hours with nanoparticle exogenous soft tissue contrast gives the ability for long term tissue growth and maturation revealing live tissue growth metrics devoid of fixation and interpolation artifacts. Biodistribution, persistence, and contrast enhancement were age and organ specific, allowing for tissue heterogeneities to be quantified. Relative changes in the myocardium associated with the age and spatial orientation were determined non-

invasively showing increased tissue heterogeneity relationships indicative of tissue compaction and trabecular maturity. Coupling live microCT imaging with gated image acquisition revealed size, shape, blood distribution, and bulk trabecular density changes of the ventricle during systole and diastole. Gated image analysis of cardiac development reveals for the first time the functional consequences of normal cardiovascular morphodynamics that are imperative for establishing structure-function relationships in normal and abnormal tissue assembly. Collectively, this dissertation reveals a framework for probing morphological scale dynamics answering questions on longitudinal tissue maturation and heterogeneity. The scientific and engineering advancements presented here enable live 3D in vivo quantitative analysis of embryonic samples non-invasively that are paramount for coupling cellular/molecular scale biological assays with morphology for an entire multi-scale comprehensive understanding of live embryonic development.

References

Aleksandrova, A., Czirok, A., Szabo, A., Filla, M. B., Julius, M., Whelan, P. F., … Rongish, B. J. (2013). Convective tissue movements play a major role in avian endocardial morphogenesis, *363*(2), 348–361. http://doi.org/10.1016/j.ydbio.2011.12.036.Convective

Bellairs, R., & Osmond, M. (2014). *Atlas of Chick Development*. *Atlas of Chick Development*. http://doi.org/10.1016/B978-0-12-384951-9.00013-7

Butcher, J. T., Sedmera, D., Guldberg, R. E., & Markwald, R. R. (2007). Quantitative volumetric analysis of cardiac morphogenesis assessed through micro-computed tomography. *Developmental Dynamics : An Official Publication of the American Association of Anatomists*, *236*(3), 802–9. http://doi.org/10.1002/dvdy.20962

Chiba, Y., & Misawa, M. (2010). MicroRNAs and their therapeutic potential for human diseases: MiR-133a and bronchial smooth muscle hyperresponsiveness in asthma. *J Pharmacol Sci*, *114*, 264–8. http://doi.org/JST.JSTAGE/jphs/10R10FM [pii]

Cui, C., Filla, M. B., Jones, E. a V, Lansford, R., Cheuvront, T., Al-Roubaie, S., … Little, C. D. (2013). Embryogenesis of the first circulating endothelial cells. *PloS One*, *8*(5), e60841. http://doi.org/10.1371/journal.pone.0060841

Czirók, A., Rongish, B. J., & Little, C. D. (2004). Extracellular matrix dynamics during vertebrate axis formation. *Developmental Biology*, *268*(1), 111–22. http://doi.org/10.1016/j.ydbio.2003.09.040

Diaspro, A., Chirico, G., & Collini, M. (2005). Two-photon fluorescence excitation and related techniques in biological microscopy. *Quarterly Reviews of Biophysics*, *38*(2), 97–166. http://doi.org/10.1017/S0033583505004129

Dickinson, M. E., Simbuerger, E., Zimmermann, B., Waters, C. W., & Fraser, S. E. (2003). Multiphoton excitation spectra in biological samples. *Journal of Biomedical Optics*, *8*(3), 329–38. http://doi.org/10.1117/1.1583734

Edwards, K. A., & Baeumner, A. J. (2007). Synthesis of a liposome incorporated 1-carboxyalkylxanthine-phospholipid conjugate and its recognition by an RNA aptamer. *Talanta*, *71*(1), 365–372. http://doi.org/10.1016/j.talanta.2006.04.031

Eichmann, A., Marcelle, C., Brant, C., Douarin, N. M. Le, De, A., & Gabrielle, B. (1993). Two molecules related to the VEGF receptor are expressed in early endothelial cells during avian embryonic development F //////////// A I, *42*, 33–48.

Gould, R. A., Yalcin, H. C., MacKay, J. L., Sauls, K., Norris, R., Kumar, S., & Butcher, J. T. (2016). Cyclic Mechanical Loading Is Essential for Rac1-Mediated Elongation and Remodeling of the Embryonic Mitral Valve. *Current Biology*, *26*(1), 27–37. http://doi.org/10.1016/j.cub.2015.11.033

Gregg, C. L., & Butcher, J. T. (2013). Translational paradigms in scientific and clinical imaging of cardiac development. *Birth Defects Research. Part C, Embryo Today : Reviews*, *99*(2), 106–20. http://doi.org/10.1002/bdrc.21034

Henning, A. L., Jiang, M. X., Yalcin, H. C., & Butcher, J. T. (2011). Quantitative three-dimensional imaging of live avian embryonic morphogenesis via micro-computed tomography. *Developmental Dynamics : An Official Publication of the American Association of Anatomists*, *240*(8), 1949–57. http://doi.org/10.1002/dvdy.22694

Kim, J. S., Min, J., Recknagel, A. K., Riccio, M., & Butcher, J. T. (2011). Quantitative Three-Dimensional Analysis of Embryonic Chick Morphogenesis Via Microcomputed Tomography. *The Anatomical Record: Advances in Integrative*

Anatomy and Evolutionary Biology, *294*(1), 1–10. http://doi.org/10.1002/ar.21276

Roger, V. L., Go, A. S., Lloyd-Jones, D. M., Adams, R. J., Berry, J. D., Brown, T. M., … Wylie-Rosett, J. (2010). Heart Disease and Stroke Statistics--2011 Update: A Report From the American Heart Association. *Circulation*, 1–193. http://doi.org/10.1161/CIR.0b013e3182009701

Sedmera, D., Pexieder, T., Norman, H. U., & Clark, E. B. (1997). Developmental changes in the myocardial architecture of the chick. *Anatomical Record*, *248*(3), 421–432. http://doi.org/10.1002/(SICI)1097-0185(199707)248:3<421::AID-AR15>3.0.CO;2-R

Singh, A., Agarwal, R., Diaz-Ruiz, C. a, Willett, N. J., Wang, P., Lee, L. A., … García, A. J. (2014). Nanoengineered particles for enhanced intra-articular retention and delivery of proteins. *Advanced Healthcare Materials*, *3*(10), 1562–7, 1525. http://doi.org/10.1002/adhm.201400051

Squirrell, J. M., Wokosin, D. L., White, J. G., & Bavister, B. D. (1999). Long-term two-photon fluorescence imaging of mammalian embryos without compromising viability. *Nature Biotechnology*, *17*(8), 763–7. http://doi.org/10.1038/11698

Supatto, W., Débarre, D., Moulia, B., Brouzés, E., Martin, J.-L., Farge, E., & Beaurepaire, E. (2005). In vivo modulation of morphogenetic movements in Drosophila embryos with femtosecond laser pulses. *Proceedings of the National Academy of Sciences of the United States of America*, *102*(4), 1047–52. http://doi.org/10.1073/pnas.0405316102

Supatto, W., Mcmahon, A., Fraser, S. E., & Stathopoulos, A. (2009). Quantitative imaging of collective cell migration during Drosophila gastrulation: multiphoton

microscopy and computational analysis, *4*(10), 1397–1412. http://doi.org/10.1038/nprot.2009.130.Quantitative

Zamir, E. a, Czirók, A., Cui, C., Little, C. D., & Rongish, B. J. (2006). Mesodermal cell displacements during avian gastrulation are due to both individual cell-autonomous and convective tissue movements. *Proceedings of the National Academy of Sciences of the United States of America*, *103*(52), 19806–11. http://doi.org/10.1073/pnas.0606100103

CHAPTER 6

EFFECTIVE ENGAGEMENT OF INQUIRY BASED LEARNING IN THE K-12 SCIENCE CLASSROOM: AN EX OVO CHICK CULTURE FOR THE STUDY OF ETHANOL ON EMBRYONIC DEVELOPMENT

6.1 Abstract

In the 2013-2014 academic school year, I participated in the Cornell's Learning Initiative in Medicine and Bioengineering (CLIMB) program as a National Science Foundation GK-12 fellow. The GK-12 program pairs current PhD students in STEM fields with local middle and high school teachers for enhancement of science curriculum through hands-on inquiry based learning. I partnered with Jill Browne, a middle school teacher at two local schools in Binghamton, NY. Together I was her "resident scientist" in her classroom, aiding in the incorporation of open ended, experimental design based lessons. Furthermore, for an intensive 6 week period in the summer preceding the school year, I immersed Jill in the laboratory at Cornell University under my guidance allowing her to experience scientific research first hand. During my time as a GK-12 fellow, I implemented science curricula based on research principles for local middle school students and enabled my teacher to implement these lessons for future academic school year lessons. In this chapter, I overview my GK-12 experience, the lessons that I taught, and the scientific and pedagogical results. This work was presented at the 2014 annual Biomedical Engineering Society Conference.

6.2 Introduction

Congenital defects are common physical anomalies that occur during embryonic development. The severity of the defects varies from mild, requiring no medical intervention, to life threatening necessitating multiple medical interventions. The avian embryo has been used extensively in developmental research due to many factors namely affordability, short gestation, and similarity to human development. Furthermore, the avian embryo can be cultured *ex ovo* (outside the shell), allowing for easy access and visibility of the embryo for experimental perturbations and teaching. Using an *ex ovo* chick embryo model, a middle school teacher and her 8th grade students were asked to choose a chemical and hypothesize how it would affect embryonic development establishing quantitative metrics to measure any teratogenic effects that may be occurring. These activities support the GK-12 classroom for the introduction to developmental biology, experimental design, animal research, and scientific ethics.

6.3 Experimental and Pedagogical Methods

Prior to beginning the experimental design, the teacher and students were introduced to basic heart anatomy and the stages of heart development. Furthermore, a lesson in animal model use in biomedical science with a particular emphasis on the history of the chick embryo model was taught prior to the experiment. Using the *ex ovo* culture system, the teacher and students chose to investigate the effects of ethanol (15%) on embryonic development. Fertilized eggs were incubated for 3 days at 99.5˚F with 55%

humidity until being cultured on day 3 of development. The chicks were incubated in portable, Styrofoam incubators. Beginning on day 4 of development, the chicks were treated with 100µL of 15% ethanol with 1x EBSS serving as the control. The heart rate was quantified through changes in heart rate observed before and after treatment. Anatomical changes were found by measuring the crown rump length (CRL), wing length (WL), foot length (FL), and eye diameter (ED) after the termination of the experiment on day 7 of development.

Materials

- Fertilized eggs (local farm)
- Styrofoam portable incubator (Little Giant Still Air egg incubator)
- Egg holders
- Clear plastic cups (9oz)
- Plastic wrap
- Rubber bands
- Ethanol diluted to 15% and 70%
- Pipette and pipette tips
- ImageJ (National Institutes of Health)

Methods

<u>Part 1: Prepare ex ovo culture cups</u>

1. Fill clear plastic cups 2/3 with water
2. Make a plastic wrap hammock, touching the plastic wrap to the water

3. Secure the plastic wrap around the cup with a rubber band
4. Disinfect the plastic wrap with ethanol (70%)
5. Cover cups with plastic lid until ready to culture

Part 2: Ex Ovo Culture

1. Incubate fertilized eggs for 3 days at 99.5˚F and 55% humidity
2. Gently crack the side of the egg
3. Place thumbs in shell crack and pull apart directly over plastic wrap hammock
4. Make sure embryo is facing up and cover with plastic lid
5. Place entire ex ovo culture in portable incubators for later use

Part 3: Long Term Ethanol Treatment

1. Prior to ethanol exposure, record the embryonic heart rate for 15 seconds
2. Pipette 100µL of 15% ethanol onto the top of the embryo, use Earl's Balanced Salt Solution (EBSS) or another neutral buffer as a control

Figure 6.1 - Ex ovo culturing method (photos courtesy of Jen Richards)

3. Repeat heart rate measurement immediately post exposure
4. Repeat ethanol exposure until day 7 of development, recording heart rates before and after exposure
5. Sacrifice the embryos on day 7 of development

6. Fix the embryos in 4% paraformaldeyde (optional)

Data Analysis

Heart rate measurements are taken for 15 seconds immediately before and after ethanol exposure each day from days 3-7 of development. Heart rate values are compared between the experimental ethanol exposure groups and the control groups treated with EBSS. Anatomical measurements were taken of sacrificed samples for comparison of teratogenic affects of the ethanol exposure. Measurements of the crown-rump length (CRL), wing length (WL), leg length (LL)< and eye diameter were completed in ImageJ and compared between the experimental and control groups. Statistical significance is determined from a p value less than 0.05 with a standard T-test.

6.4 Results

It was found that ethanol treatment statistically decreases the heart rate during development as compared to controls. The rate of change of the heart rate in the chicks surviving the ethanol treatment decreases whereas in normal chicks increases indicative of tissue maturation (Figure 6.2). In chick embryos surviving the ethanol treatment, morphological changes were detected at the end of the experiment on day 7 (Figure 6.2). The chick embryos were sacrificed, removed from their extraembryonic structures, and imaged. The teacher and students measured the CRL, FL, WL, and ED. Decreases were observed in all structures. This experimental design and analysis structure educated the students and teacher about introduction embryonic development

and interfacing with development form an external factor, in this instance a chemical agent. It put into perspective how environmental changes can influence biological activity. Furthermore, the activity was entirely driven by the teach and the students through inquiry based scientific discovery.

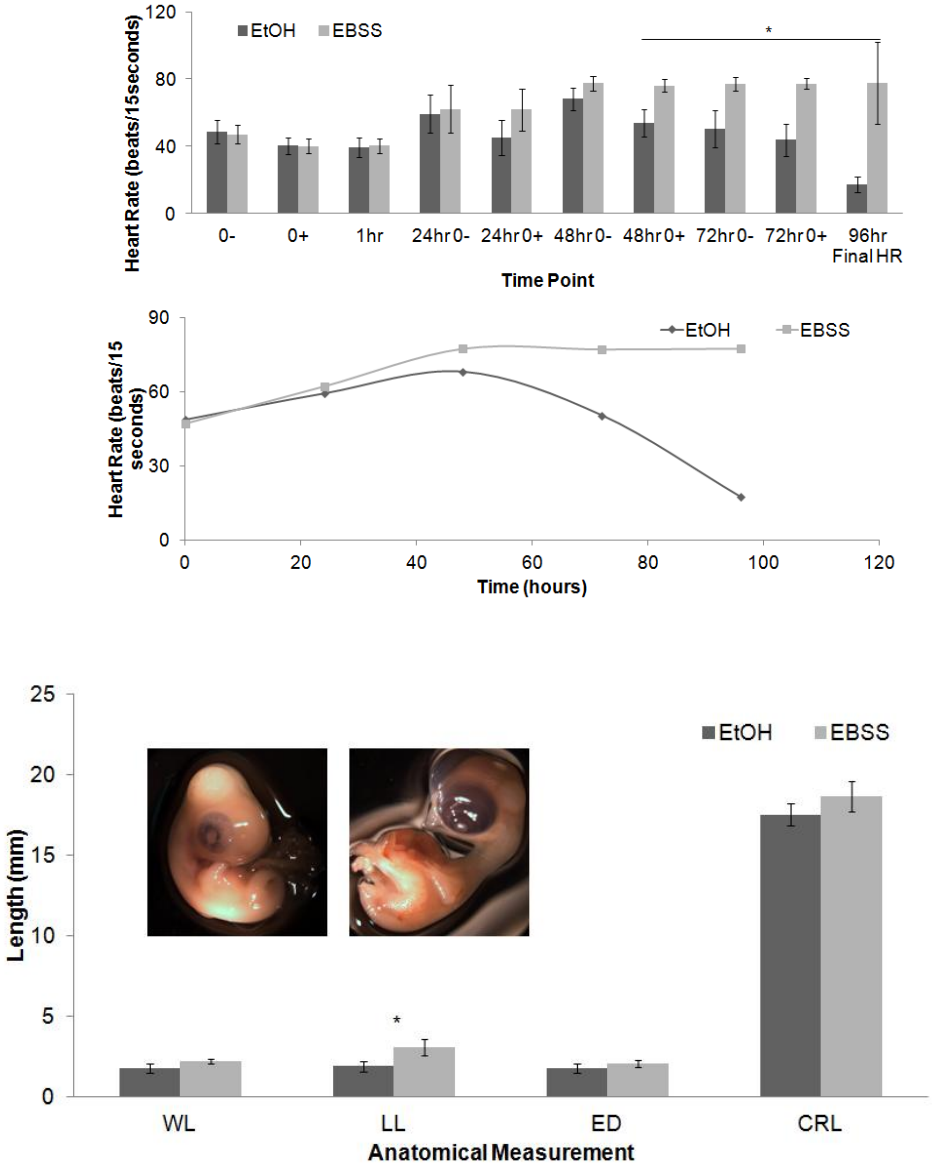

Figure 6.2 - Heart rate and anatomical analysis of long term ethanol exposure to developing chick embryos. Heart rate measurements for longitudinal ethanol exposure and modeled rate of change of the heart rate over time (top) and anatomical analysis of embryonic morphology for ethanol toxicity

6.5 Discussion

After working for a year with two middle school classrooms, the teach and students were able to understand the scientific method from asking a scientific question, developing a hypothesis, experimental design, data analysis, and formulating conclusions based on the data. The teacher was able to incorporate the principles of biomedical science into her curriculum using the development of the cardiovascular system as a vehicle for teaching these larger scientific principles. The students gained experience into how scientific research is completed through a hands-on experiment. The *ex ovo* chick culture provided a visual, interactive platform for the study of biological systems and how altering the environment can cause dramatic downstream effects. The students and teacher gained a better understanding and appreciation of scientific learning through inquiry and the dynamics of scientific research. Furthermore, this experiment is inexpensive and all materials are easily purchased, giving flexibility for the teacher to incorporate these models into her future classes.

APPENDIX A

GK-12 PRE AND POST TEST FOR EVALUATING STUDENT LEARNING

1) List 4 reasons why the chicken embryo is a useful model organism (2pts.)
    A)
    B)
    C)
    D)

2) True or False : It is important to have controls when performing an experiment? (2pt)
    A) True
    B) False

3) Outline the most important elements when making an experimental design (10pts)

4) Give three reasons why it is critical to use animal models in biomedical research (6pts)

5) Why is studying embryonic development important for understanding human disease? (10pts.)

APPENDIX B

RELEVANT PROTOCOLS

Incubator Sterilization for Live Chick Embryos

Materials

- Styrofoam incubator (Tractor Supply Company 216737999)
- Tin foil
- Disposable plastic cups
- Egg cartons
- 80% bleach
-

Sterilization Technique

1. Bleach inside of incubator, base and lid, with 80% bleach
2. Let incubator, treated with bleach, sterilize overnight
3. Autoclave tin foil, enough to cover base grate of incubator
4. After bleaching incubator overnight, remove excess bleach from the incubator
5. Treat incubator with 70% ethanol and remove excess ethanol
6. Place autoclaved tin foil onto base grate
7. UV sterilize base and lid of incubator, two egg cartons with the lids removed, and 2 disposable plastic cups for a minimum of 1 hour
8. After UV sterilization is complete, fill the plastic cups with water and place the lid of the incubator onto the base
9. Plug in incubator and allow to come to temperature (99.5˚F)

Incubator Maintenance During Experiment

1. Keep the disposable plastic cups full of water for the duration of the experiment to maintain appropriate humidity
2. Handle incubators with gloves to maintain adequate sterility for sample viability
3. Minimize internal incubator exposure to ambient environment by handling embryonic samples inside the laminar flow hood whenever possible

In Ovo Chick Culture Protocol

Materials

- Styrofoam incubator (Tractor Supply Company 216737999)
- Plastic wrap
- Masking tape
- Dissection scissors
- 70% ethanol
- Standard scissors
- 21 gauge needle
- 10mL syringe
- Cornell Poultry eggs

Egg Order and Pre-Culture Incubation

1. Order eggs, by the dozen, from Cornell Poultry (607-272-8970)
2. Place eggs in the large, tilting incubators with date and initials labeled in pencil
3. Check the water basin, keep filled for incubation
4. Culture eggs after 3 days of incubation

Culturing Sterilization

1. Autoclave dissection scissors
2. UV sterilize plastic wrap and standard scissors
3. Sterilize incubator per described

In Ovo Culturing

1. Remove eggs from large tilting incubators (approximately 4-6 at a time)
2. Clean the eggs with 70% ethanol
3. Make a small hole on the narrow end of the egg, opposite of where the embryo is located, with the dissection scissors
4. Remove 5-7mL of albumin (depending on the egg size) with a sterile 21 gauge needle and sterile 10mL syringe, cover hole with small piece of masking tape
5. Place two strips of masking tape lengthwise along the egg
6. Cut a whole along the length of the egg approximately 3.5 centimeters in diameter
7. Cover the egg with sterile plastic wrap
8. Store egg in Styrofoam incubator until completion of the experiment

In Ovo Egg Disposal

1. Place any in ovo living cultured samples into in tack egg cartons
2. Freeze samples in the 4˚C freezer
3. Once frozen, dispose of egg cartons in garbage

In Ovo MicroInjection Protocol

Materials

- Silicon tubing
- Pipette tips
- 3mL sterile syringe
- Pulled and beveled glass needles
- Injection media
- 3D translational stage
- Dissection microscope
- Egg carton
- Standard scissors

Sterilization

1. Autoclave silicon tubing and pipette tips
2. UV sterilize beveled glass needles and standard scissors

MicroInjection Set Up

1. Place dissection microscope and 3D translational stage in Laminar flow hood
2. Place half of one egg carton, lid removed, under the dissection scope for holding the egg
3. Using standard scissors, cut the top of a sterile pipette tip at the first line
4. Secure cut pipette tip to a the end of a sterile 3mL syringe

5. Place one end of the silicon tubing to the end of the pipette tip
6. Without pressure in the line, load injection media into the silicon tubing
7. Secure glass needle at the end of the silicon tubing and place into 3D translational stage
8. Pressurize the line with the 3mL syringe and remove air from the needle
9. Once pressurized, remove the 3mL syringe until injection
10. Note: See Butcher et al 2007 paper for microinjection apparatus

Live In Vivo MicroInjections

1. Place one embryo directly from the incubator under the dissection microscope
2. Visualize the extra embryonic vasculature and position the translational stage with needle above the location for injection
3. Looking through the microscope, position the needle and plunge into the blood vessel
4. Replace the 3mL syringe and inject media into the vasculature
5. Once media is injected, remove the 3mL syringe and remove the needle from the blood vessel
6. Replace the plastic wrap onto the embryo and house in the incubator until needed

Contrast Media Toxicity Analysis Protocol

Materials

- Contrast media
- 1X Earl's balanced salt solution (EBSS)
- Microinjection set up
- Timer
- 4% paraformaldehyde (PFA)
- Dissection scissors
- 5 forceps
- 1X phosphate buffered saline (PBS)

Sample Treatment and Heart Rate Analysis

1. Load contrast media into the microinjection set up
2. Visualize the embryo under the dissection microscope and record the embryonic heart rate for 15 seconds
3. Inject the contrast media into the embryo
4. Immediately post injection, record the heart rate for 15 seconds
5. Record the heart rate for 15 seconds 1 hour and 24 hours post injection
6. Inject 1X EBSS as a sham control, record the heart rates to use as a comparator

End Point Fixation and Anatomical Analysis

1. Monitor embryonic samples each day until day 10 of development
2. Discard of any samples, both treated and control, that have died and dispose of them
3. Record all embryos that have died to control for general variations in viability
4. On day 10 of development, sacrifice the samples
5. Cut the embryo out of the extra embryonic membranes an vasculature, do not harm the embryonic body
6. Transfer it to a large petri dish
7. Wash the embryo with 1X PBS
8. Using the# 5 forceps (Fine Science Tools 11251-10), remove any excess extra embryonic tissue, leaving only the embryo proper
9. Repeat washing the embryo in PBS
10. Fix the samples in 4% PFA in a 50mL conical tube for 48 hours
11. Dispose of the PFA and wash the samples in 1X PBS
12. Image the samples on a flat surface with the stereo Zeiss microscope
13. Image the entire embryo, the foot, wing, and eye
14. Measure the foot length, wing length, eye diameter, and the entire body crown-rump length in ImageJ using the line tool
15. Control for the scale appropriately
16. Compare heart rate and anatomical measurements between the treated contrast media samples and the EBSS controls

50um MicroCT Live Imaging Scan Protocol

Materials

- Custom made polycarbonate imaging chamber
- GE bone standard (SB3)
- In ovo cultured live embryos microinjected with contrast media

Scan Preparation

*Note: If the microCT had recently been used, the anode heat must be below 15% prior to the next imaging session for preserving the life of the x-ray tube. The anode heat is listed under the 'System' tab

1. Place the polycarbonate imaging chamber onto the sliding platform
2. The bone standard will sit inside of the imaging chamber, below the embryo
3. Open the already installed GE software on the microCT imaging computer
4. From the tabs on the left side of the interface, select the Scan tab
5. Once inside the scan tab, select JOE Fast Fluoro 80kV from the drop down menu

Live Imaging

1. Transfer the Styrofoam incubator to the imaging facility
2. Remove the embryo to be imaged from the incubator and place it onto the platform in the imaging chamber secured with a piece of tape

3. Keep the plastic wrap secured around the embryo to maintain sterility
4. Close microCT hatch and secure it against the machine
5. On the microCT computer, select for fluoroscopy view
6. Adjust the field of view with the right and left arrows to center the egg within the window
7. Once the egg is centered in the field of view, end the fluoroscopy view
8. Select run protocol in the lower right corner of the scan window
9. The scan will run until all 800 projections have been acquired, the projection number is designated in the top left corner of the monitor showing the image field of view
10. After the scan is complete, press ‘Return to Home’ on the microCT screen attached to the machine
11. The platform will move to the starting position within the hatch
12. Raise the hatch and remove the embryo from the imaging chamber and place it back into the incubator

MicroCT Image Reconstruction

Calibration of the Bone Standard

1. Open the thumbnail image file, the image stack will open in MicroView
2. Using the three button mouse, locate the bone standard in the image
3. From the panel on the left side of the image viewer, select the ROI tool
4. A yellow ROI box will appear in the center of the image
5. Adjust the dimensions of the ROI and position it on the corner edge of the bone standard
6. Part of the ROI should contain the bone standard and the rest should contain the air
7. In the GE microCT panel, select the acq file and press ‘Send to Recon’ in the lower right corner of the screen
8. Open the recon tab seen on the left side of the panel
9. Once inside the window, select the file sent to recon in the lower left section
10. Name the reconstruction in the main panel
11. In the MicroView window with the bone standard selected ROI select File → Save Crop Coordinates
12. In the recon panel, select the scan to be reconstructed
13. You should see the coordinates change
14. Select 32 bit
15. Select recon in the lower right of the panel

16. You should see the recon appear in the upper left panel with a status bar

Water and Air Calibration

1. Once the bone calibration image is complete, a new file with appear in the microCT image window, double click on the file to open in MicroView
2. Select ROI in the left hand panel, adjust the size of the ROI so it samples a small section of the acrylic bone standard
3. Press ‘M’ and record the median number
4. Move the ROI so it samples a small amount of the air around the bone standard
5. Press ‘M’ and record the median number again
6. Close the MicroView window

Image Reconstruction

1. Reopen the original thumbnail file
2. Repeating the ROI selection process, position the 3 planes of the ROI within the image space to capture the entire embryo
3. Minimize the excess space in the ROI not capturing the embryo in order to reduce the total file size
4. In the recon window of the microCT imaging panel, re-name the file for the final reconstruction
5. Save the crop coordinates and load them into the recon tab
6. Manually enter the air and acrylic calibration values for the air and water designations respectfully

7. Note: BE SURE TO UNSELECT THE 32 BIT OUTPUT
8. Select recon in the lower right of the main panel
9. The status of the reconstruction will appear in the upper left panel in the window
10. Once the reconstruction is complete, a new image file will appear in the main microCT imaging window

Obtaining MicroCT Image Stacks

Exporting the Image Files

- Once the image has been reconstructed on the microCT computer, the file can be dropboxed and copied into the image file share
- The image files can be accessed in the following way:
- Right click → Open the CT drive
- A window will open and all files associated with this image acquisition will be available

Reducing File Size in SliceView

1. Either file share or dropbox the reconstructed image stack in VFF format
2. Download the image stack into SliceView
3. SliceView can be downloaded here: http://gehc-sliceview.software.informer.com/
4. In SliceView: File → ROI Selection
5. In the ROI window, select the x, y, and z specifications that contain the sample
6. Save the new VFF image stack for use

Saving VFF Files as a DICOM Stack in MicroView

1. Open the VFF stack saved from SliceView into MicroView
2. MicroView can be downloaded here: http://microview.sourceforge.net/
3. Create a new folder
4. Export the VFF image stack as a DICOM stack into the newly created folder

5. File → Image Export → DICOM format → select the new folder
6. Note: some analysis is completed in MicroView using VFF files and additional analysis is completed in OsiriX using a DICOM image stack
7. Import the DICOM image stack into any image analysis platform needed

Contrast Intensity Measurements

Identifying Structures of Interest

1. Open the VFF image file in MicroView
2. Manipulate the planes to view a cross section of the sample with the organ of interest seen within the plane
3. Adjust contrast levels to make the background as close to black as possible while maintaining good visibility of the sample
4. Note: This will vary by age of sample and time post injection from contrast media

Line Tool Contrast Plots

1. One the plane with the structure of interest has been identified, go to Edit → Show Line
2. A line will appear in the image space with end marks denoted by blue and green arrows
3. A plot will be produced that is the contrast enhancement (HU) vs. distance along the line
4. Place the cursor over the first end position you want the line and press ‘1’ and repeat cursor placement for the second end position and press ‘2’
5. The blue arrow will move to the first location and the green to the final location
6. Note: Background contrast should be subtracted from the measured contrast in the structure of interest to find the absolute contrast level; therefore, make the line long enough to incorporate background

7. Once you have your line positioned, select Tools → Plot
8. The plot will be contrast level (HU) vs. position along the line moving from the blue to the green arrow
9. For peak contrast enhancement, measure the rough average of the highest peaks for the structure of interest (See figure)
10. This can be done manually by placing the cursor over the peak that is being measured
11. Below the plot you will see coordinates for the exact position of the cursor
12. Measure the rough average background contrast in the image that should be subtracted from the peak contrast measurement to have the absolute peak contrast value (See figure)
13. Often times this will be a negative number which means the contrast value will be higher than what the peak appears
14. For example:
    a. Measured Peak = 1500 HU
    b. Background Noise = -100 HU
    c. Absolute Peak Contrast = 1500 – (-100) = 1600 HU
15. For average contrast measurements throughout an entire structure, the contrast enhancement plot can be exported as a text file
16. Select File → Save Data
17. Save the text file and then copy the information to Excel
18. Note: Be sure to know the position (x coordinate) for the border of the structure of interest

19. Take the average contrast value within the spatial range of the structure of interest

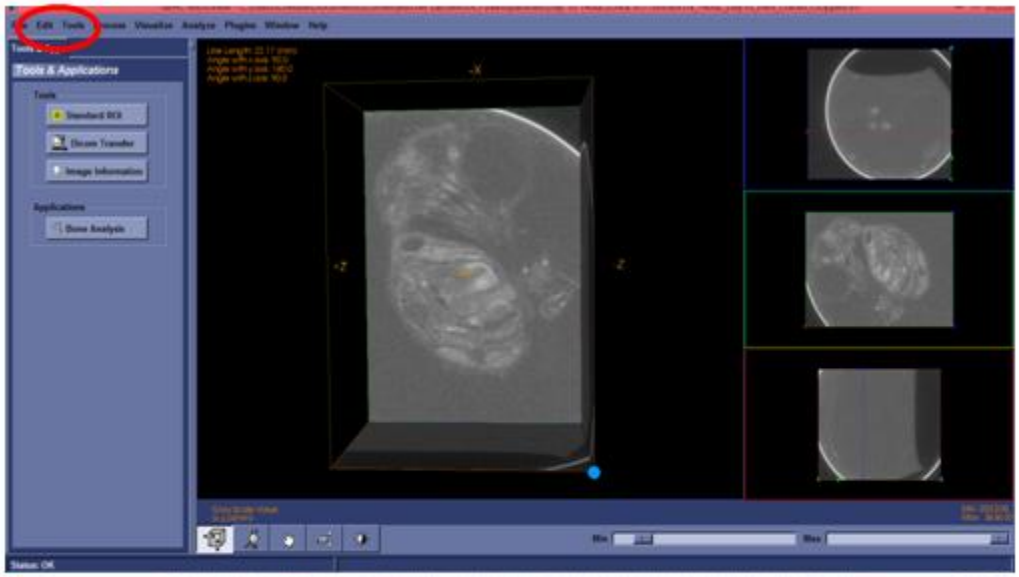

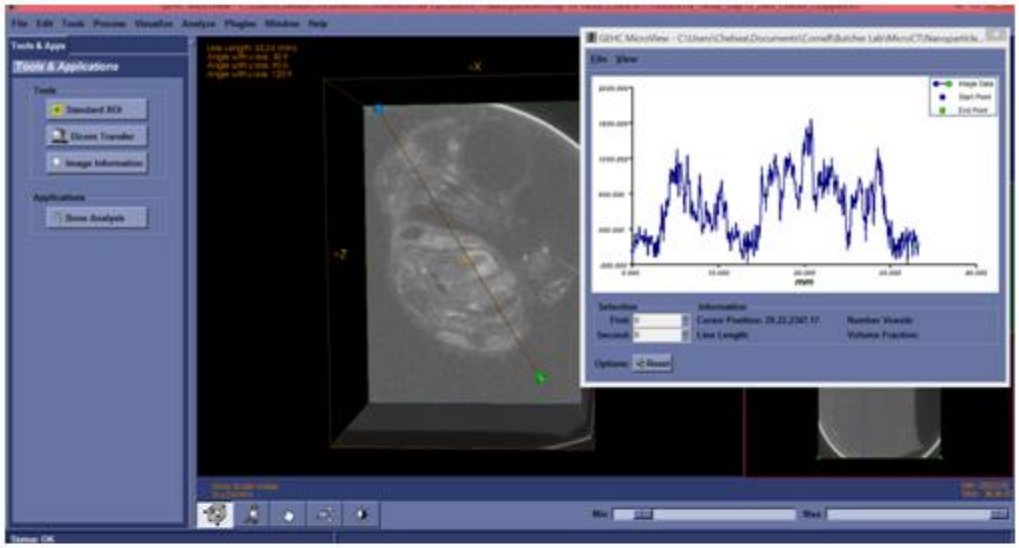

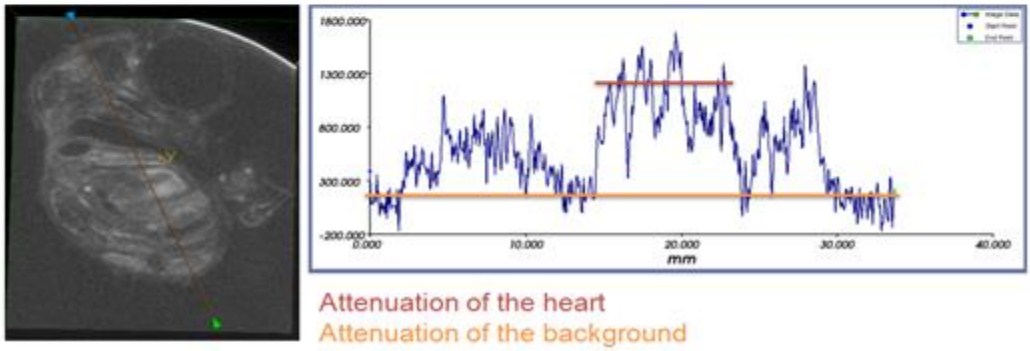

APPENDIX C

MATLAB SCRIPTS

Threshold Image Filter

```
function Threshold(im)

original = imread(im);

level = graythresh(original);

BW = im2bw(original,level);;

figure(1);

imshow(BW)

end
```

Gaussian Image Filter

```
function Gaussian(im, size, sigma, noiseType)

original = imread(im);

grayscale = rgb2gray(original);

figure(1);

imshow(original);

figure(2);

imshow(grayscale);

%Generate Gaussian matrix

h = fspecial('gaussian', size, sigma);

%Convolve the image with the Gaussian kernel

M = conv2(double(grayscale), double(h));

%Display the result

figure (3);

imshow((M.^2).^0.5, []);

end
```

Wiener Image Filter

```
function Wiener (im, len, theta)


original = imread(im);

grayscale = rgb2gray(original);

figure(1);

imshow(original);

figure(2);

imshow(grayscale);


PSF = fspecial('motion', len, theta);


Quantized = imfilter(grayscale,PSF, 'conv', 'circular');

UniformQuantizedVar = (1/256)^2/12;

signal_var = var(im2double(grayscale(:)));

wnr = deconvwnr(Quantized, PSF, UniformQuantizedVar/signal_var);


figure(3);

imshow(wnr)

end
```

Sobel Image Filter

```
function Sobel(im)

%Read in the image and convert to gray
UpwardOriginal = imread(im);
grayscale = rgb2gray(UpwardOriginal);

figure(1);
imshow(grayscale);

%Define the Sobel kernels
k_v = [-1 0 1; -2 0 2; -1 0 1];
k_h = [1 2 1; 0 0 0; -1 -2 -1];

%Convolve the gray image with Sobel kernels, store result in M1 and M2
M1 = conv2(double (grayscale), double(k_v));
M2 = conv2(double(grayscale), double (k_h));

%Display the horizontal edges and vertical edges separately
figure(2);
imshow(abs(M1), []);
figure(3);
imshow(abs(M2), []);
```

```
%Display the normalized vertical and horizontal edges combined
figure(4)
imshow((M1.^2+M2.^2).^0.5, []);


end
```

Edge Detection Image Filter

*Note: This program couples multiple filters together to produce to detect horizontal and vertical edges of an image

```
function EdgeExtraction(im, size, sigma, noiseType, len, theta)

original = imread(im);
grayscale = rgb2gray(original);
level = graythresh(grayscale);
BW = im2bw(grayscale, level);

figure (1);
imshow(original);
title('Original');

figure (2);
imshow(BW)
title('Threshold Image');

h=fspecial('gaussian', size, sigma);

M = conv2(double(BW), double(h));
```

```
figure(3);

gaussian = (M.^2).^0.5;

imshow(gaussian, []);
title ('Gaussian Filter');

PSF = fspecial('motion', len, theta);

quantized = imfilter(gaussian, PSF, 'conv', 'circular');
UniformQuantizedVar = (1/256)^2/12;
signal_var = var(im2double(gaussian(:)));
wnr = deconvwnr(quantized, PSF, UniformQuantizedVar/signal_var);

figure(4);
imshow(wnr)
title('Wiener Filter');

%Define the Sobel kernels
k_v = [-1 0 1; -2 0 2; -1 0 1];
k_h = [1 2 1; 0 0 0; -1 -2 -1];

%Convolve the gray image with Sobel kernels, store result in M1 and M2
```

```
M1 = conv2(double (wnr), double(k_v));

M2 = conv2(double(wnr), double (k_h));


%Display the horizontal edges and vertical edges separately

%figure(2);

%imshow(abs(M1), []);

%figure(3);

%imshow(abs(M2), []);


%Display the normalized vertical and horizontal edges combined

figure(5)

imshow((M1.^2+M2.^2).^0.5, []);

title('Edge Extraction');


end
```

Day 7 Bulk Nanoparticle Concentration Model

```
function [fitresult, gof] = createFits(D7LVM_Distance, D7LVM_Concentration,
D7RVM_Distance, D7RVM_Concentration)
%CREATEFITS(D10LVM_DISTANCE,D10LVM_CONCENTRATION,D10RVM_DISTAN
CE,D10RVM_CONCENTRATION,D7LVM_DISTANCE,D7LVM_CONCENTRATION,D7
RVM_DISTANCE,D7RVM_CONCENTRATION)
%  Create fits.
%
%  Data for 'D7 LVM NP Concentration' fit:
%      X Input : D7LVM_Distance
%      Y Output: D7LVM_Concentration
%  Data for 'D7 RVM NP Concentration' fit:
%      X Input : D7RVM_Distance
%      Y Output: D7RVM_Concentration
%  Output:
%      fitresult : a cell-array of fit objects representing the fits.
%      gof : structure array with goodness-of fit info.
%% Initialization.

% Initialize arrays to store fits and goodness-of-fit.
fitresult = cell( 2, 1 );
gof = struct( 'sse', cell( 2, 1 ), ...
```

```
    'rsquare', [], 'dfe', [], 'adjrsquare', [], 'rmse', [] );

%% Fit: 'D7 LVM NP Concentration'.
[xDataLV, yDataLV] = prepareCurveData( D7LVM_Distance, D7LVM_Concentration );

% Set up fittype and options.
ft = fittype( 'gauss1' );
opts = fitoptions( 'Method', 'NonlinearLeastSquares' );
opts.Display = 'Off';
opts.Lower = [-Inf -Inf 0];
opts.StartPoint = [17.6565008025682 0.39743 0.13275749571614];

% Fit model to data.
[fitresult{1}, gof(1)] = fit( xDataLV, yDataLV, ft, opts );

% Plot fit with data.
figure( 'Name', 'D7 LVM NP Concentration' );
hLV = plot( fitresult{1}, xDataLV, yDataLV );
legend( hLV, 'D7LVM_Concentration vs. D7LVM_Distance', 'D7 LVM NP
Concentration', 'Location', 'NorthEast' );
% Label axes
xlabel( 'D7LVM_Distance' );
ylabel( 'D7LVM_Concentration' );
```

```
grid on


%% Fit: 'D7 RVM NP Concentration'.
[xDataRV, yDataRV] = prepareCurveData( D7RVM_Distance, D7RVM_Concentration );


% Set up fittype and options.
ft = fittype( 'gauss1' );
opts = fitoptions( 'Method', 'NonlinearLeastSquares' );
opts.Display = 'Off';
opts.Lower = [-Inf -Inf 0];
opts.StartPoint = [14.8029249152845 0.433561 0.143503737494977];


% Fit model to data.
[fitresult{2}, gof(2)] = fit( xDataRV, yDataRV, ft, opts );


% Plot fit with data.
figure( 'Name', 'D7 RVM NP Concentration' );
hRV = plot( fitresult{2}, xDataRV, yDataRV );
legend( hRV, 'D7RVM_Concentration vs. D7RVM_Distance', 'D7 RVM NP
Concentration', 'Location', 'NorthEast' );
% Label axes
xlabel( 'D7RVM_Distance' );
ylabel( 'D7RVM_Concentration' );
```

```
grid on


% Plot fits with data on same plot.
figure( 'Name', 'D10 Ventricular Myocardium NP Concentration' );
hLV = plot(fitresult{1}, xDataLV, yDataLV);
hold on
hRV = plot (fitresult{2}, xDataRV, yDataRV);
```

Day 7 Bulk Nanoparticle Transport Model

```
function [fitresult, gof] = createFits(D7LVM_Distance, D7LVM_Perfusion,
D7RVM_Distance, D7RVM_Perfusion)
%CREATEFITS(D7LVM_DISTANCE,D7LVM_PERFUSION,D7RVM_DISTANCE,D7RV
M_PERFUSION,D10LVM_DISTANCE,D10LVM_PERFUSION,D10RVM_DISTANCE,D
10RVM_PERFUSION)
%  Create fits.
%
%  Data for 'D7 LVM Perfusion' fit:
%      X Input : D7LVM_Distance
%      Y Output: D7LVM_Perfusion
%  Data for 'D7 RVM Perfusion' fit:
%      X Input : D7RVM_Distance
%      Y Output: D7RVM_Perfusion
%
%  Output:
%      fitresult : a cell-array of fit objects representing the fits.
%      gof : structure array with goodness-of fit info.
%% Initialization.

% Initialize arrays to store fits and goodness-of-fit.
fitresult = cell( 2, 1 );
```

```
gof = struct( 'sse', cell( 2, 1 ), ...
    'rsquare', [], 'dfe', [], 'adjrsquare', [], 'rmse', [] );

%% Fit: 'D7 LVM Perfusion'.
[xDataLV, yDataLV] = prepareCurveData( D7LVM_Distance, D7LVM_Perfusion );

% Set up fittype and options.
ft = fittype( 'exp1' );
opts = fitoptions( 'Method', 'NonlinearLeastSquares' );
opts.Display = 'Off';
opts.StartPoint = [1.76274621204252e-05 4.87217655800437];

% Fit model to data.
[fitresult{1}, gof(1)] = fit( xDataLV, yDataLV, ft, opts );

% Plot fit with data.
figure( 'Name', 'D7 LVM Perfusion' );
hLV = plot( fitresult{1}, xDataLV, yDataLV );
legend( hLV, 'D7LVM_Perfusion vs. D7LVM_Distance', 'D7 LVM Perfusion', 'Location',
'NorthEast' );
% Label axes
xlabel( 'D7LVM_Distance' );
ylabel( 'D7LVM_Perfusion' );
```

```
grid on


%% Fit: 'D7 RVM Perfusion'.
[xDataRV, yDataRV] = prepareCurveData( D7RVM_Distance, D7RVM_Perfusion );


% Set up fittype and options.
ft = fittype( 'exp1' );
opts = fitoptions( 'Method', 'NonlinearLeastSquares' );
opts.Display = 'Off';
opts.StartPoint = [2.50196571591508e-05 2.92980444938307];


% Fit model to data.
[fitresult{2}, gof(2)] = fit( xDataRV, yDataRV, ft, opts );


% Plot fit with data.
figure( 'Name', 'D7 RVM Perfusion' );
hRV = plot( fitresult{2}, xDataRV, yDataRV );
legend( hRV, 'D7RVM_Perfusion vs. D7RVM_Distance', 'D7 RVM Perfusion', 'Location',
'NorthEast' );
% Label axes
xlabel( 'D7RVM_Distance' );
ylabel( 'D7RVM_Perfusion' );
grid on
```

```
% Plot fits with data on same plot.
figure( 'Name', 'D10 Ventricular Myocardium NP Concentration' );
hLV = plot(fitresult{1}, xDataLV, yDataLV);
hold on
hRV = plot (fitresult{2}, xDataRV, yDataRV);
```

Day 10 Bulk Nanoparticle Concentration Model

```
function [fitresult, gof] = createFits(D10LVM_Distance, D10LVM_Concentration,
D10RVM_Distance, D10RVM_Concentration)
%CREATEFITS(D10LVM_DISTANCE,D10LVM_CONCENTRATION,D10RVM_DISTAN
CE,D10RVM_CONCENTRATION)
%  Create fits.
%
%  Data for 'D10 LVM NP Concentration' fit:
%      X Input : D10LVM_Distance
%      Y Output: D10LVM_Concentration
%  Data for 'D10 RVM NP Concentration' fit:
%      X Input : D10RVM_Distance
%      Y Output: D10RVM_Concentration
%  Output:
%      fitresult : a cell-array of fit objects representing the fits.
%      gof : structure array with goodness-of fit info.
%% Initialization.

% Initialize arrays to store fits and goodness-of-fit.
fitresult = cell( 2, 1 );
gof = struct( 'sse', cell( 2, 1 ), ...
    'rsquare', [], 'dfe', [], 'adjrsquare', [], 'rmse', [] );
```

```
%% Fit: 'D10 LVM NP Concentration'.
[xDataLV, yDataLV] = prepareCurveData( D10LVM_Distance, D10LVM_Concentration
);

% Set up fittype and options.
ft = fittype( 'gauss1' );
opts = fitoptions( 'Method', 'NonlinearLeastSquares' );
opts.Display = 'Off';
opts.Lower = [-Inf -Inf 0];
opts.StartPoint = [39.0583199571964 0.498151 0.257444155389627];

% Fit model to data.
[fitresult{1}, gof(1)] = fit( xDataLV, yDataLV, ft, opts );

% Plot fit with data.
figure( 'Name', 'D10 LVM NP Concentration' );
hLV = plot( fitresult{1}, xDataLV, yDataLV );
legend( hLV, 'D10LVM_Concentration vs. D10LVM_Distance', 'D10 LVM NP
Concentration', 'Location', 'NorthEast' );
% Label axes
xlabel( 'D10LVM_Distance' );
ylabel( 'D10LVM_Concentration' );
```

```
grid on


%% Fit: 'D10 RVM NP Concentration'.
[xDataRV, yDataRV] = prepareCurveData( D10RVM_Distance, D10RVM_Concentration
);


% Set up fittype and options.
ft = fittype( 'gauss1' );
opts = fitoptions( 'Method', 'NonlinearLeastSquares' );
opts.Display = 'Off';
opts.Lower = [-Inf -Inf 0];
opts.StartPoint = [21.3207516578303 0.53948 0.22899154156691];


% Fit model to data.
[fitresult{2}, gof(2)] = fit( xDataRV, yDataRV, ft, opts );


% Plot fit with data.
figure( 'Name', 'D10 RVM NP Concentration' );
hRV = plot( fitresult{2}, xDataRV, yDataRV );
legend( hRV, 'D10RVM_Concentration vs. D10RVM_Distance', 'D10 RVM NP
Concentration', 'Location', 'NorthEast' );
% Label axes
xlabel( 'D10RVM_Distance' );
```

```
ylabel( 'D10RVM_Concentration' );
grid on


% Plot fits with data on same plot.
figure( 'Name', 'D10 Ventricular Myocardium NP Concentration' );
hLV = plot(fitresult{1}, xDataLV, yDataLV);
hold on
hRV = plot (fitresult{2}, xDataRV, yDataRV);
```

Day 10 Bulk Nanoparticle Transport Model

```
function [fitresult, gof] = createFits(D10LVM_Distance, D10LVM_Perfusion,
D10RVM_Distance, D10RVM_Perfusion)
%CREATEFITS(D10LVM_DISTANCE,D10LVM_PERFUSION,D10RVM_DISTANCE,D
10RVM_PERFUSION)
%  Create fits.
%
%
%  Data for 'D10 LVM Perfusion' fit:
%      X Input : D10LVM_Distance
%      Y Output: D10LVM_Perfusion
%  Data for 'D10 RVM Perfusion' fit:
%      X Input : D10RVM_Distance
%      Y Output: D10RVM_Perfusion
%  Output:
%      fitresult : a cell-array of fit objects representing the fits.
%      gof : structure array with goodness-of fit info.
%% Initialization.

% Initialize arrays to store fits and goodness-of-fit.
fitresult = cell( 2, 1 );
gof = struct( 'sse', cell( 2, 1 ), ...
```

```
    'rsquare', [], 'dfe', [], 'adjrsquare', [], 'rmse', [] );

%% Fit: 'D10 LVM Perfusion'.
[xDataLV, yDataLV] = prepareCurveData( D10LVM_Distance, D10LVM_Perfusion );

% Set up fittype and options.
ft = fittype( 'exp1' );
opts = fitoptions( 'Method', 'NonlinearLeastSquares' );
opts.Display = 'Off';
opts.StartPoint = [5.67484390317823e-05 3.1386060156809];

% Fit model to data.
[fitresult{1}, gof(1)] = fit( xDataLV, yDataLV, ft, opts );

% Plot fit with data.
figure( 'Name', 'D10 LVM Perfusion' );
hLV = plot( fitresult{1}, xDataLV, yDataLV );
legend( hLV, 'D10LVM_Perfusion vs. D10LVM_Distance', 'D10 LVM Perfusion',
'Location', 'NorthEast' );
% Label axes
xlabel( 'D10LVM_Distance' );
ylabel( 'D10LVM_Perfusion' );
grid on
```

```
%% Fit: 'D10 RVM Perfusion'.
[xDataRV, yDataRV] = prepareCurveData( D10RVM_Distance, D10RVM_Perfusion );

% Set up fittype and options.
ft = fittype( 'exp1' );
opts = fitoptions( 'Method', 'NonlinearLeastSquares' );
opts.Display = 'Off';
opts.StartPoint = [1.57764708734666e-05 5.70950742220828];

% Fit model to data.
[fitresult{2}, gof(2)] = fit( xDataRV, yDataRV, ft, opts );

% Plot fit with data.
figure( 'Name', 'D10 RVM Perfusion' );
hRV = plot( fitresult{2}, xDataRV, yDataRV );
legend( hRV, 'D10RVM_Perfusion vs. D10RVM_Distance', 'D10 RVM Perfusion',
'Location', 'NorthEast' );
% Label axes
xlabel( 'D10RVM_Distance' );
ylabel( 'D10RVM_Perfusion' );
grid on
```

```
% Plot fits with data on same plot.
figure( 'Name', 'D10 Ventricular Myocardium NP Concentration' );
hLV = plot(fitresult{1}, xDataLV, yDataLV);
hold on
hRV = plot (fitresult{2}, xDataRV, yDataRV);
```